The North Pacific biological pump: Rates, efficiency and influence on ocean carbon uptake

Hilary Ilana Palevsky

A dissertation

submitted in partial fulfillment of the

requirements for the degree of

Doctor of Philosophy

University of Washington

2016

Reading Committee:

Paul D. Quay, Chair

Steven R. Emerson

Curtis Deutsch

Program Authorized to Offer Degree:

School of Oceanography

University of Washington

Abstract

The North Pacific biological pump: Rates, efficiency and influence on ocean carbon uptake

Hilary Ilana Palevsky

Chair of the Supervisory Committee:
Professor Paul D. Quay
School of Oceanography

The North Pacific features a band of strong atmospheric CO_2 uptake at the transition between the subarctic and subtropical gyres, making it a region of particular importance to quantify the rates and mechanisms of ocean carbon cycling. We measured the surface concentration of dissolved inorganic carbon (DIC), the partial pressure of carbon dioxide to determine air-sea CO_2 flux, and triple oxygen isotopes and oxygen/argon dissolved gas ratios as non-incubation based geochemical tracers of gross oxygen production (GOP) and net community production (NCP) on sixteen container ship transects across the North Pacific between Hong Kong and Long Beach, CA from 2008-2012. This dissertation assesses the rates and efficiency of biological carbon export and evaluates the relative roles of biology, physical circulation, and temperature-driven solubility changes in driving air-sea CO_2 flux throughout the full annual

cycle across the North Pacific basin (35°N – 50°N, 142°E – 125°W) by constructing mixed layer budgets that account for physical and biological influences on the measured tracers.

The dynamic western basin influenced by the Kuroshio and Oyashio currents experiences a stronger seasonal cycle in DIC, NCP and GOP than the more quiescent eastern basin. During the productive season from spring through fall, GOP and NCP are highest in the Kuroshio region west of 170°E and decrease eastward across the basin. However deep winter mixed layers (>200 m) west of 160°W ventilate ~40-90% of this seasonally exported carbon while only ~10% of seasonally exported carbon east of 160°W is ventilated in winter where mixed layers are <120 m. As a result, despite higher annual GOP in the west than the east, the annual carbon export (sequestration) rate and efficiency decrease westward across the basin from export of 2.3 ± 0.3 mol C m^{-2} yr^{-1} east of 160°W to 0.5 ± 0.7 mol C m^{-2} yr^{-1} west of 170°E. The annual ocean carbon sink is strongest in the Kuroshio region and decreases eastward across the basin (air-sea CO_2 flux of 2.7 ± 0.9 mol C m^{-2} yr^{-1} west of 170°E, as compared to 2.1 ± 0.3 mol C m^{-2} yr^{-1} east of 160°W). This indicates that carbon export via the biological pump can fully account for annual CO_2 uptake in the eastern basin, but less than 20% of annual CO_2 uptake in the Kuroshio region, requiring a significant removal of DIC via physical processes in the west. The seasonal timing of NCP as well as its annual magnitude strongly affects the influence of the biological pump on air-sea CO_2 flux.

Estimates of primary and export production from satellite algorithms and global biogeochemical models provide promising tools to extend analysis over spatial and temporal scales where in situ measurements are unavailable. However, we find that no single satellite algorithm or model can reproduce seasonal and annual geochemically-determined primary production and NCP rates throughout the North Pacific basin, based on comparisons throughout

the full annual cycle at time series stations in the subarctic and subtropical gyres and in the basin-wide region sampled by container ship transects. The high latitude regions show large primary production discrepancies in winter and spring and strong effects of deep winter mixed layers on annual NCP that cannot be accounted for in current satellite-based approaches. These results underscore the need to evaluate satellite- and model-based estimates using multiple productivity parameters measured over broad ocean regions and throughout the full annual cycle, including during winter ventilation, in order to accurately estimate the rate and efficiency of carbon sequestration via the ocean's biological pump.

TABLE OF CONTENTS

LIST OF FIGURES

LIST OF TABLES

ACKNOWLEDGEMENTS

Scientific scholarship is a collaborative pursuit, and this work would not be possible without the support of the superlative scientific community I have been a part of these past six years.

Thanks go first and foremost to my adviser, Paul Quay. Paul has provided me with fantastic research opportunities and incredible freedom throughout my graduate education. His trademark insightful questions and eager intellectual engagement have shaped my scientific thinking, teaching me that the best way to challenge a new idea is to consider, "What would Paul ask?" I am grateful for Paul's patience and perspective, his ready laughter, and his encouragement and support of all my endeavors.

I am also grateful for the ideas and support of each of my other committee members. Steve Emerson has always been willing to help me get to the bottom of any scientific puzzle, large or small, and deserves special recognition as the only member of my committee to have gone to sea with me and personally collected samples included in this dissertation. Ginger Armbrust has been a source of guidance throughout my graduate career, and I appreciate her knack for always finding the big picture. Curtis Deutsch and Eric Steig have provided valuable feedback and advice from the time of my general exam onwards, which has greatly improved the quality of this work.

The dataset presented in this dissertation, collected over more than five years of seagoing and analytical laboratory work, required the heroic efforts of many. Johnny Stutsman and Mark Haught, in particular, were indispensable to sample collection and measurement. It was a privilege to learn the ins and outs of our field and analytical methods from such patient and experienced scientists. Thanks go as well to Deirdre Lockwood and Eric Armstrong for years of work in the lab and at sea. I am also grateful to the Orient Overseas Container Line (OOCL) and the captains and crews of the M/V OOCL Tokyo, M/V OOCL Tianjin, and R/V Melville for their assistance and gracious hospitality at sea. Finally, my analysis of the data benefited tremendously from collaboration with David (Roo) Nicholson, who introduced me to the world of global biogeochemical models, and Deirdre Lockwood, whose PhD research established the

foundation for my work, as well as discussion with fellow UW graduate students Dave Munro, Andrea Fassbender, Seth Bushinsky and Noel Pelland, who shared insights from tackling related problems in their own research.

My success as a graduate student and my development as a scientist have benefitted immensely from the community of faculty, staff, graduate students and undergraduates in the School of Oceanography and in the interdisciplinary community created through the Program on Climate Change. Special thanks go to LuAnne Thompson and Miriam Bertram, who have been incredible mentors and advocates, and to the many fellow graduate students who have shared their energy, advice, encouragement, and ideas with me throughout these past six years. I am grateful as well for the opportunities I have had to teach undergraduate students – in particular, the UW Oceanography senior class of 2013, the Evergreen State College General Chemistry II students of summer 2014, and former undergraduate research students Mariela R. T. White and Greg Ikeda – whose enthusiasm and joy inspire my continued drive to study and teach science.

Finally, scientific study is not possible without financial support. I am grateful to the US taxpayers, private citizens, and federal funding agencies that have enabled this research. My time as a graduate student has been funded by a National Defense Science and Engineering Graduate Fellowship from the Office of Naval Research, a National Science Foundation Graduate Research Fellowship, and an ARCS Foundation Fellowship. Field work and sample analyses were funded by NSF Ocean Sciences (grant numbers 0628663 and 1259055) and the NOAA OAR Climate Program Office (grant A10OAR4310088).

DEDICATION

For my family: my parents and grandparents, who have given me a lifetime of unwavering support; my brother, who is a friend I can always count on; and my partner, who has been there for me through every step of this journey.

Chapter 1.

Introduction

Anthropogenic emissions of CO_2 from fossil fuels, industry, and land use changes are driving major perturbations to the underlying carbon cycle exchanges between the atmosphere, ocean, and terrestrial biosphere [*Ciais et al.*, 2013]. Atmospheric CO_2 concentrations have increased from approximately 277 ppm in 1750 to 397 ppm in 2014, driving changes in the earth's radiation balance and global climate [*Le Quéré et al.*, 2015]. The ocean is a major carbon sink, having absorbed 29% of all anthropogenic CO_2 emissions (42% of all fossil fuel and industrial emissions) between 1970 and 2014 [*Le Quéré et al.*, 2015]. Absorption of anthropogenic CO_2 by the ocean has slowed the rate of carbon accumulation in the atmosphere, moderating the rate of global climate change, while also causing ocean acidification due to modifications to marine carbonate chemistry as the ocean reservoir of inorganic carbon increases [*Doney et al.*, 2009a]. It is thus a matter of significant importance to quantify the current rates and spatial patterns as well as potential future changes to the ocean carbon sink.

Predicting the future trajectory of the ocean carbon sink requires a mechanistic understanding of the influences on marine carbon cycling and exchange of CO_2 between the ocean and atmosphere. The strength of the ocean carbon sink is controlled by chemical solubility, physical circulation, and biological processes. The solubility of CO_2 in seawater is strongly dependent on temperature, such that cooling waters absorb additional CO_2 from the atmosphere [*Weiss*, 1974; *Volk and Hoffert*, 1985]. Physical circulation and mixing can sequester carbon from the atmosphere by transporting CO_2 absorbed at the surface into the deep ocean. On

the biological side, photosynthesis by marine phytoplankton fixes carbon dioxide into organic carbon, at a global rate of ~50 Pg yr^{-1} [*Field et al.*, 1998]. A fraction of this fixed organic carbon escapes remineralization in the surface ocean and is transferred to the ocean interior via sinking particles, mixing, or vertical animal migration, where it is sequestered from the atmosphere on time scales of months to centuries [*Volk and Hoffert*, 1985; *DeVries et al.*, 2012]. This process of biological carbon export is commonly known as the biological pump, because it transfers carbon against a concentration gradient from the surface to the deep ocean, enabling the ocean interior to maintain an inorganic carbon reservoir ~45× that of the atmosphere [*Volk and Hoffert*, 1985; *Sarmiento and Gruber*, 2006; *Ciais et al.*, 2013].

Current understanding suggests that anthropogenic carbon uptake to date has been predominantly driven by chemical solubility and physical circulation effects as the surface ocean equilibrates with rising atmospheric CO_2 concentrations, rather than changes in biological carbon cycling [*Sabine and Tanhua*, 2010; *Bates et al.*, 2014]. However, estimates of the current global rate of carbon transfer from the surface ocean to the interior via the biological pump (~6-13 Pg C yr^{-1}; [*Laws et al.*, 2011; *Siegel et al.*, 2014]) significantly exceed the current rate at which the ocean absorbs atmospheric CO_2 (2.6 ± 0.5 Pg C yr^{-1}; [*Le Quéré et al.*, 2015]), indicating that even a small perturbation to the biological pump could have a large influence on the global carbon cycle. Changes to the strength of the biological pump would also influence the distribution of nutrients and oxygen in the ocean, which has broad implications for ocean ecosystems. Global biogeochemical models project a decrease in the strength of the biological pump over the 21st century (-1% to -18%; [*Bopp et al.*, 2013; *Laufkötter et al.*, 2015]), though there is significant spread in model projections and additional uncertainty due to the many ecosystem processes not explicitly represented in the current generation of models.

In order to effectively monitor and predict future changes to the ocean's biological pump, we need to characterize its current rates, spatial patterns, and driving mechanisms. Our current understanding is limited, however, by the difficulty of measuring the rates of biological carbon export and the processes that drive it. The rate of biological carbon export is commonly determined as net community production (NCP), defined as gross photosynthetic production (GPP) minus respiration by both autotrophs and heterotrophs. NCP can be determined based on surface ocean mass balance of carbon, nutrients, and dissolved gases (oxygen, argon, and nitrogen) [e.g. *Emerson*, 2014] or from ^{15}N incubation-based estimates of the rate of new production from nitrate [*Dugdale and Goering*, 1967]. Rates of biological carbon export from sinking particulate organic carbon (POC) can also be determined from ^{234}Th-^{238}U disequilibrium and from sediment traps, though these methods do not include contributions from dissolved organic carbon (DOC) or vertical animal migration [*Emerson and Hedges*, 2008; *Emerson*, 2014].

The efficiency of the biological pump can be determined by simultaneously measuring the rate of primary production, either as GPP or as net primary production (NPP, GPP minus autotrophic respiration). Primary production rates have most commonly been determined from ^{14}C bottle incubations to determine NPP [*Steeman Nielsen*, 1952; *Marra*, 2002]. GPP rates have also been determined from ^{18}O bottle incubations [*Bender et al.*, 1987, 1999] and, more recently, through non-incubation-based approaches using the ^{16}O, ^{17}O and ^{18}O composition of dissolved oxygen [*Luz and Barkan*, 2000; *Juranek and Quay*, 2013] and diel cycles in dissolved oxygen concentration [*Nicholson et al.*, 2015].

Our most detailed understanding of the biological pump and its role in the ocean carbon sink comes from time-series sites with robust sampling programs for carbonate chemistry and

geochemical tracers of both primary and export production, often with additional observations of ecosystem composition and structure relevant to determining mechanistic controls on export [e.g. *Church et al.*, 2013; *Bates et al.*, 2014; *Stukel et al.*, 2015]. However, existing time-series sites represent only a small fraction of the global ocean (9-15% of the total ocean area, [*Henson et al.*, 2016]) and year-round study sites are largely limited to the subtropical and tropical ocean, while high latitude sites are sampled predominantly during the spring and summer productive season. In order to address questions about the role of the biological pump in the global carbon cycle, we need global-scale data coverage spanning seasonal variations throughout the full annual cycle. Data on this scale are currently only available from satellite-based algorithms for primary and export production and global biogeochemical models [*Behrenfeld and Falkowski*, 1997; *Behrenfeld*, 2005; *Dunne et al.*, 2007; *Westberry et al.*, 2008; *Henson et al.*, 2011; *Laws et al.*, 2011; *Siegel et al.*, 2014; *Laufkötter et al.*, 2015]. These approaches are vital tools in monitoring and predicting the role of the biological pump in the global carbon cycle, but remain limited by the scarce observational data available for validation.

This dissertation quantifies the rates and efficiency of the biological pump and its role in the overall ocean carbon sink across the North Pacific over the full annual cycle based on geochemical tracer measurements, and evaluates how these new estimates advance our understanding of the region's biological pump. The North Pacific plays a significant role in the global ocean carbon sink, making it a region of particular interest for assessing the role of the biological pump in ocean carbon uptake. It features a band of strong ocean carbon uptake at the transition between the subtropics to the south and the subarctic to the north, between 30°N and 45°N (Figure 1.1). A similar band of strong carbon uptake occurs in both the Atlantic and

Southern Oceans at similar north and south latitudes, suggesting that lessons from the North Pacific may be applicable in other carbon sink regions.

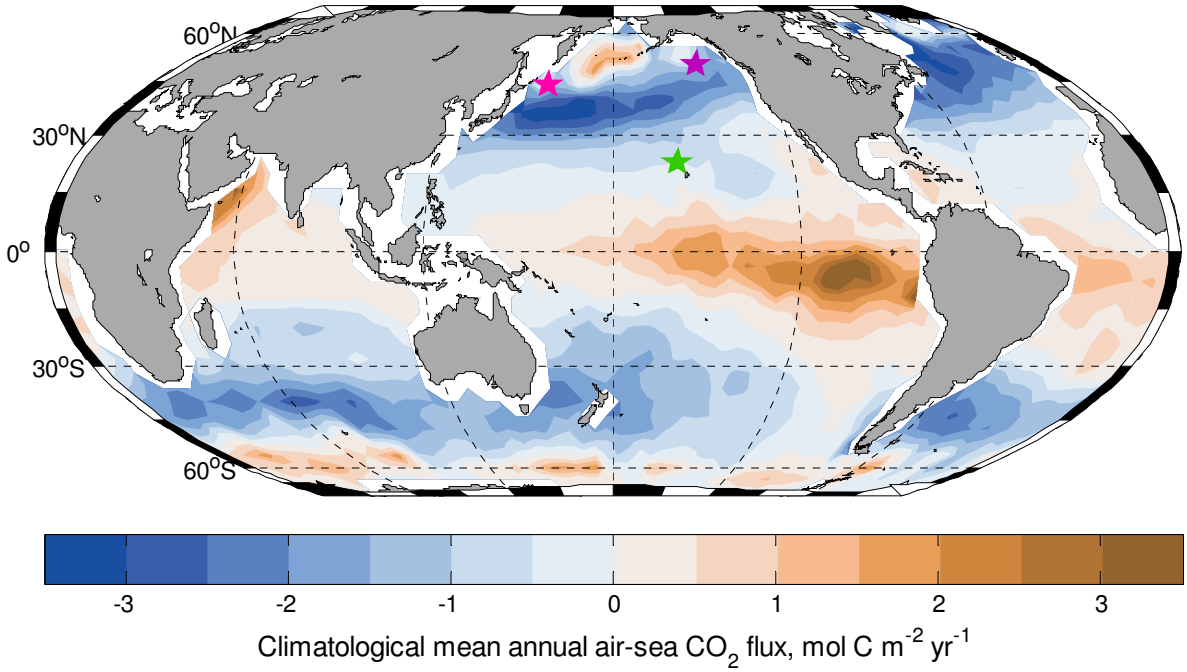

Figure 1.1 Climatological mean annual air-sea CO_2 flux, normalized to the year 2000 (data from *Takahashi et al.*, [2009]). Negative (positive) values are regions where the ocean is a net sink (source) for atmospheric CO_2. Colored stars indicate the locations of North Pacific time-series station sites (KNOT, 44°N, 155°E, in pink; Ocean Station Papa, 50°N, 150°W, in purple, Station ALOHA, 23.75°N, 158°W, in green).

Previous estimates of the rate and efficiency of the biological pump in the North Pacific have largely been limited to a few time-series stations (ALOHA in the subtropical gyre and Ocean Station Papa and Station KNOT in the eastern and western subarctic, respectively; shown in Figure 1.1), though basin-wide estimates of export have been determined from seasonal nitrate drawdown [*Wong et al.*, 2002a; *Chierici et al.*, 2006] and recent work has added primary and export production estimates at new time-series stations and mooring locations in the western subarctic and subtropical gyres [*Fassbender*, 2014; *Honda et al.*, 2015; *Matsumoto et al.*, 2016]. In order to extend our sampling range to basin-wide scales, this dissertation uses chemical

measurements of the surface ocean sampled from sixteen container transects across the North Pacific from 2008-2012 to estimate rates of GPP based on triple oxygen isotopes (TOI), NCP based on dissolved O_2/Ar gas ratios, and air-sea CO_2 flux based on measurements of surface ocean pCO_2, dissolved inorganic carbon and total alkalinity. This is the first time simultaneous geochemical-based estimates of primary and export production, as well as air-sea CO_2 flux have been made on a basin-wide scale throughout the full annual cycle.

Chapter 2 presents seasonal and annual rates of GPP and NCP in three broad regions across the North Pacific based on TOI and O_2/Ar measurements (n = 581) from the sixteen container ship transects. Tracer measurements are interpreted using mixed layer budgets to account for physical as well as biological influences, including new approaches to enable annual estimates of GPP through the full euphotic zone and NCP to the winter ventilation depth (the maximum depth ventilated to the atmosphere during the annual cycle). Results are compared with previous productivity estimates from these regions, demonstrating that existing time-series stations represent regional productivity rates in the eastern but not the western North Pacific. We find a basin-wide gradient in the contributions of the biological pump to annual carbon sequestration, with greater annual NCP in the eastern than the western basin, despite higher annual GPP and seasonal export of organic carbon from the mixed layer in the west. These results highlight the role of deep winter mixing in reducing the biological pump's efficiency at sequestering atmospheric carbon over annual to multi-annual time scales, and the importance of evaluating annual NCP to the winter ventilation depth.

The basin-wide estimates of GPP and NCP presented in Chapter 2 provide a unique opportunity to compare geochemically-determined estimates of the rate and efficiency of the biological pump with estimates from satellite-based algorithms and global biogeochemical

models commonly used in the absence of geochemical measurements. Chapter 3 compares estimates of primary production (PP, converted from GPP to NPP-equivalent), export production (EP, equivalent to NCP) and export efficiency (e-ratio = EP/PP) based on two satellite PP algorithms, three e-ratio algorithms, and a global biogeochemical model with in situ geochemical-based PP and EP estimates from the three basin-wide regions presented in Chapter 2 as well previous geochemical measurements at two time-series stations in the subarctic and subtropical gyres (Ocean Station Papa and ALOHA, respectively, shown in Figure 1.1). We find that no single satellite- or model-based approach matches geochemically-determined seasonal and annual PP and EP rates throughout the North Pacific. We discuss potential reasons for the observed discrepancies and identify a need for additional data from the high latitude ocean during undersampled seasons to facilitate the development and calibration of new models and algorithms.

Chapter 4 broadens in scope to consider all chemical, physical and biological processes influencing the marine carbon cycle in the North Pacific and evaluate the role of the biological pump in driving the strong regional ocean carbon sink. This chapter presents measurements of total dissolved inorganic carbon (DIC) collected on the same set of container ship transects as the dissolved gas samples discussed in Chapter 2, and an additional carbonate chemistry parameter (either total alkalinity or the partial pressure of CO_2) determined for all locations with measured DIC (n = 347), fully constraining the carbonate chemistry system. Separate influences of temperature-dependent changes in the solubility of CO_2 in seawater, air-sea CO_2 flux, NCP, $CaCO_3$ production, physical advection and mixing on surface ocean DIC and pCO_2 are evaluated both seasonally and annually in the same three sampling regions defined in Chapter 2. We find that DIC removal via organic carbon export (NCP) fully offsets DIC increase due to absorption

of atmospheric CO_2 in the East, whereas it can only account for 20% of atmospheric CO_2 uptake in the Kuroshio, requiring significant DIC removal via geostrophic advection. We discuss the role of the seasonal timing of export and ventilation in addition to the overall magnitude of annual NCP in determining the influence of the biological pump in driving air-sea CO_2 flux.

Finally, Chapter 5 concludes with a summary of the main findings from the previous chapters. We consider key lessons from this dissertation's work in the North Pacific and their implications for future study of the role of the biological pump in the global carbon cycle.

Chapter 2.

The annual cycle of gross primary production, net community production and export efficiency across the North Pacific Ocean[1]

2.1 INTRODUCTION

Export of biologically-produced organic material in the ocean, known as the biological pump, plays an important role in regulating the global carbon cycle [*Volk and Hoffert*, 1985]. Photosynthesis by marine phytoplankton fixes CO_2 into organic carbon, some fraction of which is exported from the surface to the deep ocean and sequestered from the atmosphere on multiannual time scales. Global climate models project that anthropogenic climate change will decrease the strength of the biological pump over the 21st century [*Bopp et al.*, 2013], with potential feedback effects on climate and ocean biogeochemistry. Evaluating and predicting the role of the biological pump requires a mechanistic understanding of the processes controlling the rate and spatial patterns of photosynthetic primary production, as well as the mechanisms determining what fraction of fixed organic carbon is exported to the deep ocean rather than recycled at the surface. Accurate baseline measurements of current rates of primary production and biological carbon export are necessary to validate rates predicted by remote sensing algorithms and global climate models, as well as refine our understanding of the dominant processes controlling rates and efficiency of export.

The North Pacific is a region of particular interest for quantifying the rate and efficiency of the biological pump, as it is a major sink for atmospheric CO_2, absorbing 0.5 Pg C yr^{-1}, ~25%

[1] An edited version of this chapter was published by AGU. Copyright (2016) American Geophysical Union: Palevsky, H. I., P. D. Quay, D. E. Lockwood, and D. P. Nicholson (2016), The annual cycle of gross primary production, net community production, and export efficiency across the North Pacific Ocean, *Glob. Biogeochem. Cycles*, *30*, doi:10.1002/2015GB005318.

of the total ocean CO_2 uptake [*Takahashi et al.*, 2009]. This regional carbon sink is driven largely by a band of strong CO_2 uptake between 30°N and 45°N [*Takahashi et al.*, 2002, 2009]. This band occurs at the transition between the subtropical and subarctic gyres, and is defined both physically by multiple salinity fronts [*Roden*, 1991] and biologically by the transition zone chlorophyll front (TZCF) between lower-chlorophyll subtropical waters to the south and higher-chlorophyll subarctic waters to the north [*Polovina et al.*, 2001; *Bograd et al.*, 2004]. A number of studies have attempted to quantify the contributions of biological carbon export to the North Pacific carbon sink, with recent work concluding that biological carbon export plays a role comparable to the combined effects of physical transport and solubility [*Chierici et al.*, 2006; *Ayers and Lozier*, 2012; *Lockwood*, 2013].

Productivity across the northern North Pacific has been described in most detail at two time-series locations: the Kyodo North Pacific Time Series (KNOT; 44°N, 155°E) in the western subarctic gyre and Ocean Station Papa (OSP; 50°N, 145°W) in the Alaskan gyre representing the nitrate-rich iron-limited subarctic. The western subarctic, represented by KNOT, is strongly influenced by the Kuroshio and Oyashio currents, which flow along the western boundary of the subtropical and western subarctic gyres respectively and join to form the Kuroshio Extension, while the eastern subarctic, represented by OSP, experiences weaker geostrophic transport. The deepest winter mixed layers (>200 m) are also found in the western basin, in bands directly to the north and south of the Kuroshio Extension [*Ohno et al.*, 2009]. Prior basin-wide comparisons of KNOT and OSP have observed a more pronounced seasonal cycle at KNOT featuring a spring diatom bloom, while OSP experiences a smaller-amplitude seasonal cycle with production dominated by small (<5 μm) cells year-round [*Harrison et al.*, 2004b]. Measurements beyond these time-series sites show, however, that the high carbon uptake region of the North Pacific is

not fully represented by these locations. Meridional transects spanning spring through fall have found elevated primary production and carbon export at the TZCF [*Howard et al.*, 2010; *Juranek et al.*, 2012; *Lockwood et al.*, 2012], indicating the importance of including the full spatial variability across the North Pacific in basin-scale estimates.

Non-incubation based dissolved gas tracers provide the means to estimate primary production and organic carbon export across broad spatial and temporal scales. The triple oxygen isotopic (TOI) composition of dissolved oxygen traces photosynthetic gross oxygen production (GOP) [*Luz and Barkan*, 2000; *Juranek and Quay*, 2013], and O_2/Ar dissolved gas ratios trace net community production (NCP) [*Emerson et al.*, 1991]. NCP represents the strength of the biological pump, while the fraction of GOP that contributes to NCP (NCP/GOP ratio) represents its efficiency. Dissolved gas productivity tracers integrate over the ~1-2 week residence time of gases in the surface mixed layer, facilitating capture of episodic production events, and can be applied using only surface samples, enabling underway sampling on vessels of opportunity. Repeated sampling of these and other tracers using container ship platforms have provided basin-wide estimates over the full annual cycle of both GOP and NCP in the North Atlantic [*Quay et al.*, 2012; *Ostle et al.*, 2014], GOP across the tropical and subtropical Pacific [*Juranek and Quay*, 2010], and NCP across the North Pacific [*Wong et al.*, 2002a; *Chierici et al.*, 2006; *Lockwood*, 2013].

In this study, we estimate GOP and NCP from TOI and O_2/Ar samples collected on sixteen basin-wide crossings of the North Pacific on commercial container ships. Our approach allows us to estimate rates and efficiency of biological carbon export throughout the full annual cycle across the entire North Pacific basin from 142°E – 125°W and 35°N – 50°N. These are the first basin-wide observational estimates of primary production throughout the annual cycle in the

North Pacific, and the first simultaneous application of TOI and O_2/Ar on a vessel of opportunity to estimate annual GOP, NCP and export efficiency on a basin-wide scale. We find that despite higher seasonal GOP and NCP in the western regions of the North Pacific in the spring through fall, annual carbon export rates and efficiency are greater in the east than the west due to deeper winter ventilation in the west.

2.2 METHODS

2.2.1 *Sample Collection and Measurement*

Samples for TOI and O_2/Ar analysis were collected from shipboard seawater intake (10 m depth) on sixteen basin-wide transects of the North Pacific between Hong Kong and Long Beach, California onboard the M/V OOCL Tianjin and the M/V OOCL Tokyo between October 2008 and December 2012 (Figure 2.1). Samples were collected into pre-evacuated 500-ml flasks every ~2.5° longitude across the basin following the procedures of *Emerson et al.* [1999]. Sea surface temperature (SST) and salinity at the time of sample collection were determined using a Sea-Bird Electronics SBE45 thermosalinograph installed in the ship's seawater intake. To prevent biofouling that could cause respiration in the ship's seawater lines and contaminate O_2/Ar measurements [*Juranek et al.*, 2010], intake lines between the anticorrosive sea chest and the sampling port were purged with bleach and freshwater between every cruise. Additional depth profile samples for TOI and O_2/Ar analysis were collected from a late winter cruise in February-March 2013 onboard the R/V Melville in the western North Pacific from Niskin bottles tripped at depths ranging from the surface to 300 m, chosen to capture both mixed layer and thermocline properties (Figure 2.1).

In the laboratory, dissolved gas samples were equilibrated at room temperature for 24 hours and then drained under vacuum to remove seawater. Oxygen and argon were cryogenically extracted and separated from the remainder of the dissolved gas mixture following the procedures of *Juranek and Quay* [2005]. Samples were subsequently analyzed on a Finnegan MAT 253 isotope ratio mass spectrometer using 75 paired measurements of masses 32, 33, and 34 alternating with measurements of an internal standard to determine $\delta^{17}O$ and $\delta^{18}O$, followed by measurements of masses 32 and 40 on a single collector to determine O_2/Ar. Reported values for $\delta^{17}O$ and $\delta^{18}O$ are corrected for the experimentally-determined dependence on both the sample size, as described by *Stanley et al.* [2010], and the sample O_2/Ar ratio. Measurement uncertainty for each sample batch was determined based on daily air standards, yielding a mean uncertainty (1σ) of 6.9 per meg for $^{17}\Delta$ (defined in section 2.3, equation 1), 0.020‰ for $\delta^{17}O$, 0.036‰ for $\delta^{18}O$, and 0.036 for O_2/Ar. Air-equilibrated water standards collected at both 4°C and room temperature (20-22°C) measured in a series of experiments (n=149) throughout the course of this study yield $^{17}\Delta_{eq}$ of 8 ± 1 $\left(\frac{2\sigma}{\sqrt{n}}\right)$ per meg, with no temperature dependence, consistent with the value of 8 per meg reported by *Reuer et al.* [2007] and *Stanley et al.* [2010].

2.2.2 ***Regional divisions***

We divide the North Pacific basin into three regions for analysis: the Kuroshio, west of 170°E, influenced by the Kuroshio, Oyashio, and Kuroshio Extension currents; the Western region, between 170°E and 160°W; and the Eastern region, east of 160°W (Figure 2.1). This regional division scheme enables analysis of the east-west basin-wide trends previously identified in comparisons of the western subarctic and Alaskan gyres [*Harrison et al.*, 2004b], and the influence of deeper winter mixed layers in the western basin (Figure 2.1, *Ohno et al.* [2009]). While these large regions encompass multiple physical and biological fronts across the

transition between the subarctic and subtropics which have led previous studies to create finer regional sub-divisions [e.g. *Wong et al.*, 2002; *Chierici et al.*, 2006], our coarser regional division scheme increases sampling density within each region, which yields more accurately described annual cycles**.**

All terms in the GOP and NCP budgets (section 2.3) are calculated for each discrete sample, and then compiled to calculate mean values for each budget term for each region and season. To evaluate potential for sampling bias in the three defined regions, we apply satellite observations of SST and chlorophyll as proxies for spatial and temporal variability in GOP and NCP, supported by the use of SST and chlorophyll in satellite-based algorithms for productivity and export efficiency [e.g. *Behrenfeld and Falkowski*, 1997; *Laws et al.*, 2000; *Dunne et al.*, 2005]. MODIS SST and chlorophyll (1/6° × 1/6° monthly data provided by the Oregon State Ocean Productivity group, http://www.science.oregonstate.edu/ocean.productivity) seasonal mean values for all grid points within each region sampled continuously from 2008-2012 were compared with seasonal mean values determined only from the times and cruise track locations where discrete samples were collected (Figure 2.2). Overall, the SST and chlorophyll comparison between the complete coverage and cruise track-sampled locations shows that the annual cycle in all three regions is generally well represented. There is some discrepancy in spring chlorophyll and summer SST in the Western region and spring SST in the Kuroshio region, as well as high spatial variability in Kuroshio region chlorophyll in spring and fall. We use this comparison as a means to quantify the degree of sampling bias in each region and season (see section 2.5).

2.2.3 *Triple oxygen isotope (TOI) and O_2/Ar budget approaches to estimate GOP and NCP*

Estimation of GOP and NCP rates based on measured TOI and O_2/Ar respectively requires construction of surface mixed layer budgets accounting for tracer sources and sinks. Both tracers are often interpreted by assuming steady-state conditions and negligible physical tracer flux due to mixing or advection. However, modeling and observational studies have demonstrated that these assumptions are not always valid and can introduce large errors [*Hamme et al.*, 2012; *Nicholson et al.*, 2012, 2014; *Jonsson et al.*, 2013]. In this study, we construct budgets for both TOI and O_2/Ar that account for physical supply and non-steady-state conditions to more accurately estimate GOP and NCP throughout the full annual cycle.

The TOI approach, described in detail elsewhere [*Luz and Barkan*, 2000; *Juranek and Quay*, 2013], enables estimates of GOP based on isotopic differentiation between dissolved oxygen in seawater produced during photosynthesis and dissolved oxygen contributed by atmospheric equilibration. The TOI approach requires measurements of both $\delta^{17}O$ and $\delta^{18}O$, which are commonly combined to define a single term, $^{17}\Delta$ [*Luz and Barkan*, 2005]:

$$^{17}\Delta \equiv 10^6 \left[\log\left(1+\frac{\delta^{17}O}{10^3}\right) - \lambda \log\left(1+\frac{\delta^{18}O}{10^3}\right)\right] \quad (1)$$

Oxygen in the atmosphere is depleted in ^{17}O due to mass-independent photochemical reactions in the stratosphere, and is defined as a standard such that $^{17}\Delta_{atmos} = 0$ per meg, whereas oxygen produced photosynthetically from seawater yields $^{17}\Delta_p = 250$ per meg [*Luz and Barkan*, 2000; *Lämmerzahl*, 2002]. $^{17}\Delta$ is defined to be insensitive to removal of oxygen through respiration through the empirically-determined choice of $\lambda = 0.518$, which maintains a constant $^{17}\Delta$ even while respiration consumes O_2 and enriches both $\delta^{17}O$ and $\delta^{18}O$ [*Luz and Barkan*, 2005]. The mixed layer budget for TOI, accounting for the influences of air-sea gas exchange, non-steady state TOI concentrations, and physical supply of TOI, can be solved to determine GOP:

$$\mathrm{GOP} \approx \frac{k[O_2]_{eq}(^{17}\Delta_{ml} - ^{17}\Delta_{eq}) + z_{ml}[O_2]_{ml}\left(\frac{\partial(^{17}\Delta_{ml})}{\partial t} - \left[\frac{\partial(^{17}\Delta_{ml})}{\partial t}\right]_{phys}\right)}{(^{17}\Delta_P - ^{17}\Delta_{ml})} \quad (2)$$

where k is the air-sea gas transfer velocity (m d^{-1}), z_{ml} is the mixed layer depth (m), and the subscripts P, eq, and ml represent photosynthetic end member [*Luz and Barkan*, 2009], air-equilibrated end member ($^{17}\Delta_{eq}$ = 8 per meg, section 2.1; $[O_2]_{eq}$ from *Garcia and Gordon* [1992]), and measured values respectively for mixed layer dissolved oxygen. Recent work has demonstrated the importance of calculating GOP directly from $\delta^{17}O$ and $\delta^{18}O$ rather than from $^{17}\Delta$ [*Kaiser*, 2011; *Prokopenko et al.*, 2011]. We use this more rigorous approach to the GOP budget in equation (2) but present measured TOI using the more intuitive $^{17}\Delta$.

The O_2/Ar approach enables estimates of NCP by isolating biological effects on oxygen supersaturation from effects of bubble injection and temperature-driven solubility changes, which affect argon similarly to oxygen [*Craig and Hayward*, 1987; *Emerson et al.*, 1991]. Biological oxygen supersaturation from O_2/Ar is defined as:

$$\Delta O_2/Ar = \frac{(O_2/Ar)_{ml}}{(O_2/Ar)_{eq}} - 1 \quad (3)$$

where $(O_2/Ar)_{ml}$ is the measured ratio of dissolved oxygen to argon in the mixed layer and $(O_2/Ar)_{eq}$ is the equilibrium ratio determined by the temperature- and salinity- dependent solubility of both gases [*Garcia and Gordon*, 1992; *Hamme and Emerson*, 2004]. In a system at steady state with negligible physical supply, $\Delta O_2/Ar > 0$ indicates that oxygen is supersaturated due to net autotrophic conditions, whereas $\Delta O_2/Ar < 0$ indicates net heterotrophic conditions. A surface mixed layer budget of O_2/Ar accounting for non-steady state conditions, air-sea biological oxygen flux, and physical supply of oxygen and argon can be used to estimate NCP:

$$\mathrm{NCP} = k[O_2]_{eq}\Delta O_2/Ar + \frac{\partial(\Delta O_2/Ar)}{\partial t} z_{ml}[O_2]_{eq} - z_{ml}\left(\frac{\partial O_2}{\partial t}_{phys} - (O_2/Ar)_{eq}\frac{\partial Ar}{\partial t}_{phys}\right) \quad (4)$$

The derivation of equation (4) from separate oxygen and argon budgets, following the approach of *Howard et al.* [2010], is given in Section 2.6.1.

Note that the GOP and NCP budgets (equations 2 and 4) can both be expressed in simplified form as:

$$\text{NCP or GOP} = \text{Air-sea flux} + \text{Non-steady state} - \text{Physical supply} \quad (5)$$

In conditions where the non-steady state and physical supply terms are negligible, as has often been assumed in previous applications of the TOI and $\Delta O_2/Ar$ methods, GOP and NCP are equal to their respective air-sea flux terms. Calculation details for both tracer budgets, broken down based on the three right hand side (RHS) components of equation (5), are provided below. All RHS terms in both budgets are calculated for each discrete sample, and then compiled to calculate mean values for each term for each region and season.

2.2.3.1 Air-sea flux

Air-sea tracer flux for both GOP (equation 2) and NCP (equation 4) depends on the air-sea gas transfer velocity (k) over the residence time of dissolved oxygen in the surface mixed layer in addition to tracer measurements. Daily wind speed data from the NOAA National Climactic Data Center's multiple-satellite Blended Sea Winds product (https://www.ncdc.noaa.gov/oa/rsad/air-sea/seawinds.html) were used to calculate k for the time and location of each discrete sample following the *Nightingale et al.* [2000] relationship between k and wind speed and the *Reuer et al.* [2007] weighting scheme.

Uncertainty in the air-sea gas exchange rate is estimated by assuming that the majority of uncertainty results from the parameterized relationship between gas exchange rate (k) and wind speed, and that the spread between the air-sea gas exchange rates calculated from the *Liss and Merlivat* [1986] and *Wanninkhof* [1992] equations represents 95% of the variability ($\pm 2\sigma$) in k

[*Palevsky et al.*, 2013], yielding a mean uncertainty in k of ±14% over all discrete sample locations in the data set.

2.2.3.2 Non-steady state terms

Seasonal GOP and NCP budget non-steady state terms in equations (2) and (4) are determined from discrete sample-specific tracer time rate of change tendencies and estimates of the mixed layer depth (z_{ml}, Table 2.1), and $[O_2]_{eq,}$ compiled to compute the mean non-steady state term for each region and season. To determine the tracer time rate of change tendencies, all surface mixed layer TOI and O_2/Ar data for each region are compiled into a single composite year, with the seasonal cycle of TOI and O_2/Ar determined by fitting simple harmonic functions using a least-squares approach. The derivatives of these harmonic fits for the day of the year corresponding to collection of each discrete sample are used to calculate the time rate of change tendency of mixed layer TOI and O_2/Ar, $\frac{\partial(^{17}\Delta_{ml})}{\partial t}$ and $\frac{\partial(\Delta O_2/Ar)}{\partial t}$.

2.2.3.3 Physical supply terms

Physical supply terms in the GOP and NCP budgets account for the influence on mixed layer TOI and O_2/Ar from horizontal advection due to geostrophic and Ekman transport, vertical advection from Ekman-driven upwelling, and vertical supply from entrainment and diffusive mixing. Estimating these terms requires knowledge of both the physical transport fields and the tracer spatial gradients in the ocean. For TOI, insufficient observational data exist to constrain tracer gradients, so the physical supply terms were estimated from the output of a global ocean model that included TOI (see section 2.3.3.1). For O_2/Ar, climatological O_2 gradients were used to estimate physical supply of O_2/Ar in the NCP budget (see section 2.3.3.2).

2.2.3.3.1 Physical supply term in the GOP budget

The physical supply contribution to the GOP budget was estimated using output from a global ocean model (Parallel Ocean Program of the Community Earth System Model version 1.1.1, CESM) run at a nominal 1 degree resolution and modified to explicitly include oxygen isotopogues to simulate the TOI system. The TOI simulations used here have been previously described in detail by *Nicholson et al.* [2014]. Model diagnostic tracers for lateral and vertical advective and mixing fluxes were extracted at the location and sampling month of each discrete sample and used to determine the individual contributions to the GOP budget from upwelling, horizontal advection and vertical supply (which encompasses both entrainment and diffusive vertical mixing).

To normalize for discrepancies in the spatial and temporal patterns of surface mixed layer TOI between the model and observations, the physical supply term calculated from model output was applied as a fractional physical supply bias normalized by the air-sea flux term in the GOP budget, where:

$$\text{Physical supply}_{fractional} = \frac{\text{Physical supply}_{model}}{\text{Air-sea flux}_{model}} \times \text{Air-sea flux}_{observations} \quad (6)$$

The sensitivity of the physical supply corrections to the magnitude of GOP in the model was tested by running a second simulation in which GOP was increased (1.7×) while net primary production and all other model biogeochemistry remained unchanged. The 1.7× GOP simulation produced nearly identical fractional physical supply terms, which indicates that modeled fractional corrections are not sensitive to the magnitude of GOP and supports the use of model-based physical supply terms in the GOP budget.

2.2.3.3.2 Physical supply term in the NCP budget

The physical supply contribution to the NCP budget was calculated using climatological data-based box models corresponding to the month and location of each discrete sample, similar

to the approach previously described by *Lockwood* [2013]. Oxygen and argon physical supply tendency terms in equation (4) are calculated following:

$$\begin{cases} z_{\mathrm{ml}} \frac{\partial \mathrm{O_2}}{\partial \mathrm{t}}_{phys} = \nabla \cdot \mathbf{u}_{\mathrm{Ek}} \mathrm{O_2} + \nabla \cdot \mathbf{u}_{\mathrm{Geo}} \mathrm{O_2} + \nabla \cdot \mathbf{w}_{\mathrm{Ek}} \left(\mathrm{O_{2,ml}} - \mathrm{O_{2,therm}} \right) \\ \qquad + \frac{\partial z_{\mathrm{ml}}}{\partial \mathrm{t}} \left(\mathrm{O_{2,ml}} - \mathrm{O_{2,therm}} \right) + K_z \left(\frac{\mathrm{O_{2,ml}} - \mathrm{O_{2,therm}}}{z_{\mathrm{ml}} - z_{\mathrm{therm}}} \right) \\ z_{\mathrm{ml}} \frac{\partial \mathrm{Ar}}{\partial \mathrm{t}}_{phys} = \nabla \cdot \mathbf{u}_{\mathrm{Ek}} \mathrm{Ar} + \nabla \cdot \mathbf{u}_{\mathrm{Geo}} \mathrm{Ar} + \nabla \cdot \mathbf{w}_{\mathrm{Ek}} (\mathrm{Ar_{ml}} - \mathrm{Ar_{therm}}) \\ \qquad + \frac{\partial z_{\mathrm{ml}}}{\partial \mathrm{t}} (\mathrm{Ar_{ml}} - \mathrm{Ar_{therm}}) + K_z \left(\frac{\mathrm{Ar_{ml}} - \mathrm{Ar_{therm}}}{z_{\mathrm{ml}} - z_{\mathrm{therm}}} \right) \end{cases} \quad (7)$$

where the RHS terms account for horizontal convergence due to Ekman transport ($\mathbf{u}_{\mathrm{Ek}}$), horizontal convergence due to geostrophic transport ($\mathbf{u}_{\mathrm{Geo}}$), upwelling due to Ekman-driven mass divergence ($\mathbf{w}_{\mathrm{Ek}}$), entrainment of thermocline water due to mixed layer deepening (dz_{ml}/dt), and diffusive vertical mixing across the base of the mixed layer (K_z), respectively.

Data sources for all terms in equation (7) are given in Table 2.1. Since World Ocean Atlas (WOA) data includes oxygen but not argon, we assume that argon is at saturation, which accounts for the temperature dependence of gas solubility but not for effects of injection or cooling/heating induced disequilibria. Previous work at OSP has found negligible changes in argon saturation across the mixed layer-thermocline boundary, suggesting that the differing effects of these processes across the thermocline boundary are minimal [*Giesbrecht et al.*, 2012]. The most poorly constrained parameter in physical supply term is diffusive vertical mixing at the base of the mixed layer (K_z), since literature values for K_z vary by orders of magnitude (10^{-6} to 10^{-2}, *Denman and Gargett*, 1983; *Brainerd and Gregg*, 1993; *Cronin et al.*, 2013, 2015). To estimate a K_z value appropriate for the regions sampled in this study, we determine winter K_z in the Kuroshio and Western regions by assuming winter NCP ≈ 0 [*Emerson and Stump*, 2010] and solving for K_z following equations (4) and (7), yielding values of 5.1×10^{-4} and 3.6×10^{-5} m^2 s^{-1} respectively. Observed winter O_2/Ar supersaturation in the Eastern region indicates net

autotrophy even if K_z is reduced to 0, so we chose a low winter K_z of 2.0×10^{-5} m^2 s^{-1}. Winter K_z values were also applied in spring and were scaled down for summer and fall for each region based on seasonal cycle of K_z observed at the Kuroshio Extension Observatory (KEO, 32.4°N, 144.6°E) and OSP [*Cronin et al.*, 2015]. Reasonable variations in the winter NCP assumption and resulting choice of K_z do not significantly change key findings of this study (Table 2.S1).

2.2.4 *Calculation of annual GOP and NCP rates*

The GOP and NCP rates determined from equations (2) and (4) respectively determine productivity within and export from the seasonally-varying mixed layer and thus are more appropriate for estimating seasonal than annual productivity rates. We present separate approaches for calculating annual rates of GOP and NCP, integrating to the base of the euphotic zone for GOP and to the deepest depth ventilated to the atmosphere during winter mixing (defined as the winter ventilation depth) for NCP.

GOP rates determined from equation (2) exclude sub-mixed layer production since it applies only within the seasonal mixed layer. Previous observational and modeling analyses at Station ALOHA in the subtropical North Pacific have shown that the annual integral of the air-sea TOI flux term closely (within 3%) approximates annual GOP (AGOP) integrated to the base of the euphotic zone [*Quay et al.*, 2010; *Nicholson et al.*, 2012]. CESM output further indicates that the annual integral of air-sea TOI flux approximates euphotic layer AGOP to within 6% across our sampling region in the North Pacific (Figure 2.S1) and accounts for the fraction of AGOP occurring below the seasonal mixed layer (about one-third). We therefore present euphotic zone AGOP as the annual integral of seasonal air-sea TOI flux.

As the mixed layer depth varies throughout the seasonal cycle, the effective depth to which NCP is integrated following the budget in equation (4) varies accordingly. Integrating

seasonal NCP with time to determine annual NCP (ANCP) would yield overestimates because some of the organic carbon exported from the shallow summertime mixed layer is subsequently respired before sinking out of the deeper mixed layer ventilated to the atmosphere during the following winter, as shown by *Körtzinger et al.* [2008]. To estimate an ANCP rate that represents carbon sequestered from the upper ocean over the annual cycle, one needs to integrate to the winter ventilation depth (which is slightly deeper than the winter mixed layer depth due to diffusive vertical mixing).

Long term ANCP estimated to the winter ventilation depth has been determined previously in the North Atlantic by integrating air-sea oxygen flux over several annual cycles [*Quay et al.*, 2012]. This approach assumed no net O_2 transport out of the region. We build on this approach by accounting for O_2 transport out of the region from horizontal advection both within and below the mixed layer and upwelling across the base of the seasonal mixed layer.

$$\mathrm{ANCP} = \mathrm{k}[\mathrm{O_2}]_{\mathrm{eq}}\Delta \mathrm{O_2/Ar} - z_{\mathrm{ml}}\left(\frac{\partial \mathrm{O_2}}{\partial \mathrm{t}}_{\mathrm{Geo+Ek}} - (\mathrm{O_2/Ar})_{\mathrm{eq}}\frac{\partial \mathrm{Ar}}{\partial \mathrm{t}}_{\mathrm{Geo+Ek}}\right) - \int_{z_{ml,max}}^{z_{ml}}\left(\frac{\partial \mathrm{O_2}}{\partial \mathrm{t}}_{\mathrm{phys,sub\text{-}ml}} - (\mathrm{O_2/Ar})_{\mathrm{eq}}\frac{\partial \mathrm{Ar}}{\partial \mathrm{t}}_{\mathrm{phys,sub\text{-}ml}}\right) dz \quad (8)$$

The RHS terms represent air-sea biological oxygen flux, physical supply due to horizontal advection of the mixed layer, and physical supply due to sub-mixed layer physical transport. Each RHS term is integrated over the full annual cycle, using seasonal mean data for each region.

Physical supply due to horizontal advection of the mixed layer (RHS term 2 in equation 8) is calculated from the geostrophic and Ekman O_2 and Ar supply terms in equation (7). Sub-mixed layer physical supply of O_2 and Ar (RHS term 3 in equation 8) are calculated from data sources in Table 2.1 following:

$$\begin{cases} \frac{\partial O_2}{\partial t}_{phys,sub\text{-}ml} = \nabla \cdot \mathbf{u}_{Ek,z} O_2 + \nabla \cdot \mathbf{u}_{Geo,z} O_2 + \nabla \cdot \mathbf{w}_{Ek}\left(O_{2,z} - O_{2,z+\Delta z}\right) \\ \frac{\partial Ar}{\partial t}_{phys,sub\text{-}ml} = \nabla \cdot \mathbf{u}_{Ek,z} Ar + \nabla \cdot \mathbf{u}_{Geo,z} Ar + \nabla \cdot \mathbf{w}_{Ek}(Ar_z - Ar_{z+\Delta z}) \end{cases} \quad (9)$$

where the RHS terms account for horizontal convergence due to Ekman transport, horizontal convergence due to geostrophic transport, and vertical convergence due to upwelling, each for a particular depth between the base of the seasonal mixed layer (z_{ml}) and the maximum annual mixed layer depth ($z_{ml,max}$). Sub-mixed layer Ekman transport velocities were assumed equal to mixed layer transport velocity above the Ekman depth and zero below the Ekman depth. Sub-mixed layer geostrophic velocities were calculated from relative geostrophic velocities at each depth interval based on geopotential anomalies calculated from WOA T and S, normalized to mixed layer geostrophic velocities. Upwelling rates driven by Ekman divergence were assumed constant throughout the sub-mixed layer region above $z_{ml,max}$.

2.2.5 *Uncertainty analysis*

We quantify uncertainty in the seasonal and annual mean GOP and NCP estimates for each region resulting from two sources: 1) error in the method used to calculate GOP and NCP, and 2) undersampling bias. Variability around the mean, reflecting spatial and temporal variability within each region, is reported as the standard deviation of the mean value. Combined uncertainty from individual sources of error was determined using a Monte Carlo approach. Uncertainty in seasonal mean $^{17}\Delta$ and $\Delta O_2/Ar$ (2σ) was determined based on 3000 simulations where individual measured values varied according to sample-specific TOI and O_2/Ar measurement error. Additional uncertainty from estimation of the air-sea gas transfer rate (described in section 2.4) and the time rate of change and physical supply correction terms was included in the Monte Carlo simulations to estimate total methodological uncertainty, with these

sources of uncertainty dominating over measurement error except where $\Delta O_2/Ar$ approaches zero. Uncertainty in estimating physical supply budget terms from modeled and climatological data products is difficult to quantify; however, as a representative estimate, we assume 50% uncertainty in all correction terms. Thus, when the magnitude of the correction terms in the GOP and NCP budgets is large, we estimate increased uncertainty in the calculated GOP and NCP rates. Vertical supply dominates the contribution of the correction terms to methodological uncertainty, with the time rate of change, horizontal supply and upwelling terms playing a minor role.

We estimate the magnitude of undersampling bias in the air-sea flux terms as the percent difference between mean satellite-based chlorophyll concentrations calculated over the entire region and season versus those calculated using only the times and locations of our discrete sample collection (section 2.2; Figure 2.2). Potential undersampling could result from insufficient sampling of spatial variability throughout each region or from temporal gaps (for instance a gap in spring sampling between early March and May in the Kuroshio and Western regions). While this is an imperfect metric because variability in chlorophyll may not match variability in productivity, it enables us to quantify the limitations of our sampling strategy. Methodological uncertainty and undersampling bias are combined to calculate total uncertainty in the air-sea flux terms for GOP and NCP. Methodological uncertainty dominates over undersampling bias in all regions and seasons except the Kuroshio in fall and the Western region in spring, where sub-sampled chlorophyll deviates most significantly from fully sampled regional mean chlorophyll (Figure 2.2). For annual rates, methodological uncertainty dominates in the Western and Eastern regions, but undersampling bias dominates (75-85% of total uncertainty) in the Kuroshio region.

2.3 RESULTS AND DISCUSSION

2.3.1 *Annual cycle of TOI and O_2/Ar observations*

In each of the three regions, both $^{17}\Delta$ and O_2/Ar describe a seasonal cycle with a winter minimum and summer maximum (Figure 2.3, Table 2.2). These tracer patterns reflect the combined influences of productivity, gas exchange and physical supply. In summer, when the influence of physical supply is low and reduced wind speeds produce low gas transfer rates, GOP and NCP exert relatively strong influence to elevate mixed layer $^{17}\Delta$ and O_2/Ar. In winter, by contrast, entrainment and vertical mixing exert a strong influence on mixed layer $^{17}\Delta$ and O_2/Ar, evident in particular in significant winter O_2/Ar undersaturation in the Kuroshio and Western regions.

The amplitude of the seasonal cycle for both $^{17}\Delta$ and O_2/Ar is largest in the Kuroshio and decreases eastward across the basin. Spatial and temporal variability, as reflected in the standard deviations of the mean tracer values, are also highest in the Kuroshio and decrease eastward (Table 2.2). This is consistent with more complex physical dynamics and stronger mesoscale eddy activity in the region influenced by the Kuroshio, Oyashio and Kuroshio Extension currents, which would be expected to increase spatial and temporal heterogeneity in biological productivity [*Sasai et al.*, 2010].

2.3.2 *Seasonal GOP and NCP budgets*

The seasonal cycle of GOP and NCP calculated from the tracer budgets in equations (2) and (4) are shown in Figure 2.4 and Table 2.2. Regional means and associated uncertainty values for each budget term in each season are in Tables 2.S2 (GOP) and 2.S3 (NCP)**.** The seasonal cycle is similar in all regions, with a pronounced spring bloom in GOP and elevated spring NCP.

GOP in all seasons and NCP in spring and summer are highest in the Kuroshio and decrease in magnitude eastward across the basin.

2.3.2.1 Influence of physical supply on seasonal budgets

The magnitude of the physical supply and non-steady state terms illustrate deviation from the assumption that air-sea tracer flux alone represents GOP and NCP. Vertical supply from diffusive mixing and entrainment dominate these terms in the seasonal GOP and NCP budgets, with upwelling, horizontal advection, and non-steady state processes playing a minor role (Figure 2.4). Variations in the influence of vertical supply over the year reflect the seasonal cycle in both the strength of entrainment and vertical diffusion and the gradients in TOI and O_2/Ar across the base of the mixed layer.

For GOP, the influence of vertical supply is strongest in fall when mixed layer deepening entrains the elevated $^{17}\Delta$ signature from summer photosynthesis in the sub-mixed layer portion of the euphotic zone. During summer, vertical supply is driven by strong TOI gradients despite relatively low vertical exchange across the strongly stratified summer mixed layer, while during winter, vertical supply is driven by strong vertical mixing and entrainment as the mixed layer deepens but relatively weaker TOI gradients once the entire summer euphotic zone has been ventilated. The minimum influence of vertical supply on the GOP budget is in spring, when the vertical TOI gradient is reduced following winter mixing and there is no influence of entrainment as the mixed layer shoals. The seasonal cycle in the GOP vertical supply term is fairly similar across the entire basin. (Figure 2.4, Table 2.S2).

The seasonal pattern of physical supply influence on the NCP budget differs significantly from that for the GOP budget, with the vertical supply term for NCP playing the largest role in winter and spring. The vertical gradient in O_2/Ar across the base of the mixed layer is greatest in

winter and spring when respiration produces strong oxygen undersaturations in the thermocline. For GOP, in contrast, TOI is not influenced by respiration and the vertical gradient is strongest in late summer and fall. The magnitude of the seasonal cycle in the NCP physical supply terms decreases dramatically eastward across the basin, driven by winter physical supply that offsets large negative air-sea flux in the Kuroshio region but approaches zero in the Eastern region. This effect is dominated by deeper winter mixed layers and stronger winter mixing in the western basin, yielding larger entrainment and vertical diffusion terms.

2.3.2.2 Influence of mixed layer depth on the seasonal GOP and NCP cycles

Since the GOP and NCP budgets integrate to the base of the seasonal mixed layer, they are affected by seasonal changes in mixed layer depth. During the period when the mixed layer is shallower than the euphotic zone in late spring through early fall, photosynthesis occurs below the mixed layer, contributing additional GOP and NCP not included in the mixed layer budgets. To estimate the fraction of the total GOP and NCP occurring below the mixed layer we use depth-resolved photosynthesis and respiration output from CESM in the North Pacific (Figure 2.S2). We apply a single basin-wide estimate of sub-mixed layer production rather than a spatially-varying estimate to avoid introducing spatial biases in CESM productivity in our tracer-based estimates and because the resulting seasonal cycle estimates are largely insensitive to this choice. During summer (June-August) when the mixed layers are shallowest (~20 m), 55% of the total euphotic zone GOP and 42% of the total NCP to the compensation depth occurs below the mixed layer.

We estimate seasonal GOP and NCP rates including sub-mixed layer production by scaling up the tracer-based mixed layer rates using CESM estimates of the fraction of GOP and NCP occurring below the mixed layer in each season (Figure 2.4). Across the basin, GOP shows

maximum rates in spring, which decrease during summer and then slightly increase during fall. A similar seasonal trend is seen in MODIS chlorophyll concentrations for all regions (Figure 2.2), suggesting that the observed seasonal cycle in GOP may reflect seasonal migration of the TZCF across these regions (Figure 2.S3). When the TZCF is at its northernmost location in summer (~40° N), a larger proportion of each region is within the less productive lower-chlorophyll area south of the front, which reduces GOP. Then in fall as the TZCF migrates south there is a corresponding GOP increase. During winter, when the TZCF is at its farthest south location, GOP matches or exceeds summer rates in all regions. Winter GOP is further discussed in section 2.3.2.4.

The seasonal cycle for NCP is similar to that for GOP, with spring and fall NCP rates greater than or comparable to summer rates in all regions, but with a less pronounced spring maximum in the Kuroshio and West for NCP than for GOP and the annual maximum NCP in the East occurring in fall rather than spring. This indicates seasonal changes in export efficiency, with a greater fraction of GOP contributing to export in fall than in spring, consistent with previous estimates in the eastern North Pacific [*Juranek et al.*, 2012]. Winter NCP was assumed to approach zero in all regions (see section 2.3.3.2), precluding the ability to interpret this portion of the seasonal cycle.

2.3.2.3 Comparison with previous seasonal productivity estimates

North Pacific primary and export production north of the subtropics have previously been measured in most detail at two time-series locations: OSP just north of our Eastern region and KNOT in the Kuroshio region, both representing the subarctic gyres (e.g. *Harrison et al.*, 1999, 2004) . Primary productivity has primarily been described based on ^{14}C incubation-based net primary production (NPP), with the only previous GOP estimates (based on TOI) from spring

and early fall transects across the Eastern region [*Juranek et al.*, 2012]. We convert our GOP rates to ^{14}C-NPP equivalent rates to compare to previous measurements using an empirically-determined gross O_2: net C ratio of 2.7 [*Marra*, 2002]. Export production has been previously estimated based on nutrient, oxygen and carbon mass balance, ^{234}Th-^{238}U disequilibrium, and $^{15}NO_3^-$ incubation experiments. We convert our NCP rates from oxygen to carbon units to compare to previous measurements using a O_2: C ratio of 1.4 [*Laws*, 1991].

In the Eastern region, our estimates of NPP and NCP are generally comparable to previous measurements at OSP and in the broader region over the spring through fall productive season (Tables 2.3-2.4). The greatest discrepancy is in summer, when our estimates of mean NPP and NCP are about half of previous measurements even when sub-mixed layer production is included, likely reflecting lower productivity south of the TZCF in the region covered by our cruise tracks while OSP remains north of the TZCF year-round. In the Kuroshio region, by contrast, our estimates of NPP are about double previous measurements at KNOT during spring-fall and an order of magnitude higher in winter (Table 2.3). For NCP our estimates are 1-2× higher than previous measurements in spring-fall, though generally agree within uncertainty (Table 2.4). Given the high spatial variability in the TOI, O_2/Ar, SST and chlorophyll observations in the Kuroshio region, it is not surprising that there is greater discrepancy between results and suggests that measurements primarily at a single time series station in the western subarctic gyre do not reflect productivity trends throughout the broader region. In contrast OSP appears to more fully reflect productivity throughout the less dynamic Eastern region. These observations are consistent with recent model analysis of time-series observing stations' spatial footprints showing that OSP represents more than twice the area of western subarctic gyre station K2 (near KNOT, at 47°N, 160°E) for both primary production and export [*Henson et al.,* 2016].

2.3.2.4 Winter GOP in the Kuroshio region

Because of the large (15×) discrepancy between our estimate of wintertime NPP in the Kuroshio region compared to previous results we further verify winter GOP rates by analyzing depth profiles of TOI and O_2/Ar from four locations in the Kuroshio region collected during a research cruise in February-March 2013 (Figure 2.S4). The depth profile observations more tightly constrain TOI and O_2/Ar budgets and, therefore, estimated winter GOP and NCP rates because we avoid using the CESM- and WOA-based physical supply corrections.

Given that vertical supply and air-sea flux are the major terms in the GOP and NCP budgets, we estimate GOP and NCP from these profiles assuming negligible time rate of change and horizontal supply:

$$\mathrm{GOP} \approx \frac{k[O_2]_{eq}\left({}^{17}\Delta_{ml} - {}^{17}\Delta_{eq}\right)}{\left({}^{17}\Delta_{P} - {}^{17}\Delta_{ml}\right)} - \frac{T_{vert}\left([O_2]_{therm}\,{}^{17}\Delta_{therm} - [O_2]_{ml}\,{}^{17}\Delta_{ml}\right)}{\left({}^{17}\Delta_{P} - {}^{17}\Delta_{ml}\right)} \quad (10)$$

$$\mathrm{NCP} = k[O_2]_{eq}\Delta O_2/\mathrm{Ar} - T_{vert}\left(\left(O_{2,ml} - O_{2,therm}\right) - (O_2/\mathrm{Ar})_{eq}\left(\mathrm{Ar}_{ml} - \mathrm{Ar}_{therm}\right)\right) \quad (11)$$

where the first RHS terms are air-sea tracer flux as defined in equations (2) and (4), and in the second RHS terms, T_{vert} represents the total vertical transport by entrainment, vertical diffusion, and upwelling across the base of the mixed layer (m d^{-1}). The subscripts "P", "therm" and "ml" represent the photosynthetic endmember, thermocline and mixed layer respectively. All terms in equation (10) are expressed here using ${}^{17}\Delta$ for simplicity, but are calculated directly from $\delta^{17}O$ and $\delta^{18}O$ (see *Nicholson et al.* [2014], equation S7 for the full vertical supply equation). Oxygen and argon concentrations in equation (11) are calculated from measured O_2/Ar by assuming argon is at saturation, as discussed previously.

Equations (10) and (11) provide two equations to constrain three unknown values: GOP, NCP and T_{vert}. We therefore determine possible GOP and T_{vert} rates at each depth profile location over a range of possible NCP rates (Figure 2.5). Since ΔO_2/Ar decreases (becomes more

undersaturated) and $^{17}\Delta$ increases with depth across the mixed layer-thermocline boundary (Figure 2.S4), a decrease in prescribed NCP in equation (11) reduces estimated T_{vert} and increases GOP estimated in equation (10). Uncertainty in all terms is estimated using a Monte Carlo approach accounting for uncertainty in tracer measurements and the air-sea-gas transfer velocity. We expect wintertime NCP to approach zero [*Emerson and Stump*, 2010]. Estimates of particulate organic carbon export from ^{234}Th yield slight net autotrophy at KNOT and OSP in winter (2-3 mmol C m^{-2} d^{-1}, [*Charette et al.*, 1999; *Kawakami et al.*, 2004; *Kawakami and Honda*, 2007]) while recent oxygen and carbon annual budgets accounting for dissolved as well as particulate organic carbon at OSP have found wintertime net heterotrophy [*Bushinsky and Emerson,* 2015; *Fassbender et al.,* 2016]. We determine GOP rates for a wider range of NCP than is likely plausible, spanning -25 to 25 mmol O_2 m^{-2} d^{-1} and find a mean GOP rate of 125 ± 52 mmol O_2 m^{-2} d^{-1} (Figure 2.5). These GOP rates are 38% lower than the Kuroshio region mixed layer winter GOP rate of 201 ± 45 mmol O_2 m^{-2} d^{-1}, but when converted to net carbon units (i.e., GOP/2.7) yield an NPP rate of 46 ± 19 mmol C m^{-2} d^{-1} that substantially exceeds (by ~10×) previous NPP estimates (5 ± 1 mmol C m^{-2} d^{-1}) in this region (Table 2.3). The results of this analysis support our conclusion that NPP rates during winter in the Kuroshio region are 10-15× higher than rates measured previously by ^{14}C incubation at KNOT, which suggests that a single time series station is insufficient to accurately represent the region.

2.3.3 *Annual gross oxygen production (AGOP)*

AGOP through the full euphotic zone, as determined from annually-integrated air-sea TOI flux, and in the mixed layer, as determined by integrating equation (2) over the annual cycle, is highest in the Kuroshio region and decreases eastward across the basin, with sub-mixed layer production contributing 19-25% of the total euphotic zone GOP (Figure 2.6a, Tables 2.2

and 2.S4). The observed trend is consistent with stronger nutrient supply from deeper winter mixing and greater aeolian iron supply from dust input in the western than the eastern basin [*Duce and Tindale*, 1991]. However, previous estimates of annual NPP at KNOT and OSP found the opposite trend, with ^{14}C-based annual NPP in the eastern subarctic at OSP estimated as about twice that at KNOT (Table 2.3). The difference in these results is primarily because our TOI-based annual NPP estimates are ~4× previous ^{14}C-based estimates in the Kuroshio region but comparable to results at OSP in the eastern region (Table 2.3).

Potential explanations for the discrepancy between previous Kuroshio region estimates and our results include: 1) Measurements primarily at a single time series station at KNOT in the dynamic Kuroshio region do not capture the full spatial variability in the region. 2) Incubation-based NPP measurements used in previous studies may fail to capture episodic pulses of productivity, which are more easily observed using the TOI approach since the measurements are integrated over the ~2 week residence time of dissolved oxygen in the surface mixed layer. 3) The gross O_2: net C conversion factor varies spatially from the constant 2.7 factor assumed here (as discussed in *Juranek and Quay*, [2013]). However, this can only explain a small portion of the discrepancy as the GOP/NPP ratio of 8-10 that would be required to reconcile our AGOP estimates with annual NPP previously estimated at KNOT is at the high end of the GOP/NPP range of 2-8 previously observed in the ocean [*Juranek and Quay*, 2013] and well above the ratio of 3 ± 1 found in nutrient-limited laboratory cultures [*Halsey and Jones*, 2015].

2.3.4 *Annual net community production (ANCP)*

ANCP integrated to the winter ventilation depth, calculated separately from the seasonal NCP budget following equation (8), decreases westward across the North Pacific basin from 3.3 ± 0.5 and 2.7 ± 0.7 mol O_2 m^{-2} yr^{-1} in the Eastern and Western regions respectively to 0.7 ± 1.0

mol O_2 m^{-2} yr^{-1} in the Kuroshio region (colored bars in Figure 2.6b). These ANCP rates differ significantly from estimates of carbon export derived by considering only export from the seasonal mixed layer (black circles in Figure 2.6b), which show the opposite trend of export from the seasonal mixed layer instead increasing westward across the basin. By integrating NCP to the seasonal mixed layer depth rather than the winter ventilation depth, organic carbon (both particulate and dissolved) exported below the stratified seasonal mixed layer in spring through fall that is subsequently respired in the seasonal thermocline and ventilated during winter mixing is "counted" as exported even though the carbon is not sequestered on annual or longer time scales. There is a strong gradient across the basin in the fraction of seasonally exported carbon that is respired and subsequently ventilated before sinking below the winter ventilation depth: 88% in the Kuroshio region, 42% in the Western region, and 12% in the Eastern region. The larger fraction of carbon respired in the seasonal thermocline in the western basin is likely driven largely by deeper winter mixing (Figure 2.1), which requires organic carbon to sink further through the water column to be effectively exported. In essence although there is greater export of organic carbon from the seasonal mixed layer in the western than the eastern North Pacific, the deeper winter mixed layers in the west negate this trend and yield a lower export rate below the winter ventilation depth in the western than the eastern basin (Figure 2.6b).

Previous studies in mid-latitude regions where winter mixing extends below the euphotic zone have demonstrated the significance of winter ventilation to annual carbon export. In the North Atlantic, ~40-45% of the carbon exported from the seasonally stratified mixed layer is remineralized above the winter mixed layer depth and ventilated during winter mixing [*Körtzinger et al.*, 2008; *Quay et al.*, 2012]. Recent studies at OSP have similarly demonstrated the significance of winter processes to ANCP, with glider data showing accumulation of a sub-

mixed layer respiration signature that is ventilated during winter mixing [*Pelland,* 2015] and float and mooring data showing ~30-50% of productive season NCP offset by winter respiration [*Bushinsky and Emerson*, 2015; *Fassbender et al.*, 2016]. CESM output for the North Pacific captures the phenomenon of mixing-driven ventilation across the basin, with a greater fraction of ANCP from the seasonal mixed layer respired above the maximum annual mixed layer and not contributing to ANCP at the winter mixed layer depth in areas with deeper winter mixed layers (Figure S5a-b). These results highlight the importance of including winter observations of seasonally-exported carbon ventilated during winter mixing in estimating ANCP.

By measuring O_2/Ar throughout the full annual cycle, we were able to observe winter ventilation of O_2/Ar undersaturated waters in the Kuroshio and Western regions (Figure 2.3; Table 2.2) and account for the reduced amount of carbon exported below the winter ventilation depth as compared to the seasonal mixed layer depth. If we assumed that net physical transport of O_2 via horizontal advection or upwelling were negligible, air-sea biological oxygen flux from these O_2/Ar measurements (RHS term 1 in equation 8; orange circles in Figure 2.6b; values given in Table 2.S4) would approximate ANCP. However, physical transport of O_2 (RHS terms 2 and 3 in equation 8; rates for individual terms from equations 8 and 9 given in Table 2.S4) plays a significant though secondary role contributing to winter O_2/Ar undersaturation in the western basin (contributions of -1.6 ± 1.0, -1.2 ± 1.1, and -0.2 ± 0.2 mol O_2 m^{-2} yr^{-1} in the Kuroshio, Western and Eastern regions respectively). The trend of a more negative physical transport term to the west is due to increased rates of Ekman-driven upwelling and eastward geostrophic advection by the Kuroshio Extension [*Jayne et al.*, 2009]. Thus while a simpler budget including only air-sea biological oxygen flux effectively approximates ANCP in the Eastern region, it would underestimate ANCP in the more dynamic Kuroshio and Western

regions. Future studies investigating ANCP to the winter ventilation depth and the role of remineralization of seasonally exported carbon should take care to account for the influence of physical transport, especially in similarly dynamic regions.

2.3.5 *Export efficiency*

The NCP/GOP ratio provides a metric of the efficiency of the biological pump, defined as the fraction of photosynthetically-fixed carbon that contributes to export. Efficiency of seasonal export from the surface mixed layer can be evaluated from mixed layer NCP/GOP, while annual export efficiency can be evaluated from ANCP/euphotic-depth AGOP to determine the fraction total euphotic zone production that is exported past the winter ventilation depth. ANCP/AGOP (Figure 2.6c) is generally very low with the ratio decreasing westward across the basin from 0.07 ± 0.01 in the Eastern region to 0.01 ± 0.02 in the Kuroshio region. (The NPP/NCP ratio in carbon units would be about double the value in O_2 units (i.e. [GOP/2.7]/[NCP/1.4]). This spatial pattern opposes that of seasonal NCP/GOP in spring and summer and differs from annual NCP/GOP integrated to the base of the seasonal mixed layer, which is similar across the basin at 0.07-0.08 (Table 2.2, black circles in Figure 2.6c).

The basin-wide trend of lower seasonal export efficiency in spring and summer in the east than the west agrees with previous findings based on sediment trap, carbon, oxygen and nutrient budget, and ^{14}C-NPP estimates [*Honda*, 2003; *Harrison et al.*, 2004b]. Elevated fall NCP/GOP in the Eastern region deviates from this trend of lower seasonal export efficiency in the east than the west, but is consistent with the only previous NCP/GOP estimates in our study area (-0.01 to 0.13 in spring and 0.14 to 0.17 in fall in the Eastern region [*Juranek et al.*, 2012]), which agree with our observed NCP/GOP (0.08 ± 0.02 in spring and 0.20 ± 0.09 in fall). Seasonal NCP/GOP in all regions falls within the range previously observed from O_2 and TOI

mass balance in other ocean regions (0.06 to 0.35, summarized by *Quay et al.*, [2012]). The North Atlantic is the only region where annual export efficiency accounting for winter ventilation has previously been determined (ANCP/AGOP of 0.07 ± 0.06, *Quay et al.* [2012]). ANCP/AGOP in the Eastern region of the North Pacific matches that of the North Atlantic, while annual export efficiency in the Western and Kuroshio regions is lower than that in the North Atlantic or than seasonal export efficiency previously observed in other ocean regions. Mechanistic explanations for variations in export efficiency have generally focused on the role of biological community composition. Larger phytoplankton cells sink faster than small cells and thus are more likely to sink out of the euphotic zone before being remineralized or grazed [*Smayda*, 1970], and ballasting by biogenic silica or calcium carbonate increases sinking rates [*Armstrong et al.*, 2002; *Francois*, 2002; *Klaas and Archer*, 2002]. Based on this, we would expect higher export efficiency in the western than the eastern North Pacific, as the proportion of diatoms as compared to small cells in the phytoplankton community is greater in the west than the east [*Harrison et al.*, 2004b]. This expected trend is consistent with our and previous studies' findings for seasonal export efficiency in spring and summer but the opposite of our observed trend in annual export efficiency, which is primarily the result of differences in the depth of winter ventilation across the basin. CESM output for the North Pacific similarly shows reduced annual export efficiency in regions where remineralization of seasonally exported organic material between the base of the stratified seasonal mixed layer and deep winter mixed layer reduces ANCP (Figure S5c). Our observations demonstrate that the physical dynamics of winter ventilation are a key parameter to be more fully considered in evaluating the efficiency of the biological pump on annual time scales.

2.4 SUMMARY AND CONCLUSIONS

The vessel of opportunity sampling approach employed in this study enabled the first basin-wide estimates of GOP and NCP rates across the North Pacific throughout the full annual cycle. Comparison with previous estimates shows that productivity east of 170°W is fairly well represented by time-series measurements at OSP, but that time-series measurements at KNOT and other locations in the western subarctic underrepresent GOP and seasonal NCP in the more dynamic and spatially variable Kuroshio region west of 170°E. In particular, we observe significantly higher winter primary productivity in the Kuroshio region than previously measured. A more complete understanding of the rates and efficiency of carbon export in the western North Pacific and other highly dynamic regions across the globe will require sampling at higher spatial resolution than at single time series or mooring locations, using approaches such as vessel of opportunity sampling and autonomous measurements from bio-Argo floats [e.g. *Emerson and Bushinsky*, 2014].

The mixed layer budget approach used here to determine seasonal GOP and NCP from observed TOI and O_2/Ar demonstrates the importance of accounting for physical supply influence on tracer measurements applied over the full annual cycle. Especially in non-summer months, strong vertical diffusion and entrainment and steep vertical tracer gradients exert significant influence on mixed layer TOI and O_2/Ar. Physical supply corrections are large for GOP in fall and winter, and for NCP in winter and spring, with larger influence of physical supply in the more dynamic western basin. Improved constraints on gradients, particularly for TOI, can be achieved in future field programs by sampling the thermocline as well as the mixed layer as previously recommended by *Nicholson et al.* [2014], since the dominant physical supply

is vertical. Improved constraints on rates of advection and mixing, particularly on diffusive vertical mixing, will also improve physical supply estimates.

Throughout the spring through fall productive season, GOP and NCP are highest in the Kuroshio region and decrease eastward across the basin. AGOP is also highest in the Kuroshio and decreases eastward, in contrast to previous estimates of annual primary production rates (Table 2.3, Figure 2.6a). NCP from the seasonal mixed layer integrated over the spring through fall productive season also is highest in the Kuroshio and decreases eastward, with rates comparable to previous estimates (Table 2.4).

However, deep winter mixed layers (>200 m) in the Kuroshio and Western regions ventilate ~40-90% of the carbon exported from the seasonal mixed layer during the spring through fall productive season. Winter mixing does not penetrate as deeply in the Eastern region (<120 m) due to a strong permanent halocline [*Harrison et al.*, 1999], ventilating only ~10% of the seasonally exported carbon. As a result, annual NCP decreases westward across the basin from 2.3 ± 0.3 mol C m^{-2} yr^{-1} east of 160°W to 0.5 ± 0.7 mol C m^{-2} yr^{-1} west of 170°E, opposite the spatial trend of NCP from the seasonal mixed layer during the productive season. Our results demonstrate that annual estimates of carbon export to the deep ocean can only be resolved by accounting for winter ventilation of seasonally exported carbon in regions of deep winter mixing such as the western North Pacific. Estimates that only consider export below the shallow seasonal mixed layer during the highly stratified late spring-early fall months would tend to overestimate the contribution to annual carbon export. The ability of CESM to capture the influence of deeper winter mixing on ANCP in the North Pacific (Figure S5) indicates that global earth system model simulations could be used to investigate the role of winter ventilation

on ANCP on the global scale, although additional observational estimates of ANCP to the winter ventilation depth are needed to validate modeled rates and spatial patterns of ANCP.

Annual export efficiency (ANCP/AGOP) increases eastward across the basin, with ANCP/AGOP in the Eastern region >6× that in the Kuroshio (Figure 2.6c). This suggests that the larger phytoplankton blooms dominated by larger cells found in the western as compared to the eastern North Pacific [*Harrison et al.*, 2004b], which likely produce the observed higher seasonal export efficiencies in the west than the east in spring and summer, play a less important role than physical constraints (i.e. winter ventilation depth) in controlling export efficiency on an annual basis. This could have significant implications in projecting how future climate change will influence the strength and efficiency of the biological pump. Increased stratification of the ocean is projected to both shift the phytoplankton community towards smaller cells and to decrease the depth of winter mixing. The shift to smaller cells is expected to decrease the efficiency of export, while the decreasing depth of winter mixing would increase the efficiency of annual export. Projections of future changes to biological carbon export should account for both of these competing influences.

2.5 FIGURES AND TABLES

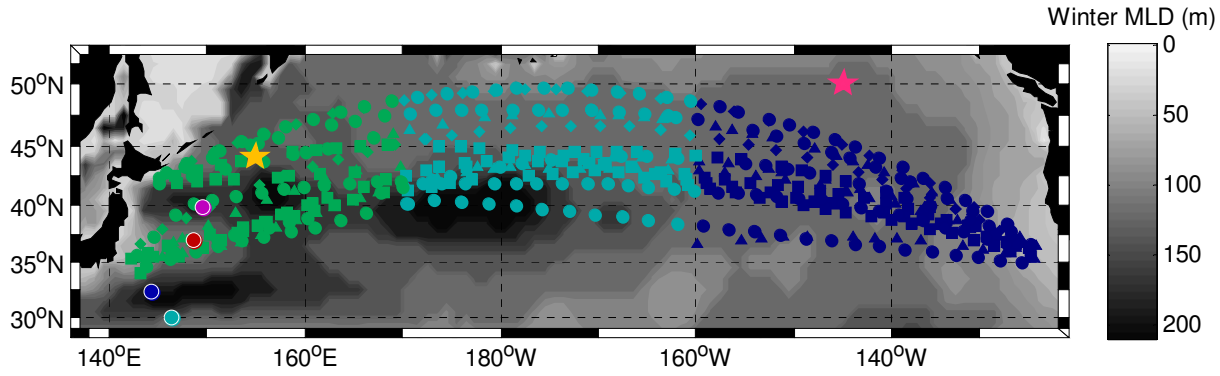

Figure 2.1: Mixed layer discrete samples collected on sixteen basin-wide transects of the North Pacific between 2008 and 2012 are divided for analysis into three regions: the Kuroshio (green), the Western region (light blue), and the Eastern region (dark blue). The annual cycle is divided by season: spring (Mar. – May, triangles), summer (June – Aug., diamonds), fall (Sept. – Nov., squares), and winter (Dec. – Feb., circles). The four colored circles outlined in white indicate depth profile samples collected in late winter 2013. Stars indicate time-series stations at KNOT (yellow) and OSP (pink), for comparison to previous measurements. Sample locations are overlain on climatological maximum winter mixed layer depth (MLD), calculated from World Ocean Atlas data (see Table 2.1 for details).

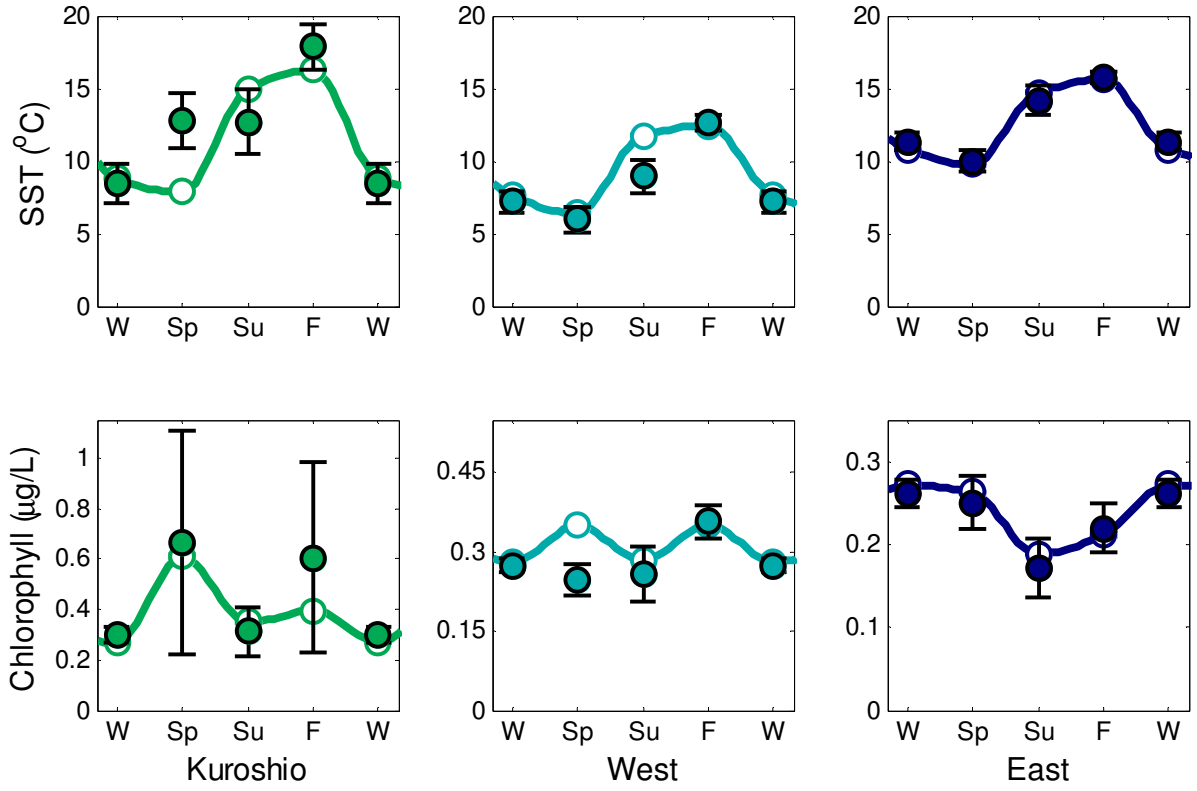

Figure 2.2: The seasonal cycle of sea surface temperature (SST, top) and chlorophyll (bottom) in each region, from MODIS satellite data. Open circles connected by solid lines show mean values over all points in the region in all three months comprising each season in every year 2008-2012. Filled circles show mean values sampled only at the locations and times when discrete samples were collected during this study. Error bars represent twice the standard error of the mean (error bars not shown are smaller than the marker size). Discrepancies between the solid and open circles reflect undersampling bias. Note the varying y-axis for chlorophyll plots.

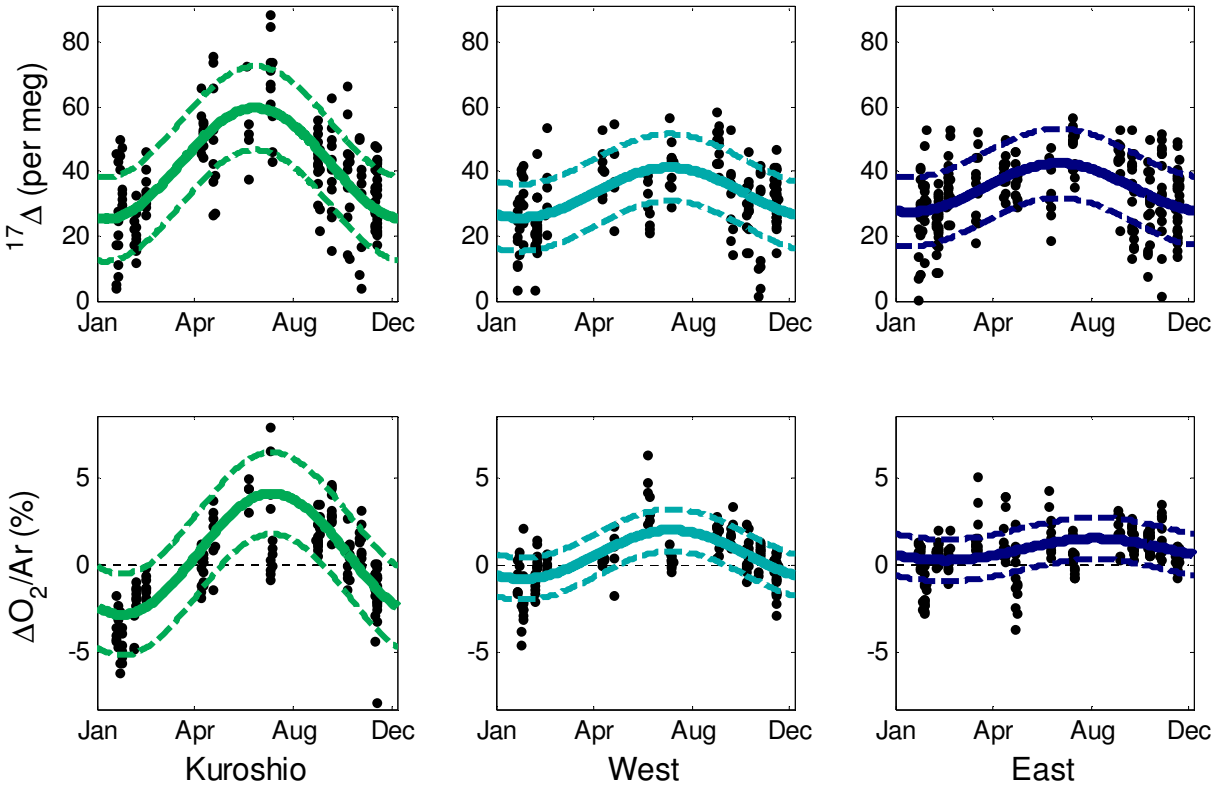

Figure 2.3: Composite annual cycle of $^{17}\Delta$ and $\Delta O_2/Ar$ in each region. Black dots show all discrete sample measurements in a given region (four samples with measured $^{17}\Delta < 0$ and four samples with measured $\Delta O_2/Ar > 9\%$ are outside the y-axis bounds). The solid line is a harmonic fit to the data describing the annual cycle and the dashed lines show the harmonic fit ± root mean squared error.

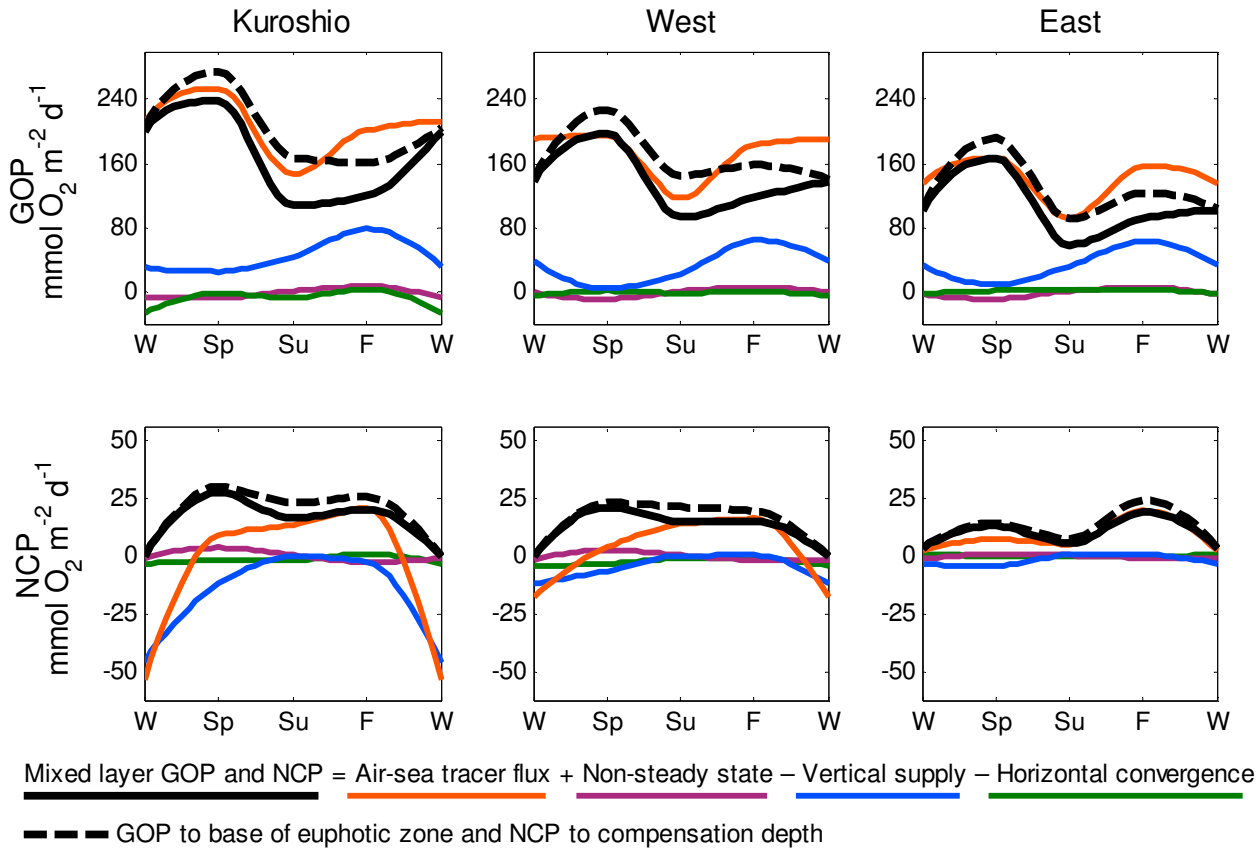

Figure 2.4: Seasonal cycle of GOP (top) and NCP (bottom) in each region, including component budget terms, calculated following equations (2) and (4) respectively. Vertical supply includes both entrainment and vertical diffusion. Horizontal convergence includes both Ekman and geostrophic transport. Upwelling is a minor contribution to the budget and is omitted for clarity. Seasonal GOP to the base of the euphotic zone and NCP to the compensation depth (where photosynthesis = respiration) include sub-mixed layer production estimated from CESM output (Figure S2). For all budget terms including uncertainty values, see Tables 2.S2 and 2.S3.

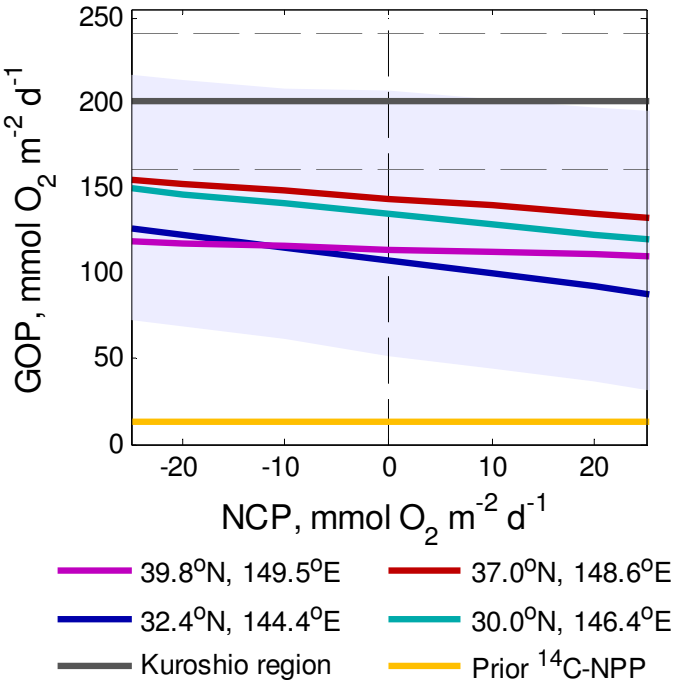

Figure 2.5: Winter GOP and NCP constrained by four depth profiles for TOI and O_2/Ar collected in late winter in the Kuroshio region (locations indicated in Figure 1; combined uncertainty bounds from all four depth profiles shaded in blue). Kuroshio region GOP from this study and previously measured ^{14}C-NPP in the region (from Table 2.3, converted to GOP using a gross O_2: net C ratio of 2.7) are plotted for comparison (uncertainty bounds shown with dashed lines, which are within the size of the line for prior ^{14}C-NPP). GOP and NCP are jointly constrained from depth profile data based on the assumption that the dominant budget terms are air-sea gas exchange and vertical supply (see text for details). Depth profile data are shown in Figure S4.

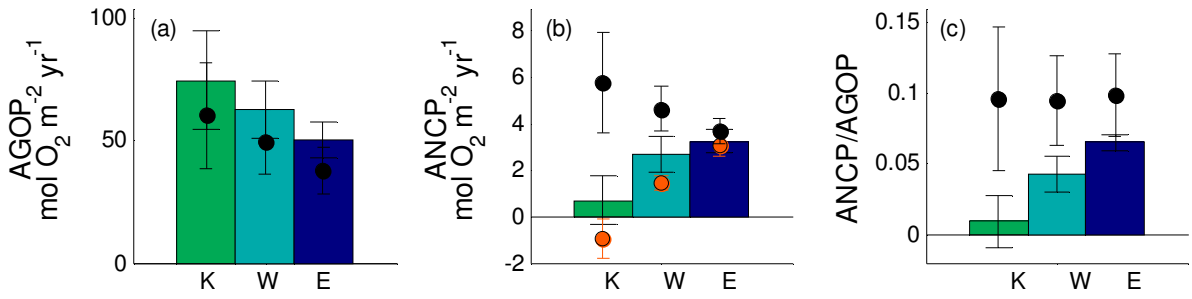

Figure 2.6: Colored bars are (a) AGOP to the base of the euphotic zone, calculated as the annual integral of air-sea flux of TOI, (b) ANCP to the winter ventilation depth, calculated following equation (8), and (c) annual export efficiency (ANCP/AGOP) in the Kuroshio (green), Western (light blue), and Eastern (dark blue) regions. Black circles are annual rates for each region determined to the base of the seasonal mixed layer (GOP calculated following equation (2) and NCP calculated following equation (4), as shown in Figure 4, each integrated over the year). Orange circles in (b) are air-sea biological oxygen flux from O_2/Ar (as shown in Figure 4) integrated over the year in each region.

Table 2.1: Data sources for NCP budget physical supply correction terms

Parameter	Data source	Spatial resolution	Time resolution
Oxygen (O_2), temperature (T), salinity (S)	World Ocean Atlas 2013 (WOA) (https://www.nodc.noaa.gov/OC5/woa13)	1° × 1°	Monthly climatology (data from 1955-2012)
Argon (Ar)	Calculated from WOA T and S [*Hamme and Emerson*, 2004]	1° × 1°	Monthly climatology (data from 1955-2012)
Mixed layer depth (z_{ml})	0.125 kg m^{-3} density increase from the surface, from WOA T and S [*Monterey and Levitus*, 1997]	1° × 1°	Monthly climatology (data from 1955-2012)
Ekman transport ($\mathbf{u_{Ek}}$)[a]	U.S. Navy Fleet Numerical Meteorology and Oceanography Center (FNMOC) data derived from synoptic surface pressure analyses (http://coastwatch.pfeg.noaa.gov/erddap/griddap/erdlasFnWPr.html)	1° × 1°	Monthly climatology (data from 2008-2012)
Geostrophic transport ($\mathbf{u_{Geo}}$)	Ssalto/Duacs absolute geostrophic velocity data from satellite altimetry, distributed by Aviso (http://www.aviso.altimetry.fr/en/data/products/sea-surface-height-products/global.html)	1/4° × 1/4°, regridded to 1° × 1°	Monthly climatology (data from 2008-2012)
Ekman-driven upwelling ($\mathbf{w_{Ek}}$) [b]	Horizontal divergence of mass due to Ekman transport ($\mathbf{u_{Ek}}$, above)	1° × 1°	Monthly climatology (data from 2008-2012)
Vertical diffusivity at the base of the mixed layer (K_z)	Winter/spring K_z determined by assuming winter NCP = 0. Summer/fall K_z scaled down from winter/spring values based on seasonal cycle observed at KEO and OSP [*Cronin et al.*, 2015].[c]	Regional	Seasonal climatology

[a] When the Ekman depth was deeper than the mixed layer, transport was scaled to only include Ekman transport within the mixed layer.
[b] When the vertical velocity is downward (downwelling), there is no effect on the mixed layer budget.
[c] Factors to scale winter/spring K_z for summer/fall are 0.1, 0.2 and 0.5 in the Kuroshio, Western and Eastern regions respectively, chosen based on the observed seasonal cycle amplitude at the Kuroshio Extension Observatory (KEO, 32.4°N, 144.6°E) and OSP [*Cronin et al.*, 2015]. Eastern region winter NCP is > 0 even when $K_z = 0$, so winter/spring Kz was chosen as 2.0×10^{-5} m^2 s^{-1}, twice background diffusivity.

Table 2.2: Summary of regional mean geochemical tracer values and productivity rates across the North Pacific[a]

Kuroshio (142°E – 170°E)								
	No. of samples	$^{17}\Delta$ (per meg)	$\Delta O_2/Ar$ (% supersaturation)	GOP		NCP		NCP/GOP
				Mixed layer	Euphotic zone	Mixed layer	Full depth	
Spring (MAM)	26	50 ± 2 (12)	1.38 ± 0.09 (3.9)	238 ± 57	274 ± 65	27 ± 7	30 ± 7	0.11 ± 0.04
Summer (JJA)	17	63 ± 3 (15)	3.10 ± 0.12 (3.5)	108 ± 33	167 ± 51	16 ± 2	23 ± 3	0.15 ± 0.05
Fall (SON)	51	38 ± 2 (16)	1.87 ± 0.04 (1.8)	120 ± 120	161 ± 161	20 ± 12	25 ± 15	0.17 ± 0.19
Winter (DJF)	73	29 ± 1 (12)	-2.38 ± 0.04 (1.7)	201 ± 45	205 ± 46	0 ± 19	0 ± 19	--
Annual	169	--	--	60 ± 22	74 ± 20	5.8 ± 2.2	0.7 ± 1.0	0.01 ± 0.02
West (170°E – 160°W)								
	No. of samples	$^{17}\Delta$ (per meg)	$\Delta O_2/Ar$ (% supersaturation)	GOP		NCP		NCP/GOP
				Mixed layer	Euphotic zone	Mixed layer	Full depth	
Spring (MAM)	20	37 ± 3 (10)	0.31 ± 0.10 (0.8)	197 ± 62	227 ± 72	21 ± 4	23 ± 5	0.11 ± 0.04
Summer (JJA)	21	37 ± 3 (9)	1.68 ± 0.10 (1.9)	93 ± 24	144 ± 37	15 ± 3	21 ± 4	0.16 ± 0.05
Fall (SON)	50	34 ± 2 (14)	1.17 ± 0.04 (0.9)	118 ± 44	158 ± 59	15 ± 3	19 ± 4	0.13 ± 0.05
Winter (DJF)	74	27 ± 1 (10)	-0.66 ± 0.04 (1.2)	137 ± 38	141 ± 39	0 ± 7	0 ± 7	--
Annual	166	--	--	49 ± 13	63 ± 12	5.2 ± 1.0	2.7 ± 0.8	0.04 ± 0.01
East (160°W – 125°W)								
	No. of samples	$^{17}\Delta$ (per meg)	$\Delta O_2/Ar$ (% supersaturation)	GOP		NCP		NCP/GOP
				Mixed layer	Euphotic zone	Mixed layer	Full depth	
Spring (MAM)	61	36 ± 2 (9)	0.64 ± 0.06 (1.5)	167 ± 23	192 ± 27	13 ± 2	14 ± 3	0.08 ± 0.02
Summer (JJA)	25	42 ± 2 (10)	1.07 ± 0.09 (1.2)	58 ± 22	90 ± 34	5 ± 1	7 ± 1	0.09 ± 0.04
Fall (SON)	68	34 ± 2 (13)	1.59 ± 0.04 (0.8)	92 ± 40	123 ± 54	19 ± 3	24 ± 4	0.20 ± 0.09
Winter (DJF)	92	27 ± 1 (11)	0.20 ± 0.03 (1.0)	102 ± 25	104 ± 25	4 ± 2	4 ± 2	--
Annual	246	--	--	38 ± 10	50 ± 7	3.7 ± 0.6	3.3 ± 0.5	0.07 ± 0.01

[a] All results are given as mean ± uncertainty, reflecting both methodological error and sampling bias (see text for details). For tracer values, 1σ variability about the mean is given in parentheses, reflecting regional variability. GOP and NCP are reported in mmol O_2 m^{-2} d^{-1} for seasonal rates and mol O_2 m^{-2} yr^{-1} for annual rates. NCP/GOP is unitless. Seasonal euphotic zone GOP and full (i.e.

compensation) depth NCP include sub-mixed layer production as estimated from CESM output (see Figure S2). Euphotic zone AGOP rates are the annually-integrated air-sea TOI flux, and full depth ANCP rates are integrated to the winter ventilation depth following equation (8). Seasonal NCP/GOP is calculated from mixed layer productivity rates and annual NCP/GOP is calculated from euphotic zone AGOP and winter ventilation depth ANCP.

Table 2.3: Net primary productivity (NPP) estimates for the Kuroshio and Eastern regions of the North Pacific[a]

	Annual	Spring	Summer	Fall	Winter
Kuroshio					
KNOT	7.5[b]	44[b]	19[b], 23[d]	14[b], 44[d]	4[b]
Elsewhere	7.3[c]	65[b], 39[c], 29[d], 111[e]	19[c], 26[d], 35[f], 39[g]	16[c], 30[d], 31[h]	6[c]
Mean ± 1σ	**7.4 ± 0.1**	**58 ± 33**	**27 ± 8**	**27 ± 12**	**5 ± 1**
This study					
Mixed layer	*22 ± 8*	*88 ± 21*	*40 ± 12*	*44 ± 44*	*74 ± 17*
Euphotic zone	*28 ± 7*	*102 ± 24*	*62 ± 19*	*60 ± 20*	*76 ± 17*
East					
OSP	14[i], 12[j], 18[k]	46[i], 35[j], 71[k]	73[i], 39[j], 71[k]	21[h], 62[i], 31[j]	24[j], 25[k]
Elsewhere		70[m], 74[m]	28[l]	26[m], 69[m]	
Mean ± 1σ	**15 ± 3**	**59 ± 18**	**53 ± 23**	**42 ± 22**	**24 ± 1**
This study					
Mixed layer	*14 ± 4*	*62 ± 9*	*22 ± 8*	*34 ± 15*	*38 ± 9*
Euphotic zone	*19 ± 3*	*71 ± 10*	*33 ± 13*	*46 ± 20*	*39 ± 9*

[a] Annual NPP in mol C m^{-2} yr^{-1}; seasonal NPP in mmol C m^{-2} d^{-1}. All previous measurements are ^{14}C or ^{13}C incubations, unless otherwise indicated. Sampling locations are noted for values from elsewhere than KNOT or OSP. We summarize previous measurements annually and seasonally in each region as the mean ± 1σ of all previous studies' mean values. GOP values from this study are converted to ^{14}C-NPP equivalent rates using a gross O_2: net C ratio of 2.7 [*Marra*, 2002].

[b] *Imai et al.* [2002], Values from KNOT as well as a May bloom near KNOT (44-45°N, 155.5-156.5°E)

[c] *Shiomoto*, [2000], 40-45°N, 150-160°E

[d] *Kawakami and Honda* [2007], Values from KNOT as well as stations K1 (51°N, 165°E) , K2 (47°N, 160°E) and K3 (39°N, 160°E)

[e] *Isada et al.*, [2010], 41-43°N, 144-147°E

[f] *Fujiki et al.*, [2011], Fast repetition rate fluorometry from profiling float at K2, calibrated with ^{13}C incubations

[g] *Elskens et al.* [2008], K2

[h] *Kawakami et al.* [2010a], Kuroshio region value from 47-51°N, 160-169°E, including K1 and K2.

[i] *Welschmeyer et al.* [1993]

[j] *Wong et al.* [1995]

[k] *Boyd and Harrison*, [1999], as presented in *Harrison et al.*, [1999]

[l] *Giesbrecht et al.*, [2012], seasonal mean from OSP and station P16 (49.3°N, 134.7°W)

[m] *Juranek et al.*, [2012], GOP from TOI, converted to NPP with a gross O_2: net C ratio of 2.7. Values from the subtropical-subarctic physical transition zone (31-43°N, 145-160°W) and the subarctic gyre (39-55°N, 145-160°W).

Table 2.4: Net community productivity (NCP) estimates for the Kuroshio and Eastern regions of the North Pacific[a]

	Annual	Productive season	Spring	Summer	Fall
Kuroshio					
KNOT		4.5[b], 5.1[e]	5[g], 2.5[h]	12[h]	10[g], 10[h]
Elsewhere		3.2[c], 2.9[d], 3.3[e], 4.0[e], 4.8[f], 2.6[h], 1.9[h], 6.3[k], 2.7[k], 6.9[k], 4.2[m], 5.3[m], 4.5[w]	7[d], 19[g], 6[h]	24[d], 10[h], 8[j]	8[g], 5[h], 4[i]
Mean ± 1σ		**4.1 ± 1.4**	**8 ± 6**	**13 ± 7**	**7 ± 3**
This study					
Mixed layer		*4.1 ± 1.6*	*19 ± 5*	*12 ± 2*	*14 ± 8*
Full depth	*0.5 ± 0.7*		*21 ± 5*	*16 ± 2*	*18 ± 10*
East					
OSP	0.7[x]	3.0[f], 2.2[l], 2.1[r], 1.6[r], 2.5[r], 2[w], 1.4[x]	35[o], 24[o]	8[n], 6[o], 21[o], 22[p], 15[r], 10[r], 17[r]	3[i], 19[o]
Elsewhere	2.2 (0.5-4)[v]	3.1[k], 1.8[m], 1.3[m]	7[n], 15[u], 2[u]	13[q], 7[q], 8[s]	3[s], 12[t], 26[t], 9[u], 22[u]
Mean ± SD	**1.5 ± 1.1**	**2.1 ± 0.6**	**17 ± 13**	**13 ± 6**	**13 ± 9**
This study					
Mixed layer		*2.6 ± 0.4*	*9 ± 2*	*4 ± 1*	*13 ± 2*
Full depth	*2.3 ± 0.3*		*10 ± 2*	*5 ± 1*	*17 ± 3*

[a] Annual and productive season NCP in mol C m^{-2} yr^{-1}; seasonal NCP in mmol C m^{-2} d^{-1}. Sampling locations are noted for values not from KNOT or OSP. We summarize previous measurements annually and seasonally in each region as the mean ± 1σ of all previous studies' mean values. NCP values from this study are converted to carbon units using a O_2: C ratio of 1.4 [*Laws*, 1991]. Full depth seasonal NCP includes sub-mixed layer production to the compensation depth, and full depth annual NCP is integrated to the winter ventilation depth.

[b] *Tsurushima et al.* [2002], Carbon and nitrate drawdown from top 100 m, May to October, 1998 and 1999

[c] *Andreev et al.* [2002], Carbon and nitrate budget in top 100 m, includes data from KNOT and central western subarctic gyre (50°N, 165-170°E)

[d] *Midorikawa et al.* [2002, 2003] Seasonal carbon and nitrate drawdown, 48°N, 165°E

[e] *Kawakami et al.* [2007], Carbon and nitrate drawdown from top 100 m, April to October. Values elsewhere than KNOT from stations K1 (51°N, 165°E) and K2 (47°N, 160°E).

[f] *Kawakami et al.* [2010], Carbon and nitrate budget in top 100 m, K2 and OSP

[g] *Kawakami et al.* [2004], Particulate carbon flux to the base of the euphotic zone from ^{234}Th, 40-50°N, 150-170°E

[h] *Kawakami and Honda* [2007], Particulate carbon flux to 100 m from ^{234}Th. Values elsewhere than KNOT from K1, K2, and K3 (39°N, 160°E). Annual values from K2 and K3.

[i] *Kawakami et al.* [2010a], Particulate carbon flux to 100 m from ^{234}Th. Kuroshio value from 47-51°N, 160-169°E, including K1 and K2.

[j] *Elskens et al.* [2008], $^{15}NO_3^-$ uptake in top 50 m at K2

[k] *Wong et al.* [2002], Carbon and nitrate mixed layer budget. Kuroshio regions are the western subarctic gyre (45-55°N, 140-160°E), southeast Japan (42-45°N, 140-160°E) and Hokkaido (35-42°N, 140-160°E); Eastern region is the Alaskan gyre (45-55°N, 140-170°W)

[l] *Wong et al.* [2002b], Nitrate drawdown from top 50 m over six month productive season

[m] *Chierici et al.* [2006], Carbon and nitrate mixed layer budget. Kuroshio regions are the Oyashio (41-47°N, 145-155°E) and western subarctic gyre (45-51°N, 155-165°E); Eastern regions are the Alaskan gyre (45-52°N, 150-165°W) and subarctic (47-51°N, 135-145°W)

[n] *Charette et al.*, [1999], Particulate carbon flux to the base of the euphotic zone from ^{234}Th. Spring value is mean along Line P in Alaskan gyre.

[o] *Wheeler*, [1993], Nitrate drawdown for spring (May) and summer (May-Sept.); $^{15}NO_3^-$ uptake for spring (May), summer (June and Aug.) and fall (Sept.), converted from to carbon units with 16 N: 106 C [*Redfield et al.*, 1963]

[p] *Varela and Harrison*, [1999], $^{15}NO_3^-$ uptake from May to September

[q] *Giesbrecht et al.*, [2012], Mixed layer O_2/Ar budget and $^{15}NO_3^-$ uptake, OSP and station P16 (49.3°N, 134.7°W)

[r] *Emerson* [1987]; *Emerson et al.* [1991]; *Emerson and Stump* [2010], O_2 and inert gas mixed layer budgets, assuming 150 day productive season from May-September

[s] *Howard et al.* [2010], O_2/Ar euphotic zone budget, 30-45°N, 145-152°W

[t] *Lockwood et al.* [2012], O_2/Ar mixed layer budget. Values from the subtropical-subarctic physical transition zone (32-45°N, 145-152°W) and the subarctic gyre (45-50°N, 145-152°W).

[u] *Juranek et al.* [2012], O_2/Ar mixed layer budget, converted to C units with an O_2: C ratio of 1.4. Values from the subtropical-subarctic physical transition zone (31-43°N, 145-160°W) and the subarctic gyre (39-55°N, 145-160°W).

[v] *Sonnerup et al.* [2013], Apparent oxygen utilization from transit time distributions, 35-50°N, 145-152°W

[w] *Fassbender* [2014]; *Fassbender et al.* [2016] Carbon and alkalinity budgets at OSP and KEO (32.3°N, 144.6°E)

[x] *Bushinsky and Emerson* [2015], O_2 budget from profiling float

2.6 SUPPLEMENTARY INFORMATION

2.6.1 *Derivation of surface mixed layer O_2/Ar budget to estimate NCP*

The surface mixed layer O_2/Ar budget used to estimate NCP (equation (4) in the main text) and the derivation shown here, are based on previous work combining oxygen and argon budgets to estimate NCP [*Craig and Hayward*, 1987; *Howard et al.*, 2010; *Lockwood*, 2013]. We write separate mass balance equations for the effects of gas exchange, physical supply and NCP on mixed layer concentrations of dissolved oxygen and argon. Since argon is an inert gas, it is not affected by NCP. Details of the physical supply terms are given in equation (7) in the main text.

$$z_{\mathrm{ml}}\frac{\partial[\mathrm{O_2}]_{\mathrm{ml}}}{\partial t} = -\mathrm{k_{O2}}\left([\mathrm{O_2}]_{\mathrm{ml}} - [\mathrm{O_2}]_{\mathrm{eq}}\right) + z_{\mathrm{ml}}\frac{\partial \mathrm{O_2}}{\partial \mathrm{t}}_{\mathrm{phys}} + \mathrm{NCP} \quad \text{(S1)}$$

$$z_{\mathrm{ml}}\frac{\partial[\mathrm{Ar}]_{\mathrm{ml}}}{\partial t} = -\mathrm{k_{Ar}}\left([\mathrm{Ar}]_{\mathrm{ml}} - [\mathrm{Ar}]_{\mathrm{eq}}\right) + z_{\mathrm{ml}}\frac{\partial \mathrm{Ar}}{\partial \mathrm{t}}_{\mathrm{phys}} \quad \text{(S2)}$$

To write a combined budget for O_2/Ar, we multiply equation (S2) by $(O_2/Ar)_{eq}$ and subtract it from equation (S1). We make the simplifying assumption that $k_{Ar} \approx k_{O2}$, based on the similarity in solubility and molecular diffusion between the two gases.

$$z_{\mathrm{ml}}\left[\frac{\partial[\mathrm{O_2}]_{\mathrm{ml}}}{\partial t} - (\mathrm{O_2/Ar})_{\mathrm{eq}}\frac{\partial[\mathrm{Ar}]_{\mathrm{ml}}}{\partial t}\right] = -\mathrm{k_{O2}}\left([\mathrm{O_2}]_{\mathrm{ml}} - (\mathrm{O_2/Ar})_{\mathrm{eq}}[\mathrm{Ar}]_{\mathrm{ml}}\right) + z_{\mathrm{ml}}\left(\frac{\partial \mathrm{O_2}}{\partial \mathrm{t}}_{\mathrm{phys}} - (\mathrm{O_2/Ar})_{\mathrm{eq}}\frac{\partial \mathrm{Ar}}{\partial \mathrm{t}}_{\mathrm{phys}}\right) + \mathrm{NCP} \quad \text{(S3)}$$

To simplify equation (S3), we represent oxygen and argon gas supersaturation following the form:

$$\Delta \mathrm{C} = \frac{[\mathrm{C}]_{\mathrm{ml}}}{[\mathrm{C}]_{\mathrm{eq}}} - 1 \quad \text{(S4)}$$

Applying the notation of equation (S4):

$$[\mathrm{O_2}]_{\mathrm{ml}} - (\mathrm{O_2/Ar})_{\mathrm{eq}}[\mathrm{Ar}]_{\mathrm{ml}} = [\mathrm{O_2}]_{\mathrm{eq}}(\Delta \mathrm{O_2} - \Delta \mathrm{Ar}) \quad \text{(S5)}$$

The O_2-Ar supersaturation difference, (ΔO_2 - ΔAr), is commonly approximated as ΔO_2/Ar (following equation (S4) here and also defined in equation (3) in the main text). Applying this approximation and substituting into the time rate of change (left hand side) term and gas exchange (first right hand side) terms in equation (S3) following equation (S5):

$$z_{\mathrm{ml}}[\mathrm{O_2}]_{\mathrm{eq}}\frac{\partial(\Delta \mathrm{O_2/Ar})}{\partial t} = -\mathrm{k_{O2}}[\mathrm{O_2}]_{\mathrm{eq}}\Delta \mathrm{O_2/Ar} + z_{\mathrm{ml}}\left(\frac{\partial \mathrm{O_2}}{\partial \mathrm{t}}_{\mathrm{phys}} - (\mathrm{O_2/Ar})_{\mathrm{eq}}\frac{\partial \mathrm{Ar}}{\partial \mathrm{t}}_{\mathrm{phys}}\right) + \mathrm{NCP} \quad \text{(S6)}$$

Rearranging equation (S6) to solve for NCP produces the form of equation (4) presented in the main text, which is also reproduced below:

$$\mathrm{NCP} = \mathrm{k}[\mathrm{O_2}]_{\mathrm{eq}}\Delta \mathrm{O_2/Ar} + \frac{\partial(\Delta \mathrm{O_2/Ar})}{\partial t}z_{\mathrm{ml}}[\mathrm{O_2}]_{\mathrm{eq}} - z_{\mathrm{ml}}\left(\frac{\partial \mathrm{O_2}}{\partial \mathrm{t}}_{\mathrm{phys}} - (\mathrm{O_2/Ar})_{\mathrm{eq}}\frac{\partial \mathrm{Ar}}{\partial \mathrm{t}}_{\mathrm{phys}}\right) \quad \text{(S7)}$$

2.6.2 *Supplementary Figures and Tables*

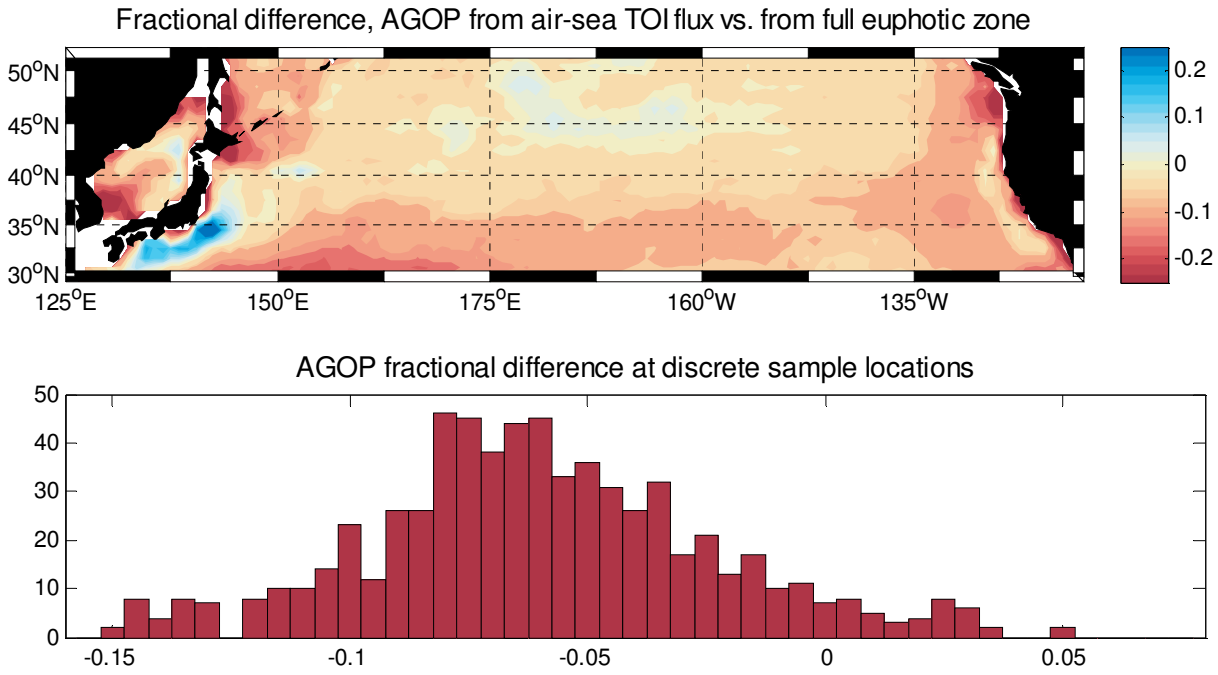

Figure 2.S1: Comparison between North Pacific annual gross oxygen production (AGOP) in the Community Earth System Model (CESM) as determined from the annually-integrated rate of air-sea TOI flux and from the model's reality for AGOP through the full euphotic zone. The spatial map (top) shows trends in the fractional difference throughout the North Pacific, where blue (red) indicates higher (lower) estimated AGOP from annually-integrated air-sea TOI flux than the model's reality of full euphotic zone AGOP. The histogram (bottom) shows fractional offsets at the locations of all discrete sample points included in this study, with a mean offset of -0.06, indicating that AGOP from air-sea TOI flux is 6% lower than the model's reality of full euphotic zone AGOP.

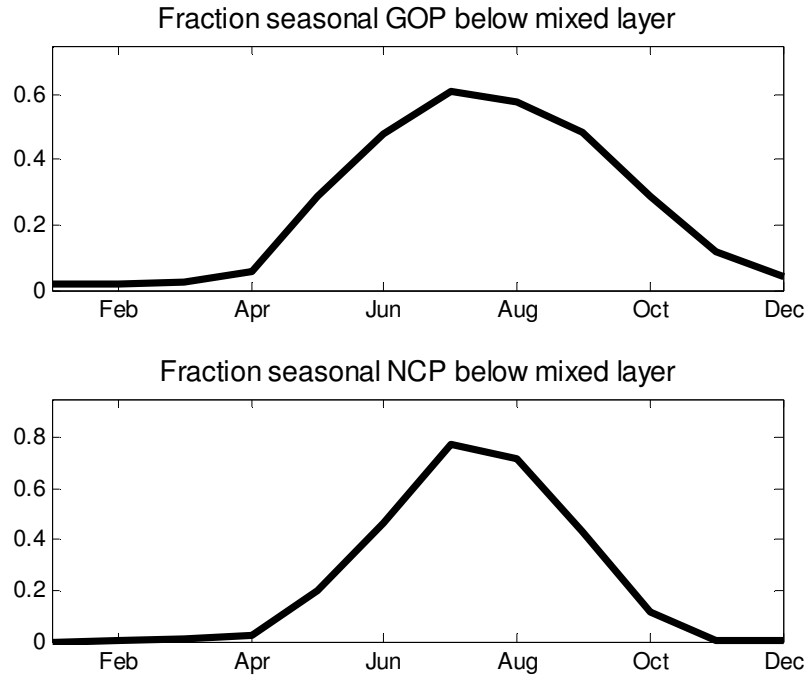

Figure 2.S2: Fraction of monthly productivity occurring below the seasonal mixed layer in the North Pacific (35– 50 °N, 142°E – 125°W) in Community Earth System Model (CESM) output, for (top) gross oxygen production (GOP) integrated through the full euphotic zone, and (bottom) net community production (NCP), integrated to the compensation depth (where photosynthesis = respiration).

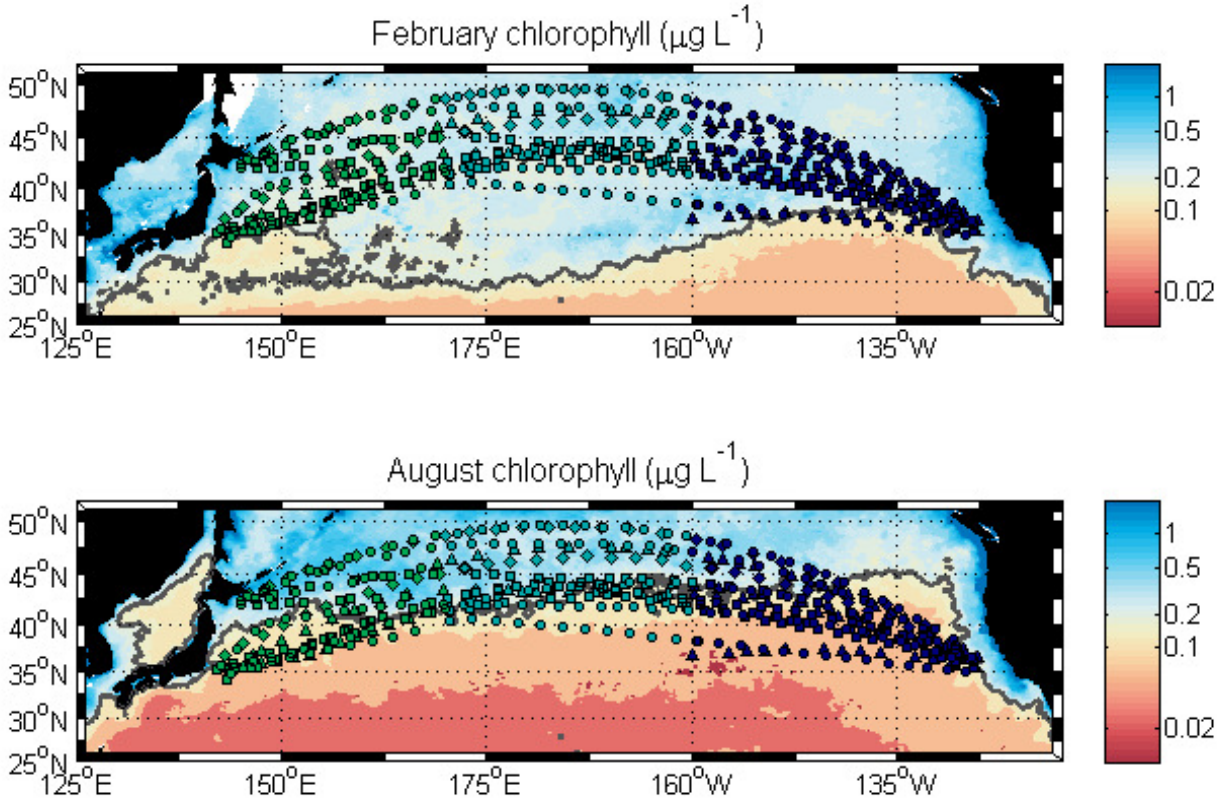

Figure 2.S3: MODIS chlorophyll concentrations (mean of 2008-2012 data) for February (top) and August (bottom), which are the months of the southernmost and northernmost locations respectively of the transition zone chlorophyll front (TZCF; defined by the 0.2 μg L^{-1} chlorophyll isopleth, dark gray line). Locations of mixed layer discrete samples from container ship transects (as in Figure 1) are shown for reference. Regions discussed in the main paper are the Kuroshio (green), the Western region (light blue), and the Eastern region (dark blue). The annual cycle is divided by season: spring (Mar. – May, triangles), summer (June – Aug., diamonds), fall (Sept. – Nov., squares), and winter (Dec. – Feb., circles).

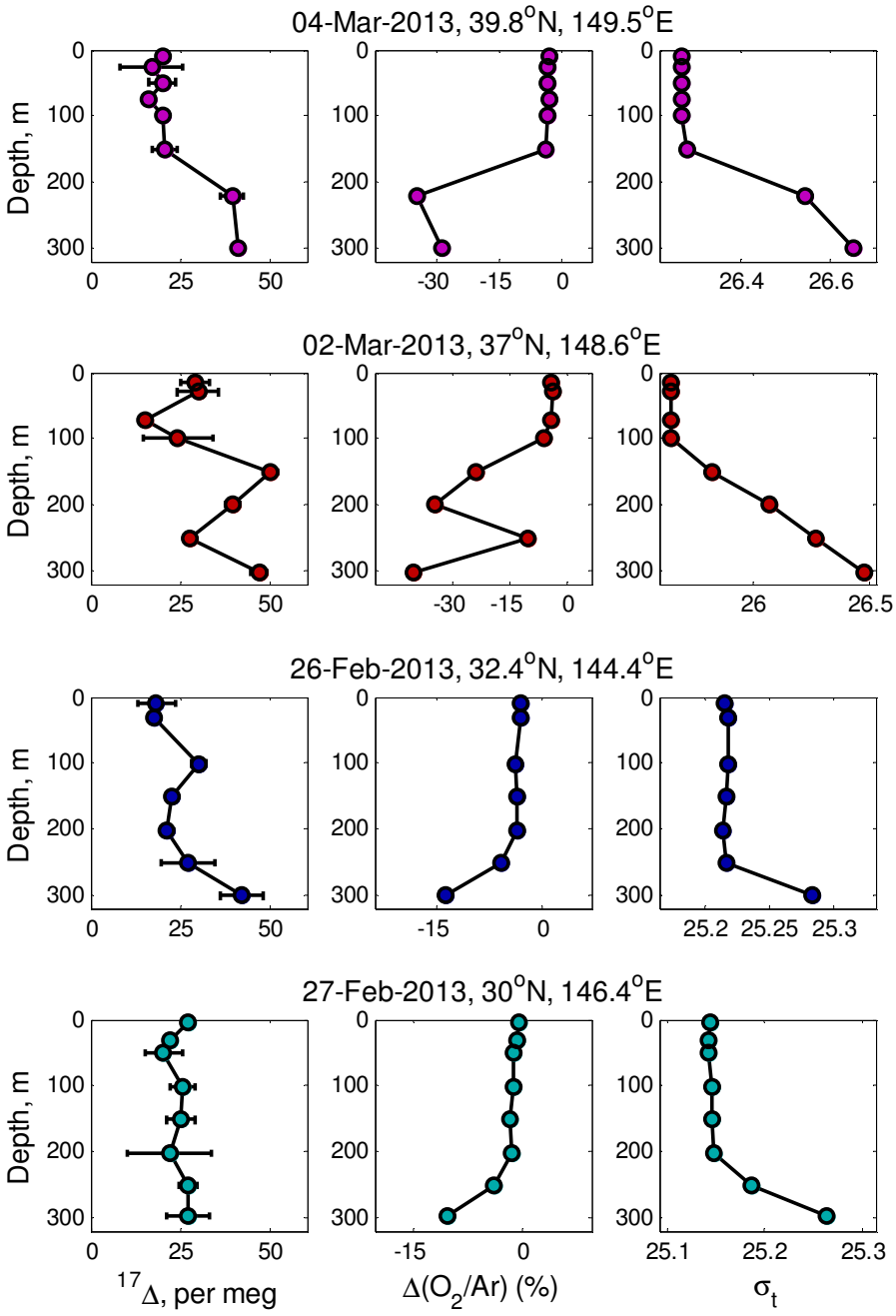

Figure 2.S4: Depth profiles for TOI ($^{17}\Delta$), $\Delta O_2/Ar$, and density (σ_t) for four locations in the Kuroshio region in late winter. Error bars show the full range between measurements from duplicate samples. Profile locations are shown in the map in Figure 1 and constraints on wintertime GOP and NCP from these data are shown in Figure 5, both with colors corresponding to those shown here.

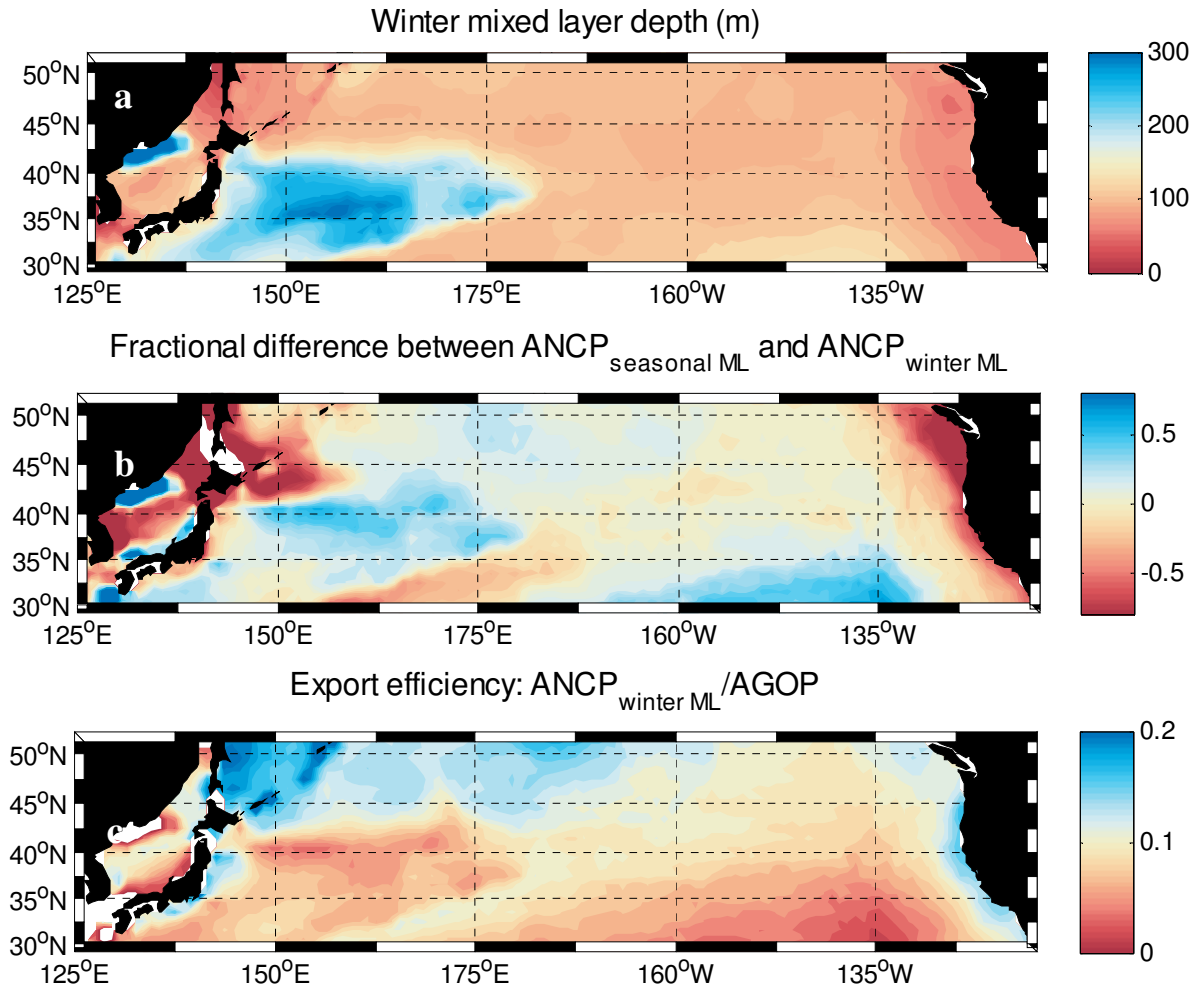

Figure 2.S5: Community Earth System Model (CESM) output in the North Pacific for a) the maximum annual (winter) mixed layer depth, b) the fractional difference between annual net community production (ANCP) to the base of the seasonally-varying mixed layer and to the winter mixed layer depth, such that positive values (blue) represent lower ANCP at the winter mixed layer depth due to remineralization of organic matter between the base of the seasonal mixed layer and the winter mixing depth and negative values (red) represent greater ANCP at the winter mixed layer depth due to a net autotrophic sub-mixed layer, and c) annual export efficiency, defined as the fraction of annual gross oxygen production (AGOP) through the full euphotic zone that contributes to ANCP to the winter mixed layer depth.

Table 2.S1: Influence of varying assumptions for winter NCP on K_z and on the mixed layer NCP budget [a]

	Winter NCP = -10	Winter NCP = -5	Winter NCP = 0 [b]	Winter NCP = 5	Winter NCP = 10
Kuroshio					
Winter K_z	3.1×10^{-4}	4.1×10^{-4}	5.1×10^{-4}	6.1×10^{-4}	7.1×10^{-4}
Spring (MAM)	22.7 ± 4.5	25.0 ± 5.4	27.2 ± 6.5	29.5 ± 7.4	31.7 ± 8.6
Summer (JJA)	16.2 ± 2.5	16.2 ± 2.4	16.2 ± 2.4	16.1 ± 2.5	16.1 ± 2.4
Fall (SON)	19.4 ± 11.5	19.7 ± 11.5	20.0 ± 11.6	20.3 ± 11.5	20.6 ± 11.5
Annual	4.4 ± 1.9	5.1 ± 2.1	5.8 ± 2.2	6.5 ± 2.6	7.2 ± 2.9
West					
Winter K_z	[c]	[c]	3.6×10^{-5}	1.4×10^{-4}	2.3×10^{-4}
Spring (MAM)	--	--	20.9 ± 4.4	24.0 ± 4.7	27.0 ± 5.2
Summer (JJA)	--	--	14.9 ± 2.6	15.0 ± 2.6	15.1 ± 2.6
Fall (SON)	--	--	15.2 ± 2.8	15.2 ± 2.9	15.2 ± 2.8
Annual	--	--	4.7 ± 1.0	5.4 ± 1.1	6.1 ± 1.2
East					
Winter K_z	[b]	[b]	[b] 2.0×10^{-5}	6.5×10^{-5}	2.2×10^{-4}
Spring (MAM)	--	--	12.8 ± 2.3	14.2 ± 2.5	19.0 ± 4.1
Summer (JJA)	--	--	5.3 ± 0.9	4.8 ± 1.0	3.1 ± 1.6
Fall (SON)	--	--	18.7 ± 3.0	18.6 ± 3.1	18.2 ± 3.1
Annual	--	--	3.7 ± 0.6	3.9 ± 0.6	4.6 ± 0.7

[a] Winter vertical diffusivity at the base of the mixed layer (K_z, units of $m^2\ s^{-1}$) is determined from a range of assumptions for winter net heterotrophy or autotrophy rates. Applying this value for K_z, resulting seasonal mixed layer NCP for spring through fall (mmol $O_2\ m^{-2}\ d^{-1}$) and annual NCP integrated to the base of the mixed layer in each season (mol $O_2\ m^{-2}\ yr^{-1}$) are also determined. The majority of the difference in the annual NCP estimated from the mixed layer budget results from changes in winter NCP, since an increase of 5 mmol $O_2\ m^{-2}\ d^{-1}$ in winter NCP adds 0.5 mol $O_2\ m^{-2}\ yr^{-1}$ to the annual mixed layer NCP. ANCP integrated to the winter ventilation depth is not affected by changes in K_z. Values based on the assumption of winter NCP = 0 are used throughout the main paper.

[b] Eliminating the influence of vertical diffusion (setting $K_z = 0$) only reduces wintertime NCP in the Eastern region to 2.9 mmol $O_2\ m^{-2}\ d^{-1}$. For the main paper, we assume K_z in the summer and fall at a background value of $1.0 \times 10^{-5}\ m^2\ s^{-1}$ and double this value for winter and spring K_z, yielding winter NCP of 3.5 mmol $O_2\ m^{-2}\ d^{-1}$.

[c] Eliminating the influence of vertical diffusion (setting $K_z = 0$) only reduces wintertime NCP in the Western region to -1.8 mmol $O_2\ m^{-2}\ d^{-1}$.

Table 2.S2: Seasonal means for each region for all terms in the gross oxygen production (GOP) mixed layer budget[a]

Kuroshio							
	Air-sea TOI flux	Non-steady state	Physical supply				Gross oxygen production (GOP)
			Vertical supply	Upwelling	Horizontal convergence	Sum	
Spring (MAM)	253 ± 55 (98)	7.7 ± 3.9	25.1 ± 12.5	-1.9 ± 1.0	-2.2 ± 1.1	21.0 ± 12.6	238 ± 57 (85)
Summer (JJA)	147 ± 24 (48)	-0.8 ± 0.4	43.7 ± 21.9	-0.6 ± 0.3	-7.4 ± 3.7	35.7 ± 22.2	108 ± 33 (33)
Fall (SON)	202 ± 113 (131)	-6.6 ± 3.2	78.3 ± 39.2	0.0 ± 0.0	3.0 ± 1.5	81.3 ± 39.2	120 ± 119 (103)
Winter (DJF)	212 ± 40 (163)	8.0 ± 4.0	31.4 ± 15.7	8.2 ± 4.1	-25.6 ± 12.8	14.0 ± 20.7	201 ± 45 (190)
West							
	Air-sea TOI flux	Non-steady state	Physical supply				Gross oxygen production (GOP)
			Vertical supply	Upwelling	Horizontal convergence	Sum	
Spring (MAM)	195 ± 62 (85)	9.4 ± 4.7	3.6 ± 1.8	1.5 ± 0.8	1.1 ± 0.5	6.2 ± 2.0	197 ± 62 (79)
Summer (JJA)	117 ± 21 (54)	-0.4 ± 0.2	22.4 ± 11.2	2.1 ± 1.1	-2.1 ± 1.0	22.5 ± 11.3	93 ± 24 (38)
Fall (SON)	183 ± 30 (104)	-5.1 ± 2.5	64.0 ± 32.0	-1.5 ± 0.7	-0.2 ± 0.1	62.2 ± 32.0	118 ± 44 (71)
Winter (DJF)	191 ± 32 (126)	1.0 ± 0.5	38.9 ± 19.4	10.2 ± 5.1	-5.5 ± 2.8	43.6 ± 20.3	137 ± 38 (93)
East							
	Air-sea TOI flux	Non-steady state	Physical supply				Gross oxygen production (GOP)
			Vertical supply	Upwelling	Horizontal convergence	Sum	
Spring (MAM)	167 ± 23 (64)	9.4 ± 4.7	8.8 ± 4.4	-1.8 ± 0.9	1.2 ± 0.6	8.2 ± 4.5	167 ± 23 (58)
Summer (JJA)	91 ± 15 (42)	-0.8 ± 0.4	32.3 ± 16.2	-2.3 ± 1.1	2.3 ± 1.1	32.3 ± 16.2	58 ± 22 (26)
Fall (SON)	156 ± 24 (99)	-4.9 ± 2.5	63.3 ± 31.6	-7.8 ± 3.9	2.5 ± 1.3	58.0 ± 31.9	92 ± 40 (57)
Winter (DJF)	134 ± 18 (83)	3.4 ± 1.7	33.6 ± 16.8	2.2 ± 1.1	-2.5 ± 1.2	33.4 ± 16.9	102 ± 24 (57)

[a] All GOP budget terms in units of mmol O_2 m^{-2} d^{-1}. Uncertainty, incorporating methodological error and undersampling bias, is given for each budget term (details in text, section 2.5). The standard deviations of all discrete points included in the calculated means for air-sea TOI flux and of GOP, representing spatial and temporal variability in the region, are given in parentheses. All terms are calculated following equation (2), which can be represented as: GOP = Air-sea TOI flux + Non-steady state – Physical supply of TOI.

Table 2.S3: Seasonal means for each region for all terms in the net community production (NCP) mixed layer budget[a]

Kuroshio									
	Air-sea O_2/Ar flux	Non-steady state	Physical supply						Net community production (NCP)
			Entrainment	Vertical diffusion	Upwelling	Ekman convergence	Geostrophic convergence	Sum	
Spring (MAM)	8.9 ± 2.0 (27.1)	3.6 ± 1.8	-0.5 ± 0.2	-11.7 ± 5.8	-0.3 ± 0.2	0.2 ± 0.1	-2.3 ± 1.1	-14.5 ± 6.0	27.2 ± 6.5 (29.5)
Summer (JJA)	13.3 ± 2.2 (12.4)	0.5 ± 0.2	0.0 ± 0.0	-0.2 ± 0.1	0.0 ± 0.0	-0.1 ± 0.1	-1.9 ± 1.0	-2.2 ± 1.0	16.2 ± 2.4 (17.6)
Fall (SON)	20.5 ± 11.4 (14.9)	-2.6 ± 1.3	-1.3 ± 0.6	-1.4 ± 0.7	-0.1 ± 0.0	-0.1 ± 0.0	1.1 ± 0.5	-1.7 ± 1.1	20.0 ± 11.6 (16.5)
Winter (DJF)	-53.0 ± 9.8 (49.2)	-0.8 ± 0.4	-20.4 ± 10.2	-25.1 ± 12.6	-2.8 ± 1.4	0.4 ± 0.2	-3.9 ± 1.9	-51.8 ± 16.4	0.0 ± 19.1 (85.4)
West									
	Air-sea O_2/Ar flux	Non-steady state	Physical supply						Net community production (NCP)
			Entrainment	Vertical diffusion	Upwelling	Ekman convergence	Geostrophic convergence	Sum	
Spring (MAM)	3.8 ± 1.7 (10.6)	2.6 ± 1.3	-5.6 ± 2.8	-0.8 ± 0.4	-3.9 ± 2.0	0.0 ± 0.0	-3.5 ± 1.7	-13.8 ± 3.9	20.9 ± 4.4 (24.0)
Summer (JJA)	13.5 ± 2.5 (15.3)	0.4 ± 0.2	0.0 ± 0.0	0.0 ± 0.0	-0.3 ± 0.1	0.1 ± 0.1	-1.2 ± 0.6	-1.3 ± 0.6	14.9 ± 2.6 (17.2)
Fall (SON)	16.0 ± 2.7 (12.6)	-1.6 ± 0.8	0.4 ± 0.2	0.0 ± 0.0	-0.1 ± 0.1	0.4 ± 0.2	-1.2 ± 0.6	-0.6 ± 0.7	15.2 ± 2.8 (11.2)
Winter (DJF)	-17.7 ± 3.1 (29.7)	-1.7 ± 0.8	-10.2 ± 5.1	-1.8 ± 0.9	-4.2 ± 2.1	-0.6 ± 0.3	-3.7 ± 1.8	-20.5 ± 5.9	0.0 ± 6.7 (33.6)
East									
	Air-sea O_2/Ar flux	Non-steady state	Physical supply						Net community production (NCP)
			Entrainment	Vertical diffusion	Upwelling	Ekman convergence	Geostrophic convergence	Sum	
Spring (MAM)	7.4 ± 1.2 (16.4)	0.8 ± 0.4	-3.8 ± 1.9	-0.6 ± 0.3	-0.2 ± 0.1	0.2 ± 0.1	-0.2 ± 0.1	-4.6 ± 1.9	12.8 ± 2.3 (18.7)
Summer (JJA)	5.0 ± 0.9 (7.7)	0.3 ± 0.1	0.1 ± 0.1	0.2 ± 0.1	0.0 ± 0.0	-0.1 ± 0.0	-0.3 ± 0.1	0.1 ± 0.2	5.3 ± 0.9 (8.1)
Fall (SON)	19.4 ± 3.0 (9.6)	-0.9 ± 0.4	0.4 ± 0.2	0.0 ± 0.0	0.0 ± 0.0	-0.1 ± 0.0	-0.4 ± 0.2	0.0 ± 0.3	18.7 ± 3.0 (11.4)
Winter (DJF)	2.0 ± 0.4 (16.2)	-1.4 ± 0.7	-2.7 ± 1.4	-0.6 ± 0.3	-0.5 ± 0.3	0.0 ± 0.0	0.9 ± 0.5	-3.0 ± 1.5	3.5 ± 1.7 (17.7)

[a] All NCP budget terms in units of mmol O_2 m^{-2} d^{-1}. Uncertainty, incorporating methodological error and undersampling bias, is given for each budget term (details in text, section 2.5). The standard deviations of all discrete points included in the calculated means for air-sea O_2/Ar flux and of NCP, representing spatial and temporal variability in the region, are given in parentheses. All terms are calculated following equation (4), which can be represented as: NCP = Air-sea O_2/Ar flux + Non-steady state – Physical supply of O_2/Ar.

Table 2.S4: Annual means for each region for all terms in the annual GOP and NCP budgets[a]

		Kuroshio	West	East
AGOP budget				
Air-sea TOI flux (euphotic zone AGOP)		74.3 ± 20.1	62.6 ± 11.8	50.1 ± 7.2
Vertical supply		16.3 ± 17.9	14.3 ± 11.8	12.6 ± 14.4
Upwelling		0.5 ± 1.5	1.1 ± 1.9	-0.9 ± 1.6
Horizontal convergence		-2.9 ± 4.9	-0.6 ± 1.1	0.3 ± 0.8
Mixed layer annual GOP		60.0 ± 21.7	49.3 ± 13.2	37.5 ± 9.5
ANCP budget				
Air-sea O_2/Ar flux		-0.95 ± 1.19	1.42 ± 0.32	3.09 ± 0.48
Mixed layer horizontal convergence	Ekman	0.03 ± 0.08	0.00 ± 0.13	0.01 ± 0.04
	Geostrophic	-0.64 ± 0.91	-0.87 ± 0.97	0.00 ± 0.19
Sub-mixed layer horizontal convergence	Ekman	-0.01 ± 0.00	0.00 ± 0.00	-0.04 ± 0.02
	Geostrophic	-0.06 ± 0.03	0.52 ± 0.26	-0.07 ± 0.03
Upwelling across base of winter mixed layer		-0.97 ± 0.49	-0.90 ± 0.45	-0.07 ± 0.03
ANCP to winter ventilation depth		0.70 ± 1.02	2.68 ± 0.76	3.26 ± 0.48

[a] All budget terms in units of mol O_2 m^{-2} yr^{-1}. Uncertainty, incorporating methodological error and undersampling bias, is given for each budget term (details in text, section 2.5). Euphotic zone AGOP is equivalent to the annual air-sea TOI flux. Mixed layer annual GOP (calculated as the annual integral of the seasonal GOP budget following equation 2) = Annual air-sea TOI flux – Vertical supply – Upwelling – Horizontal convergence. ANCP to the winter ventilation depth (calculated following equation 8) = Annual air-sea O_2/Ar flux – Mixed layer horizontal convergence – Sub-mixed layer horizontal convergence – Upwelling across the base of the winter mixed layer.

Chapter 3.

Discrepant estimates of primary and export production from satellite algorithms, a biogeochemical model, and geochemical tracer measurements in the North Pacific Ocean

3.1 INTRODUCTION

Photosynthetic primary production generates the fixed organic carbon that supports nearly all marine food webs. A fraction of this carbon is exported from the surface ocean, sequestering it in the deep ocean and thus influencing the global carbon cycle. Given the scarcity of observational data to constrain both primary and export production (PP and EP), satellite-based algorithms and global biogeochemical models are widely used to fill these gaps and enable global-scale analysis of the rates and spatial patterns of marine PP and EP [e.g. *Laufkötter et al.*, 2013; *Siegel et al.*, 2014].

Satellite- and model-based global estimates of PP and EP are essential pieces of our understanding of the ocean's carbon cycle, but given the limited observational estimates available for validation, questions remain as to how well they represent true rates and spatial patterns of PP and EP. A number of previous studies have compared satellite-based PP with geochemical estimates based on ^{14}C-PP incubations [*Carr et al.*, 2006; *Saba et al.*, 2011; *Westberry and Behrenfeld*, 2014] and *in situ* triple oxygen isotopes [e.g., *Juranek and Quay*, 2013]. *Stukel et al.* [2015] recently compared export efficiency (e-ratio, defined as EP/PP) algorithms with observations at process study locations. However, global annual EP estimates from satellite-based approaches and global biogeochemical models range widely (~6-13 Pg C per

year, [*Laws et al.*, 2011; *Siegel et al.*, 2014; *Laufkötter et al.*, 2015]), indicating that further work is needed to improve our consensus on current EP rates.

Recent work comparing geochemical and satellite-based EP estimates at Ocean Station Papa (OSP, 50°N, 145°W) in the eastern subarctic gyre and the Hawaii Ocean Time-series Station ALOHA (22.75°N, 158°W) in the subtropical gyre of the North Pacific indicated that a carbon-based PP model [*Westberry et al.*, 2008] combined with the *Laws et al.* [2000] e-ratio model matches geochemical EP estimates in both locations [*Emerson*, 2014]. However, no previous work to our knowledge has compared simultaneous year-round PP, EP and EP/PP (e-ratio) observational-based estimates with satellite algorithm- or model-based estimates across broad ocean regions. We find that neither a biogeochemical model nor any single commonly-used satellite-based algorithm matches the PP, EP and e-ratio determined from geochemical measurements throughout the entire North Pacific over the full annual cycle.

3.2 METHODS

We compare PP, EP and e-ratios estimated from geochemical measurements, satellite-based algorithms, and a dynamic global ocean model with embedded ecosystem and biogeochemistry components, with details of each approach described below. Comparisons are conducted over the full annual cycle at two time-series stations (OSP and ALOHA) and in three regions spanning the entire North Pacific basin in the transition zone and subarctic gyre (35°N–50°N, 142°E–125°W; Figure 3.1).

3.2.1 *Productivity estimation approaches*

Long-term sampling at OSP and ALOHA provides geochemical estimates of PP from ^{14}C-PP incubations (compiled for OSP by *Palevsky et al.*, [2016]; available for ALOHA from http://hahana.soest.hawaii.edu/hot/hot-dogs) and of EP from oxygen, nitrate, and carbon isotope mass balance [*Emerson*, 2014]. Basin-wide geochemical PP, EP and e-ratio estimates based on surface ocean triple oxygen isotope and O_2/Ar measurements (n=581) collected during 16 container ship crossings of the North Pacific from 2008-2012 have recently been described in detail [*Palevsky et al.*, 2016]. All PP estimates are converted to values equivalent to 24-hour ^{14}C-PP incubations, representing net primary production (total photosynthesis minus autotrophic respiration) through the full euphotic zone (details in Table 3.1). EP is determined from the seasonally-varying surface mixed layer and, for the container ship regions, also determined seasonally at the compensation depth and annually at the winter ventilation depth. E-ratios are calculated from separate estimates of PP and EP. For maximal comparability between geochemical estimates and other approaches, globally-available satellite data and model output were extracted from a 2.5° box centered on each time-series site in all months, and for the container ship regions from a 1/3° box at the locations and months corresponding to each geochemical measurement and compiled for each region and season following the same procedure as the geochemical data compilation.

Satellite-based EP estimates require two independent algorithms: one to estimate PP and a separate algorithm to estimate the e-ratio, where EP = PP × e-ratio. Each PP and e-ratio model can be combined to produce a unique EP model. All satellite-based PP and e-ratio estimates for this study use MODIS Aqua R2014 monthly products (available from http://www.science.oregonstate.edu/ocean.productivity). The two most commonly used PP

algorithms are the Vertically Generalized Production Model (VGPM, [*Behrenfeld and Falkowski*, 1997]) and the Carbon-based Production Model (CbPM, [*Behrenfeld*, 2005; *Westberry et al.*, 2008]). Both algorithms estimate integrated PP rates through the full euphotic zone. The VGPM combines measured surface chlorophyll concentrations and photosynthetically-available radiation with an estimate of euphotic depth and an empirically-determined relationship between sea surface temperature (SST) and carbon assimilation efficiency determined from ^{14}C-PP data. The CbPM uses backscattering-based estimates of phytoplankton biomass to produce a PP model that accounts for environmental condition-specific variations in carbon:chlorophyll ratios. E-ratio algorithms predict the fraction of PP exported from a given depth horizon based on satellite-measured SST, chlorophyll, and PP from the algorithms above. Here, we consider three widely-used e-ratio algorithms: 1) the pelagic food web model of *Laws et al.* [2000] (hereafter Laws00), which includes both particulate and dissolved organic carbon (POC and DOC) export from the euphotic zone, and was validated using geochemical data from 11 process study sites, 2) the empirical model of *Dunne et al.* [2005, 2007] (hereafter Dunne07), based on a compilation of field measurements using a range of methods adjusted to represent POC export from the euphotic zone, and 3) the empirical model of *Henson et al.* [2011] (hereafter Henson11), based on a compilation of ^{234}Th measurements representing POC export below 100 m.

The global biogeochemical model used here is the ocean component of the Community Earth System Model (CESM) version 1.1.1, run with an embedded biogeochemistry and ecosystem module (the Biogeochemical Elemental Cycling model [*Moore et al.*, 2002, 2004]). The model includes four phytoplankton functional groups, multiple potentially limiting nutrients (N, P, Fe), a single zooplankton class, and DOC and sinking POC pools. PP, EP and e-ratios in previous and current versions of this model have been evaluated through comparison with

existing data sets [*Moore et al.*, 2002, 2004, 2013; *Doney et al.*, 2009b; *Friedrichs et al.*, 2009]. However, the scarcity of direct observational estimates has limited previous comparisons of CESM output to process study locations or satellite-derived global PP (VGPM). CESM simulations presented here represent repeated normal year forcing run to equilibrium conditions in the surface ocean and thermocline after a 200-year spin up (for full details, see *Nicholson et al.* [2014]). This CESM output includes depth-resolved photosynthesis and respiration rates, which were used to determine PP, e-ratio and EP for a range of depth criteria (seasonal mixed layer, euphotic zone, compensation depth, and winter mixed layer) needed for optimal comparability to the geochemical estimates. Standard runs for model intercomparison projects such as the Coupled Model Intercomparison Project (CMIP5) [*Taylor et al.*, 2012] have not routinely archived the depth-resolved data needed for this type of comparison, limiting analysis across a wide range of models. We recommend that future model intercomparison projects extend standard output variables to enable monthly depth-resolved PP, EP and e-ratio estimates.

3.2.2 *Comparability between EP and e-ratio estimation approaches*

EP and e-ratio estimates vary with the integration depth criterion chosen. In stratified conditions when the mixed layer is shallower than the euphotic layer, PP can exceed respiration in the sub-mixed layer euphotic zone and contribute additional EP excluded from mixed layer-based EP estimates. Seasonal EP integrated to the compensation depth (where gross photosynthesis and community respiration rates are equal) represents the maximum EP of all possible depth criteria. In nearly all cases with shallow mixed layers, EP at the base of the euphotic zone (the Laws00 and Dunne07 depth criterion) will be greater than EP at the base of the seasonal mixed layer but less than EP at the compensation depth. E-ratios, however, are

much more sensitive to the chosen depth criterion since they consistently decrease with depth, such that deeper depth criteria (i.e. 100 m for Henson11) produce lower e-ratios.

Additionally, EP estimates to the base of the euphotic zone or 100 m are only meaningful when the mixed layer is shallower than the chosen depth criterion. When the mixed layer is deeper, organic material must still sink out of the mixed layer to be seasonally exported from the surface ocean. For exported organic material to be effectively sequestered from the atmosphere on annual or multi-annual time scales, it must sink deep enough to avoid being remineralized and ventilated to the atmosphere during deep winter mixing. Geochemical and CESM EP estimates from the container ship regions account for winter ventilation; however, satellite-based EP cannot be evaluated to the winter ventilation depth using current e-ratio algorithms.

3.3 RESULTS

3.3.1 *Time-series stations OSP and ALOHA*

Geochemical, satellite algorithm, and CESM estimates of annual PP, e-ratio and EP are compared at time-series stations in the eastern subarctic (OSP) and subtropical (ALOHA) North Pacific (Figure 3.2). Geochemical estimates from ^{14}C-PP incubations yield comparable annual PP at OSP and ALOHA (14-15 mol C m^{-2} yr^{-1}). The two satellite-based algorithms predict conflicting relative PP between the two stations, with the VGPM estimating 38% lower annual PP at ALOHA while the CbPM estimates 36% lower annual PP at OSP. CbPM-PP more closely matches geochemical PP at ALOHA while VGPM-PP more closely matches geochemical PP at OSP, but neither matches geochemical PP at both stations. CESM, similar to the CbPM, yields greater annual PP at ALOHA than OSP.

Canonically, lower e-ratios are expected in the subtropics than the subarctic due to faster recycling in warmer waters and a phytoplankton community dominated by smaller cells [*Passow and Carlson*, 2012]. This canonical pattern is evident in lower e-ratios predicted by CESM and satellite-based e-ratio algorithms at ALOHA (0.03-0.17) than at OSP (0.10-0.44) (Figure 3.2). In contrast, geochemical-based e-ratios are slightly higher at ALOHA (0.19) than OSP (0.15). Although the geochemically-based e-ratio is most closely approximated at ALOHA by the Laws00 algorithm and at OSP by the Henson11 algorithm, none of the three e-ratio algorithms nor CESM match geochemical e-ratios at both sites.

Geochemical estimates of annual EP from the seasonally-varying mixed layer are comparable at OSP and ALOHA (2.3 ± 0.6 and 2.5 ± 0.7 mol C m^{-2} yr^{-1} respectively; *Emerson* [2014]). The many potential permutations combining individual satellite-based PP and e-ratio algorithms provide a wide range of annual EP estimates (Figure 3.2). At ALOHA, however, the only combination that closely approximates geochemically-determined EP is the CbPM PP + Laws00 e-ratio. Since the CbPM and Laws00 algorithms also effectively approximate geochemical observations at ALOHA for PP and e-ratio respectively, this is an appropriate approach to estimate EP at ALOHA, and perhaps more broadly in the subtropical North Pacific. At OSP, the CbPM+Laws00 combination yields annual EP (3.2 ± 0.7 mol C m^{-2} yr^{-1}; 2003-2013 mean±1σ) that agrees within uncertainty with geochemical estimates (2.5 ± 0.7 mol C m^{-2} yr^{-1}) as previously observed by *Emerson* [2014]. However this agreement is a fortuitous combination of underestimated PP from the CbPM and overestimated e-ratio from Laws00 for OSP. Other approaches (CbPM+Dunne07, VGPM+Henson11, or CESM) more closely approximate annual EP at OSP, but no single combination successfully matches geochemical-based estimates of PP, EP and e-ratio at both OSP and ALOHA.

3.3.2 *Basin-wide comparisons across the North Pacific*

Geochemical, satellite algorithm, and CESM estimates for PP, e-ratio, and EP are compared to geochemical estimates [*Palevsky et al.*, 2016] in three broad container ship-sampled regions (boundaries shown in Figure 3.1) across the basin both throughout the seasonal cycle (Figure 3.3) and annually (Figure 3.4). In all three regions, satellite algorithm and CESM PP estimates are generally lower than the geochemical observation-based PP estimates, with the largest discrepancies during winter and spring. The geochemically-determined rates show a spring PP maximum in each region, with fairly comparable PP rates in summer, fall and winter. In contrast, the satellite algorithms and CESM generally produce PP seasonal cycles with a winter minimum and summer maximum, consistent with light-limited growth conditions in the subarctic [*Matsumoto et al.*, 2016; *Sasai et al.*, 2016]. However, in nutrient-limited conditions in the subtropical North Pacific, winter shoaling of the nitracline can lead to maximum annual PP rates in winter [*Matsumoto et al.*, 2016]. The geochemically-determined PP is consistent with mixed nutrient- and light-limitation at the boundary between the subtropics and subarctic.

Due largely to discrepancies in winter and spring, both the satellite algorithms and CESM predict lower annual PP than the geochemical-based estimates in all regions (Figure 3.4), with the least discrepancy in the VGPM and the greatest in the CbPM. The VGPM, CbPM and CESM all reproduce the geochemically-observed westward increase in annual PP across the basin, though the magnitude of the trend is matched only by the VGPM, while the CbPM and CESM predict a smaller westward increase. Integrated across all three regions, mean annual PP rates determined based on geochemical observations are significantly higher than those estimated by other approaches (1.5× VGPM, 2.7× CbPM, and 1.7× CESM).

Dunne07 and Laws00 e-ratios at the base of the euphotic zone are both roughly within the range of geochemical e-ratio estimates at the base of the seasonal mixed layer (Figure 3.3), with the Dunne07 algorithm predicting e-ratios 15-35% lower than the Laws00 algorithm (consistent with the Dunne07 algorithm excluding DOC, which is on order ~20% of total export [*Hansell and Carlson*, 1998]). In contrast, Henson11 e-ratios (representing ^{234}Th-based estimates of POC export at 100 m) are significantly lower than the geochemically-determined e-ratios at the base of the mixed layer, which in part would be expected from POC flux attenuation between the base of the mixed layer and 100 m. All e-ratio algorithms predict relatively constant e-ratios throughout the year, whereas CESM predicts much higher e-ratios in spring and summer than in fall and e-ratios (and EP) near or below zero in winter. In contrast, geochemically-determined e-ratios do not show elevated values in spring, although there is significant uncertainty in the seasonal estimates. On an annual basis, Dunne07 e-ratios agree with geochemically-based e-ratios from the seasonal mixed layer in all three regions whereas the Laws00 estimates are consistently higher and Henson11 estimates are consistently lower (Figure 3.4).

No single satellite algorithm combination nor CESM matches geochemical estimates of EP from the mixed layer (or compensation depth) in all seasons and regions (Figure 3.3). Because it underestimates PP, the CbPM produces EP rates that are significantly lower than geochemical estimates in both spring and fall when combined with any e-ratio algorithm. Similarly, since the Henson11 algorithm estimates lower e-ratios than the geochemical approach, it produces EP rates that are consistently lower than geochemical estimates in all seasons, whether combined with VGPM or CbPM PP. CESM EP estimates show stronger spring to fall seasonality than the geochemical and satellite-based estimates, which is mainly a result of consistently underestimated EP in fall. The only approach that agrees with geochemically-

determined annual EP from the mixed layer in all three regions is the VGPM+Dunne07 combination (Figure 3.4), which also yielded the closest match to annual EP at OSP.

3.4 DISCUSSION

3.4.1 *Primary production*

The VGPM comes closest to successfully reproducing geochemically-observed PP rates at OSP and in the container ship regions, while the CbPM underestimates PP as compared to the geochemically-determined rates. Similarly, a previous study in the Gulf of Alaska showed that VGPM-based EP matched O_2/Ar-based estimates of EP in a springtime high-productivity hotspot whereas it was not detected in CbPM-based EP [*Palevsky et al.*, 2013]. However, the VGPM significantly underestimates PP in the subtropics (Figure 3.2) and also underestimates winter and spring PP in the container ship regions (Figure 3.3). This may reflect an inability of the VGPM's single empirical relationship between SST and photosynthetic assimilation efficiency to represent all phytoplankton physiological variations across regions and throughout the seasonal cycle [*Westberry and Behrenfeld*, 2014].

CbPM underestimates of PP in the transition zone and subarctic North Pacific may reflect physiological effects of photoacclimation and iron stress not accounted for in existing satellite models [*Behrenfeld et al.*, 2009, 2015; *Westberry et al.*, 2016]. The CbPM photoacclimation model underestimates PP when mixed layers extend below the euphotic zone during winter and early spring because it does not account for the effect of total darkness below the euphotic zone on phytoplankton carbon:chlorophyll ratios [*Behrenfeld et al.*, 2015; *Westberry et al.*, 2016]. This is consistent with the larger discrepancy between CbPM and geochemical PP estimates in winter and spring, particularly in regions of deep winter mixing in the western basin (Figure 3.3).

Additionally, iron limitation in high nutrient-low chlorophyll regions increases cell carbon:chlorophyll ratios [*Behrenfeld et al.*, 2009; *Westberry et al.*, 2016] but is not accounted for in the CbPM, which could also bias PP estimates in the transition zone and subarctic regions throughout the year. At ALOHA, where the mixed layer is shallower than the euphotic depth year-round and phytoplankton are not iron-limited, the CbPM matches geochemical PP estimates.

CESM, though more mechanistically sophisticated than either the VGPM or CbPM, also underestimates PP as compared to geochemical estimates throughout the subarctic and transition zone in all seasons except summer. This may be a result of model physics, which underestimates maximum annual mixed layer depths in the northwest Pacific and, in turn, underestimates surface nutrient concentrations throughout the subarctic [*Moore et al.*, 2013], which could suppress PP. Further analysis of model output that separates physical and ecological impacts on PP would help understand the discrepancies with geochemical-based PP estimates.

3.4.2 *Export production and efficiency*

Previous analysis at OSP and ALOHA found that annual EP from the CbPM PP + Laws00 e-ratio algorithms matched geochemically-determined annual EP in both the subtropics and subarctic [*Emerson*, 2014]. However, neither the CbPM PP nor the Laws00 e-ratio algorithms match geochemical estimates in the transition zone and subarctic North Pacific, such that annual EP agreement at OSP is the fortuitous result of offsetting biases in the PP and e-ratio algorithms. No single e-ratio algorithm matches geochemical e-ratio estimates throughout the North Pacific, with the Dunne07 algorithm best fitting geochemical estimates at OSP and in the container ship regions while the Laws00 algorithm best fits geochemical estimates at ALOHA.

These algorithms represent e-ratio variations based only on SST, chlorophyll and PP and therefore may not be applicable in locations or seasons where few or no calibration data were available. A potential benefit of CESM is that it employs a mechanistic ecosystem model to determine the fraction of PP that is recycled versus exported. However the seasonality and magnitude of CESM e-ratios does not match geochemical estimates. Recent development of a mechanistic ecosystem-based e-ratio model using satellite products provides a promising step forward [*Siegel et al.*, 2014], although further work is needed to validate and expand upon such approaches [e.g. *Stukel et al.*, 2015; *Siegel et al.*, 2016], particularly in high latitude regions in fall and winter where observational data is lacking.

Satellite-based estimates of annual EP face the additional challenge that existing e-ratio algorithms are based on single time point estimates of EP/PP, and therefore cannot account for effects of seasonal physical dynamics on the annual e-ratio. Geochemical-based estimates of annual EP demonstrate that 40-90% of seasonally-exported organic carbon is ventilated during deep winter mixing in the Kuroshio and Western regions of the North Pacific [*Palevsky et al.,* 2016] yielding significantly lower estimates for EP determined to the winter ventilation depth than the seasonally-varying mixed layer depth (Figure 3.4). Satellite-based e-ratio models cannot account for wintertime ventilation or net heterotrophy, both of which reduce annual EP. In order to quantify the influence of EP on the global carbon cycle, annual EP rates need to account for these wintertime processes to avoid overestimating carbon sequestration. New process-based e-ratio models should be developed to account for these processes and existing e-ratio algorithms should be evaluated with this context in mind.

Global biogeochemical models explicitly resolve depth-dependent production, remineralization, and ventilation. CESM shows significantly reduced EP (30-40%) to the winter

mixed layer depth as compared to the base of the seasonally-varying mixed layer in the Kuroshio and Western regions (Figure 3.4), with the fraction of seasonally-exported material ventilated comparable to geochemical estimates in the Western region but lower in the Kuroshio. Importantly, both the geochemical observations and CESM output demonstrate that annual EP and e-ratio to the winter ventilation depth (i.e., export that sequesters carbon from the atmosphere) are substantially lower than EP and e-ratio integrated to the seasonally-varying mixed layer depth in regions with deep winter mixing. These results emphasize the role that physics play in the ocean's biological pump. Furthermore, the ability of CESM to capture winter ventilation effects on EP is promising for our ability to model the ocean's biological pump over annual and longer time scales.

3.5 CONCLUSIONS

This study represents a rare opportunity to compare geochemical, satellite and global biogeochemical model estimates of PP, e-ratio and EP across broad spatial scales throughout the annual cycle. The results demonstrate that no combination of the two satellite PP algorithms and three e-ratio algorithms nor CESM can reproduce geochemical observation-based estimates of PP, EP and e-ratio at the ALOHA and OSP time-series stations and across the North Pacific basin. These results emphasize that caution is needed in applying ecosystem models or satellite-based algorithms for global-scale analysis of the ocean's biological pump since no single approach accurately represents spatial and temporal trends in productivity across multiple biogeochemically and ecologically distinct regions. Caution is especially warranted in the strongly seasonal and more physically dynamic high latitude ocean, which is less well validated than the subtropics in model and algorithm development and likely undersampled from late fall

through early spring. Both geochemical- and model-based estimates of export highlight the importance of deep winter mixing at high latitudes in significantly reducing annual export rates. Additional observational data, especially from high latitude regions and during seasons with deep mixed layers that may confound models designed for stratified conditions, are needed to better calibrate model and satellite-based estimates of export and improve their skill in estimating the current magnitude and predicting future changes in the global ocean's biological pump.

3.6 FIGURES AND TABLES

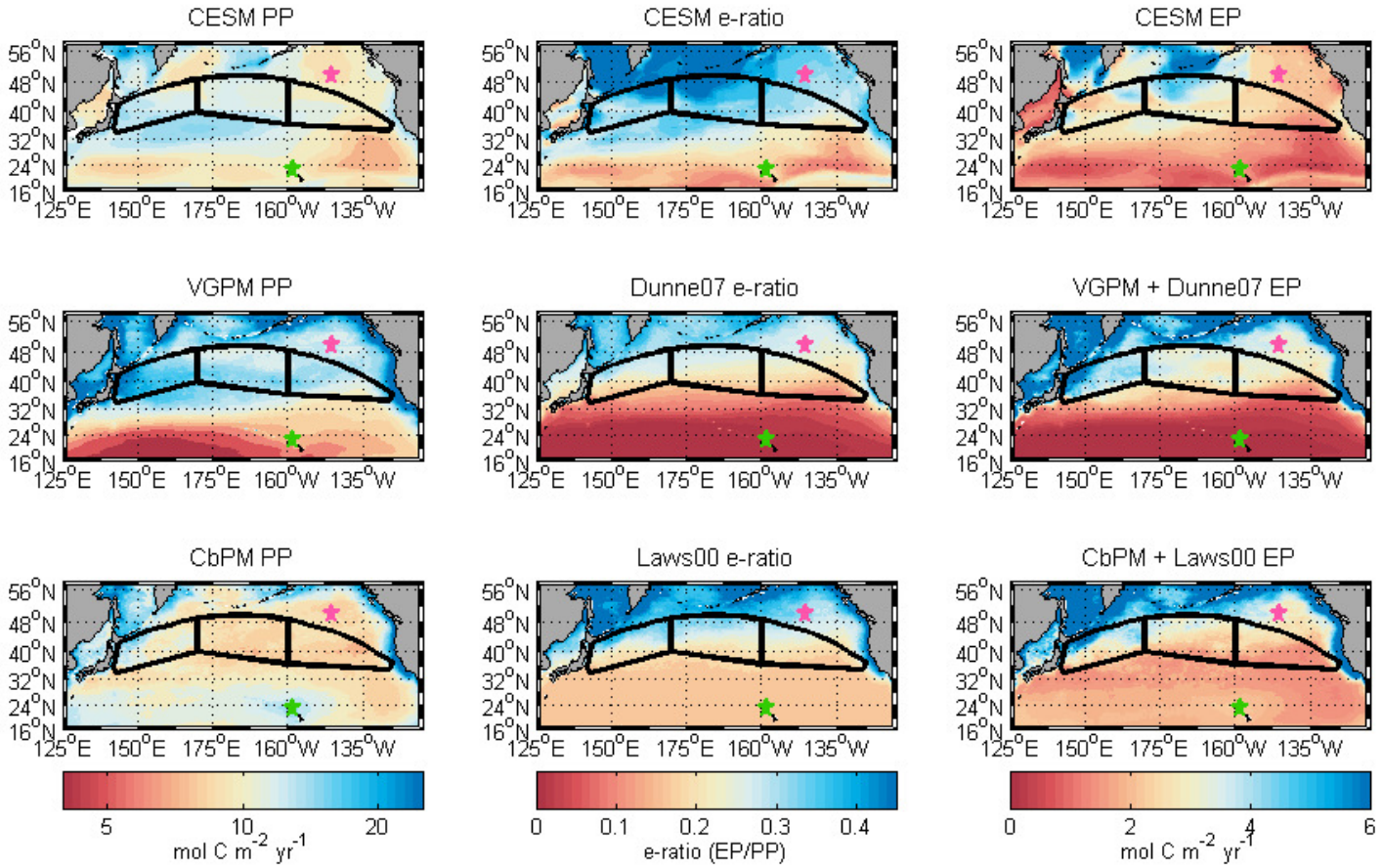

Figure 3.1. Annual primary production (PP, left), export efficiency (e-ratio, EP/PP, middle), and export production (EP, right) for the North Pacific as predicted by CESM (top), and satellite-based algorithms using MODIS data from 2003-2013 (middle and bottom). OSP (pink star), ALOHA (green star) and container ship regions (outlined in black; referred to from west to east as the Kuroshio, Western and Eastern regions respectively) are shown in all plots.

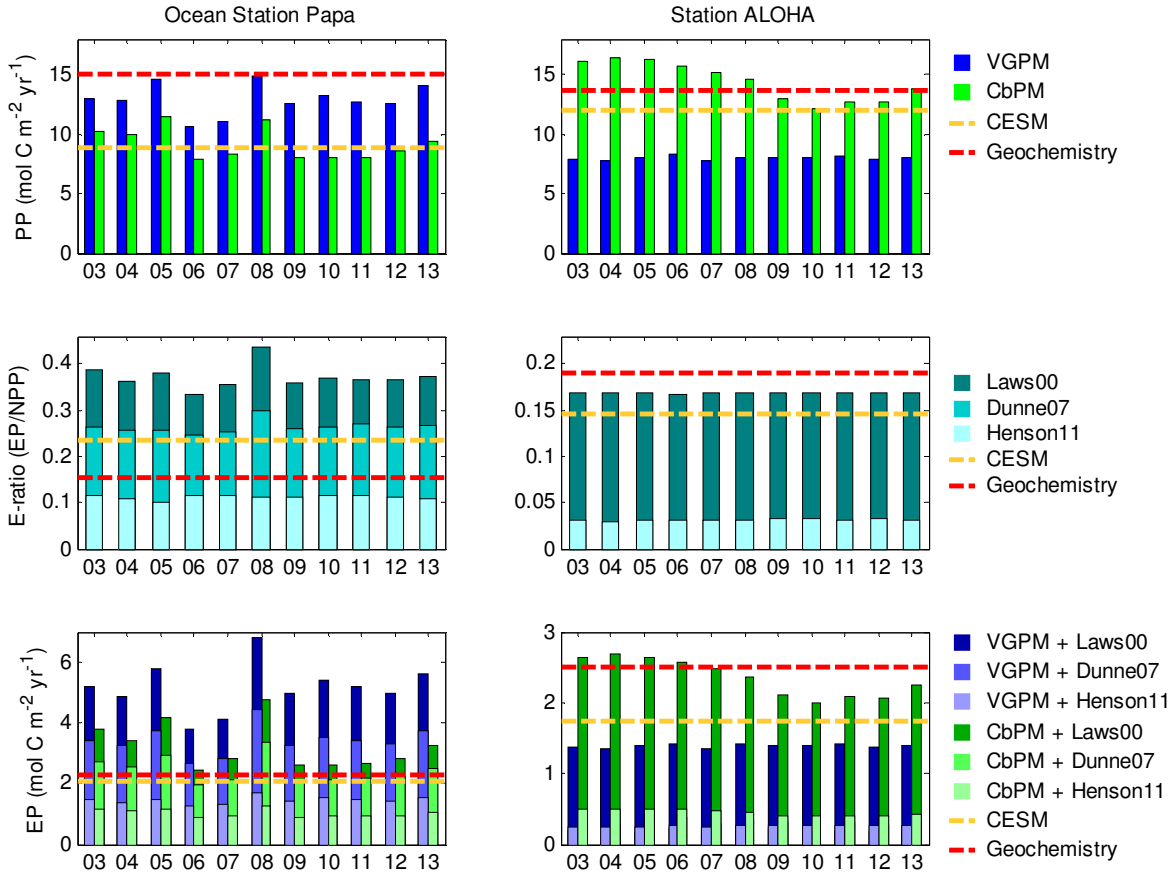

Figure 3.2. Annual primary production (PP, top), export efficiency (e-ratio, EP/PP, middle), and export production (EP, bottom) at OSP and ALOHA. Satellite-based estimates are shown for all years 2003-2013. CESM and geochemistry results represent a single climatological year.

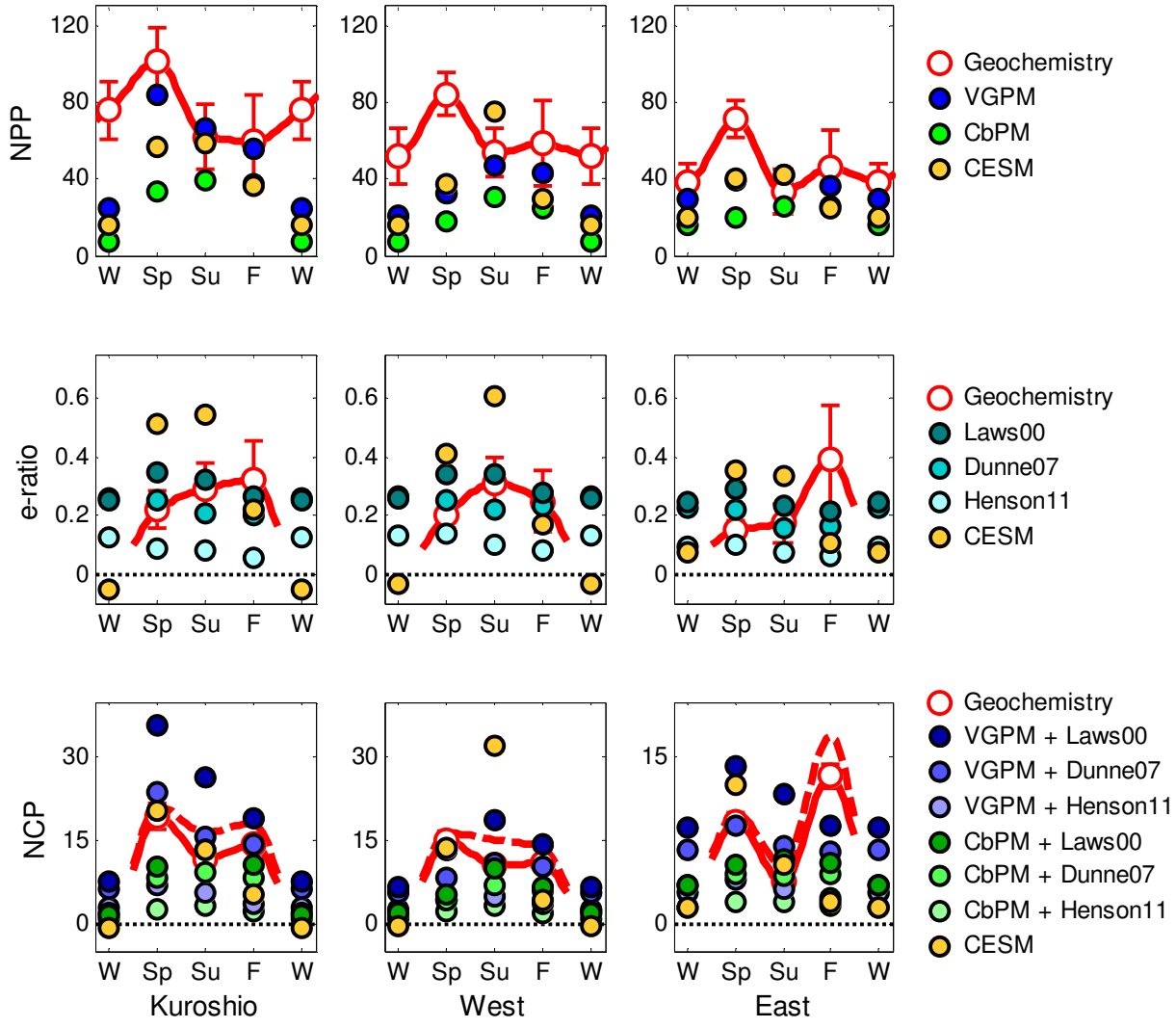

Figure 3.3. Seasonal primary production (PP, top), export efficiency (e-ratio, middle), and export production (EP, bottom) for each container ship region. For EP, dashed red lines indicate geochemical EP extended to the compensation depth. Note the 2× change in y-axis scale for EP in the East.

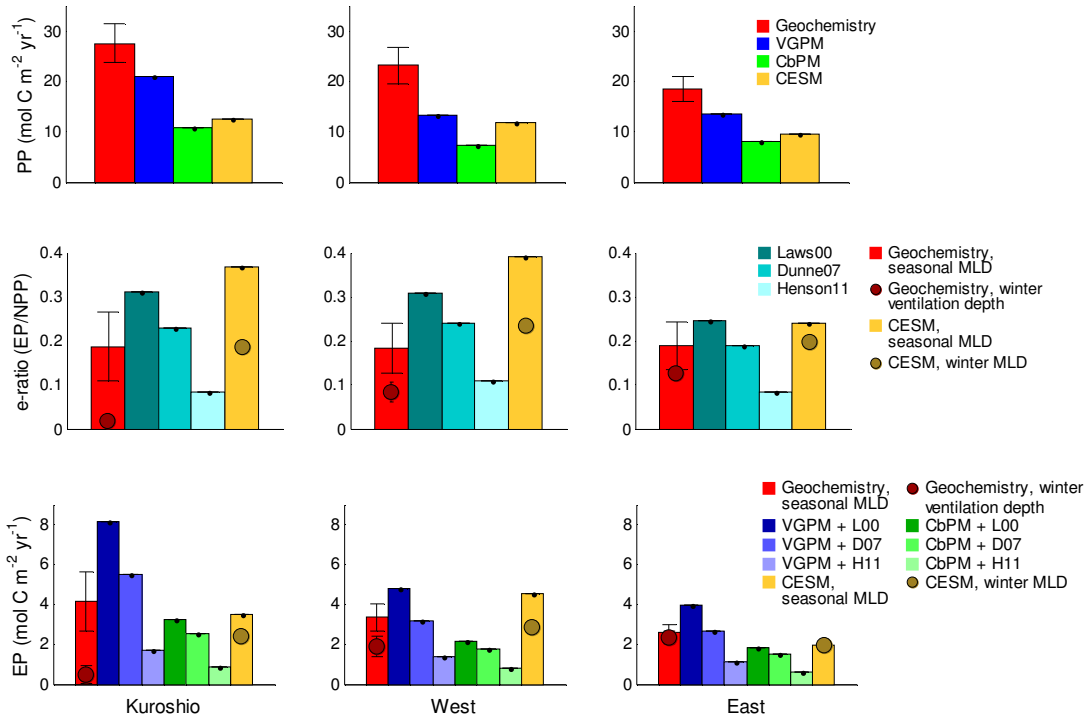

Figure 3.4. Annual primary production (PP, top), e-ratio (EP/NPP), and export production (EP, bottom) for each container ship region. For e-ratio and EP, geochemical and CESM estimates are presented both to the seasonally-varying mixed layer depth (bars) and the winter ventilation depth (colored circles).

Table 3.1: PP, EP and e-ratio data sources.

	Primary production (PP)	**e-ratio (EP/PP)**	**Export production (EP)**
Geochemistry: Time-series sites	^{14}C-PP incubations[a]	Determined from EP and PP	Oxygen, carbon and nitrate annual mass balance (*Emerson* [2014], Table 2)
Geochemistry: Container ship regions	Triple oxygen isotope budgets[b]	Determined from EP and PP	O_2/Ar dissolved gas ratio budgets[b]
Satellite-based algorithms	VGPM [*Behrenfeld and Falkowski*, 1997] and CbPM [*Westberry et al.*, 2008][c]	*Laws et al.* [2000]; *Dunne et al.* [2005, 2007]; and *Henson et al.* [2011][c]	Determined from all combinations of satellite-based PP and e-ratio algorithms
Global biogeochemical model	CESM1-BEC climatological year[d]	CESM1-BEC climatological year[d]	CESM1-BEC climatological year[d]

[a] Ocean Station Papa data are from 24-hour incubations (compiled in *Palevsky et al.* [2016], Table 3). Station ALOHA data are from 12-hour dawn to dusk incubations on monthly Hawaii Ocean Time-series (HOT) cruises from 2003-2013 (available from http://hahana.soest.hawaii.edu/hot/hot-dogs) integrated to 125 meters following the trapezoid method and scaled to a 24-hour incubation equivalent NPP rate assuming a 15% respiration rate from dusk to dawn [*Karl et al.*, 1996].

[b] Gross oxygen production (GOP) to the base of the seasonal mixed layer and the euphotic zone and EP to the base of the seasonal mixed layer, compensation depth, and winter ventilation depth calculated based on mixed layer geochemical measurements on 16 container ship cruises [*Palevsky et al.*, 2016]. GOP is converted to PP using a GOP:NPP ratio of 2.7 [*Marra*, 2002]. EP is converted from oxygen to carbon units using an O_2:C ratio of 1.4 [*Laws*, 1991]. Uncertainty in these estimates represents methodological uncertainty, but not sampling bias within the regions, since satellite and CESM data are sampled at the same times and locations as geochemical measurements (see *Palevsky et al.*, [2016] for details). Seasonal EP is not presented for the winter due to high uncertainty.

[c] Moderate Resolution Imaging Spectroradiometer (MODIS) Aqua R2014 monthly satellite products at 1/6° resolution (available from http://www.science.oregonstate.edu/ocean.productivity) were downloaded directly for the VGPM and CbPM and used in combination with SST and chlorophyll to calculate e-ratios following the Laws00, Dunne07 and Henson11 algorithms. The Dunne07 algorithm is undefined for conditions at Station ALOHA, and is therefore not presented. For a small fraction of years in the MODIS record (2-3), satellite data were unavailable for December at OSP for some variables. Annual records for those years were created using climatological mean December data for all years with available data.

[d] Global output from the Parallel Ocean Program of the Community Earth System Model version 1.1.1 (CESM), with the Biogeochemical Ecosystem Component (BEC), run with repeated climatological normal year forcing. Full details of the model configuration are described in *Nicholson et al.* [2014]. Model rates of photosynthesis and respiration in each depth level in each grid cell were used to determine PP both in the mixed layer and throughout the full euphotic zone and EP to the base of the seasonal mixed layer, the community compensation depth, and the winter mixed layer.

Chapter 4.

Influence of biological carbon export on ocean carbon uptake over the annual cycle across the North Pacific Ocean

4.1 INTRODUCTION

The ocean currently absorbs 26% of all anthropogenic carbon emissions [*Le Quéré et al.*, 2015], slowing global climate change by reducing carbon accumulation in the atmosphere and modifying marine chemistry by redistributing this carbon into the ocean. Much attention has thus been focused on understanding the mechanisms controlling the rates and spatial patterns of ocean carbon uptake [e.g. *Takahashi et al.*, 2002, 2009; *Wanninkhof et al.*, 2013; *Landschützer et al.*, 2014]. There are three main mechanisms that drive exchange of CO_2 between the ocean and the atmosphere: chemical effects due to temperature- and salinity-dependent variation in the solubility of CO_2 in seawater; biological effects due to fixation and export of organic carbon from the surface ocean as net community production (NCP) and to production of biogenic $CaCO_3$; and physical effects due to advection and mixing, which can sequester carbon from the atmosphere by transporting CO_2 absorbed at the surface into the deep ocean. Understanding the relative roles of these chemical, physical, and biological processes is necessary to improve our ability to mechanistically predict how the ocean carbon sink will respond to and exert a feedback influence on increasing atmospheric CO_2 concentrations and climate changes projected for the 21st century [e.g. *Roy et al.*, 2011; *Ciais et al.*, 2013; *Hauck et al.*, 2015].

The North Pacific is a major sink for atmospheric CO_2, featuring a band of strong CO_2 uptake at the transition zone between the subarctic gyre to the north and the subtropical gyre to

the south (*Takahashi et al.*, [2009]; Figure 4.1). Previous studies have used a variety of observational and analytical approaches to quantify the contributions of temperature-driven solubility effects, physical circulation and biological carbon export to the North Pacific carbon sink. *Takahashi et al.* [2002] presented a simple approach to separate temperature and non-temperature effects on observed seasonal cycles of surface ocean partial pressure of CO_2 (pCO_2). Applying this approach to both observations and global biogeochemical model output reveals opposite-phase temperate- and non-temperature-driven seasonal cycles where temperature effects dominate in the subtropical and much of the eastern subarctic North Pacific and non-temperature effects of biological pCO_2 drawdown and physical pCO_2 supply dominate in the high latitude and western subarctic North Pacific, with a region of more complex balance between the two at the interface between these two regimes [*Takahashi et al.*, 2002; *Chierici et al.*, 2006; *McKinley et al.*, 2006]. Recent work explicitly separating non-temperature effects into physical and biological components concluded that despite their large effect on the seasonal cycle, temperature-driven changes in solubility contribute only a small portion of annual CO_2 uptake, with geostrophic advection joining biological carbon export as the dominant drivers of strong CO_2 uptake and setting the location of the strong transition zone CO_2 sink [*Ayers and Lozier*, 2012].

Opportunities to evaluate seasonal and annual effects on the ocean carbon sink over a basin-wide scale using direct measurements of both carbonate chemistry and biological carbon export rates are rare. Global biogeochemical models can simulate both physical and biological effects on the carbonate chemistry system, but analysis of model output in the North Pacific has demonstrated that the models have difficulty resolving the effects of both physical and biological processes on pCO_2, especially in the highly dynamic western regions [*McKinley et al.*, 2006].

Previous observation-based basin-scale analyses have combined carbonate chemistry measurements from repeat ship of opportunity transects with estimates of biological carbon export based on seasonal nitrate drawdown [*Wong et al.*, 2002a; *Chierici et al.*, 2006] or used climatological carbonate chemistry data and estimated biological carbon export from satellite-based primary production and export efficiency algorithms [*Ayers and Lozier*, 2012]. These approaches are limited, however, by discrepancies between satellite- and geochemical observation-based estimates of seasonal biological carbon export [*Palevsky et al.*, submitted manuscript] and the inability of either satellite-based estimates or measurements of nitrate drawdown to account for the fraction of seasonally-exported organic matter that is subsequently ventilated back to the atmosphere as CO_2 during deep winter mixing, which has a strong influence on annual biological carbon export in the western North Pacific [*Palevsky et al.*, 2016].

In this study, we use measurements of the complete carbonate chemistry system on fifteen basin-wide transects across the North Pacific on ships of opportunity to quantify the rate and the physical, chemical, and biological drivers of air-sea CO_2 flux across the entire North Pacific throughout the full annual cycle. Seasonal and annual rates of biological carbon export (defined as net community production, or NCP) have recently been determined based on measurements of dissolved O_2/Ar gas ratios measured on the same set of ship of opportunity transects [*Palevsky et al.*, 2016]. The combination of measured carbonate chemistry with O_2/Ar-based estimates of NCP on a basin-wide scale throughout the full annual cycle provides a unique opportunity to resolve the role of biological carbon export in driving the North Pacific ocean carbon sink.

4.2 REGIONAL SETTING

Carbonate chemistry data presented here are interpreted in the context of three broad regions across the North Pacific, as defined by *Palevsky et al.* [2016]: the Kuroshio, west of 170°E, influenced by the Kuroshio, Oyashio, and Kuroshio Extension currents; the Western region, between 170°E and 160°W; and the Eastern region, east of 160°W (Figure 4.1). These regions include portions of both the physical transition zone between the subarctic and subtropics between 32°N and 42°N [*Roden*, 1991] and the high-nutrient low-chlorophyll subarctic gyre to the north [*Harrison et al.*, 2004a]. Superimposed on these physical gradients, the transition zone chlorophyll front migrates seasonally across the region, with its southernmost extent in February largely south of our three study regions, while its northernmost extent in August at ~40°N lies in the middle of our regions [*Polovina et al.*, 2001; *Ayers and Lozier*, 2010].

Our regional division scheme focuses on analysis of east-west basin-wide trends. The western basin is more dynamically complex, influenced both by strong eastward geostrophic transport by the Kuroshio Extension and by deep winter mixing (< 200 m) [*Jayne et al.*, 2009; *Ohno et al.*, 2009]. The eastern side of the basin experiences weaker geostrophic transport and has a strong permanent halocline at ~120 m that limits the extent of winter mixing [*Harrison et al.*, 1999]. Primary production rates, as determined by analysis of triple oxygen isotope samples collected along the same container ship transects described in this study, are greatest in the Kuroshio and decrease eastward across the basin, likely due both to greater nutrient supply from deeper winter mixing and greater aeolian dust (iron) supply in the west [*Palevsky et al.*, 2016]. Analysis of dissolved O_2/Ar gas ratios measured on the same samples indicate that spring through fall NCP rates are also greatest in the Kuroshio and decrease eastward across the basin. However, wintertime O_2/Ar measurements indicate that much of the seasonally-exported organic

material is subsequently remineralized and is ventilated back to the atmosphere during winter mixing. Winter mixed layer depths and thus the fraction of seasonally-exported material that is ventilated to the atmosphere as CO_2 increase westward across the basin, such that annual NCP rates integrated to the winter ventilation depth are greatest in the east and decrease westward across the basin, yielding the opposite trend to productive season export [*Palevsky et al.*, 2016].

4.3 METHODS

4.3.1 *Sample collection and measurement*

Samples for carbonate chemistry analysis were collected from shipboard seawater intake (10 m depth) on fifteen basin-wide transects of the North Pacific between Hong Kong and Long Beach, California onboard the M/V OOCL Tianjin and the M/V OOCL Tokyo between October 2008 and December 2012 (Figure 4.1, Figure 4.S1). Sea surface temperature (SST) and salinity (S) at the time of sample collection were determined using a Sea-Bird Electronics SBE45 thermosalinograph installed in the ship's seawater intake. Carbonate chemistry sampling locations largely correspond with locations of sample collection for analysis of dissolved O_2/Ar ratios as a tracer of net community production (NCP), as presented by *Palevsky et al.* [2016], allowing us to interpret carbonate chemistry data alongside NCP results.

Samples for dissolved inorganic carbon (DIC) analysis were collected on all cruises into 250 mL bottles with greased ground glass stoppers and poisoned with 100 μL of saturated mercuric chloride solution. DIC concentrations were determined in the laboratory through a combination of manometric measurements (*Quay and Stutsman*, 2003; n = 320) and measurements with an Apollo SciTech AS-C3 IR-based DIC analyzer (n = 138). Certified reference materials (Andrew Dickson, UCSD) were used for calibration and determination of

sample-specific measurement error for all DIC measurements using the AS-C3 analyzer, with mean uncertainty of ± 4 μmol kg^{-1}. Comparison of duplicate samples analyzed both manometrically and with the AS-C3 analyzer (n = 111) agree to within 1 ± 9 μmol kg^{-1} and indicate uncertainty of ± 8 μmol kg^{-1} in the manometric measurements.

A second carbonate chemistry parameter was determined for all locations with DIC measurements. For transects from 2008-2010, pCO_2 was measured using an automated underway IR-detection-based system, which determines seawater pCO_2 to ± 2 μatm (*Feely et al.*, 1998; *Pierrot et al.*, 2009; data available online at http://www.pmel.noaa.gov/co2/story/Long+Beach+to+Hong+Kong). Measurements from this system were made continuously along the cruise tracks and were extracted at locations corresponding to DIC sample collection. For transects in 2011-2012, the underway pCO_2 system was not used and instead discrete samples were collected to determine total alkalinity (TA) at DIC sampling locations, following the same collection procedures as for DIC. TA samples were measured using an automated, open-cell potentiometric titration system (*Dickson et al.*, [2007]; SOP 3b), with sample-specific measurement error quantified based on certified reference materials (Andrew Dickson, UCSD) measured with each sample batch (mean uncertainty of ± 2 μeq kg^{-1}). For a small fraction of DIC sampling locations (n = 51), neither underway pCO_2 nor discrete measurements of TA were available due to issues with the underway pCO_2 system or lost samples during TA analysis. For these sampling locations, TA was determined using regional TA-salinity relationships determined from the measured TA samples (Figure 4.S2).

For all locations, the combination of DIC with either TA or pCO_2 fully constrains the carbonate chemistry system. The parameter not measured (either TA or pCO_2) was calculated for each sampling location using the program CO2sys [*van Heuven et al.*, 2011] with the carbonate

constants of *Mehrbach et al.* [1973] refit by *Dickson and Millero* [1987]. These constants are also used in all carbonate chemistry calculations throughout this work. Uncertainty in each calculated carbonate chemistry parameter was determined using a Monte Carlo approach, where 3000 calculations were made with CO2sys while allowing the two carbonate chemistry input parameters to vary according to sample-specific measurement uncertainty. Mean uncertainty in TA calculated from DIC and pCO_2 is ± 9 μeq kg^{-1} and mean uncertainty in pCO_2 calculated from DIC and TA is ± 16 μatm. Seasonal mean DIC, TA and pCO_2 were calculated for each region, with methodological uncertainty (1σ) determined using a Monte Carlo 3000-simulation analysis where each individual sampling location value varied according to sample-specific measurement uncertainty.

4.3.2 *Processes influencing DIC and pCO_2*

Seasonal changes in observed DIC concentrations in the surface mixed layer (mmol m^{-3} d^{-1}) are influenced by air-sea CO_2 flux (Gas), biological export of organic carbon (net community production, or NCP), biological production of calcium carbonate ($CaCO_3$), and physical addition or removal of DIC due to advection and mixing (Physics).

$$\frac{\partial \mathrm{DIC}}{\partial t} = \left.\frac{\partial \mathrm{DIC}}{\partial t}\right|_{\mathrm{Gas}} + \left.\frac{\partial \mathrm{DIC}}{\partial t}\right|_{\mathrm{NCP}} + \left.\frac{\partial \mathrm{DIC}}{\partial t}\right|_{\mathrm{CaCO_3}} + \left.\frac{\partial \mathrm{DIC}}{\partial t}\right|_{\mathrm{Physics}} \quad (1)$$

Each term in equation (1) is calculated seasonally for each of the three regions shown in Figure 4.1. Seasonal fluxes for the Gas, NCP, and $CaCO_3$ terms (mmol m^{-2} d^{-1}; details of flux estimation methods for each term given below) are converted to influences on the seasonal DIC concentration (μmol kg^{-1} d^{-1}) by multiplying by the regional mean $\frac{\rho}{\mathrm{MLD}}$ in each season, where ρ is the temperature- and salinity-dependent seawater density and MLD is the mixed layer depth, as determined by 0.125 kg m^{-3} density increase from the surface [*Monterey and Levitus*, 1997] in

World Ocean Atlas 2013 (WOA; https://www.nodc.noaa.gov/OC5/woa13) gridded temperature and salinity fields. Uncertainty in MLD estimates is calculated as the standard error $\left(\frac{2\sigma}{\sqrt{n}}\right)$ of the mean for each season in each region. The physical influence of advection and mixing is calculated as the residual based on estimates of all other terms in equation (1).

Seasonal changes in observed pCO_2 in the surface mixed layer are influenced by all factors that influence DIC, as well as effects of temperature and salinity on the solubility of CO_2.

$$\frac{\partial \mathrm{pCO_2}}{\partial t} = \frac{\partial \mathrm{pCO_2}}{\partial t}\Big|_{\mathrm{Temp}} + \frac{\partial \mathrm{pCO_2}}{\partial t}\Big|_{\mathrm{Sal}} + \frac{\partial \mathrm{pCO_2}}{\partial t}\Big|_{\mathrm{Gas}} + \frac{\partial \mathrm{pCO_2}}{\partial t}\Big|_{\mathrm{NCP}} + \frac{\partial \mathrm{pCO_2}}{\partial t}\Big|_{\mathrm{CaCO_3}} + \frac{\partial \mathrm{pCO_2}}{\partial t}\Big|_{\mathrm{Physics}} \quad (2)$$

The individual right hand side (RHS) terms can each be calculated following equations 3-7:

$$\frac{\partial \mathrm{pCO_2}}{\partial t}\Big|_{\mathrm{Temp}} = \left(\frac{\partial \mathrm{SST}}{\partial \mathrm{t}}\right) * \mathrm{pCO_2}(0.0423\ ^{\circ}\mathrm{C}^{-1}) \quad (3)$$

$$\frac{\partial \mathrm{pCO_2}}{\partial t}\Big|_{\mathrm{Sal}} = \left(\frac{\partial \mathrm{S}}{\partial \mathrm{t}}\right) * \frac{\mathrm{pCO_2}}{\mathrm{S}}(1.6) \quad (4)$$

$$\frac{\partial \mathrm{pCO_2}}{\partial t}\Big|_{\mathrm{Gas}} = \left(\frac{\partial \mathrm{DIC}}{\partial t}\Big|_{\mathrm{Gas}}\right)\left(\frac{\partial \mathrm{pCO_2}}{\partial \mathrm{DIC}}\right) \quad (5)$$

$$\frac{\partial \mathrm{pCO_2}}{\partial t}\Big|_{\mathrm{NCP}} = \left(\frac{\partial \mathrm{DIC}}{\partial t}\Big|_{\mathrm{NCP}}\right)\left[\left(\frac{\partial \mathrm{pCO_2}}{\partial \mathrm{DIC}}\right) - \frac{17}{117}\left(\frac{\partial \mathrm{pCO_2}}{\partial \mathrm{TA}}\right)\right] \quad (6)$$

$$\frac{\partial \mathrm{pCO_2}}{\partial t}\Big|_{\mathrm{CaCO_3}} = \left(\frac{\partial \mathrm{DIC}}{\partial t}\Big|_{\mathrm{CaCO_3}}\right)\left[\left(\frac{\partial \mathrm{pCO_2}}{\partial \mathrm{DIC}}\right) + 2\left(\frac{\partial \mathrm{pCO_2}}{\partial \mathrm{TA}}\right)\right] \quad (7)$$

The temperature- and salinity- dependences of CO_2 in equations (3) and (4) are from *Takahashi et al.* [1993] and *Sarmiento and Gruber* [2006] respectively. The air-sea CO_2 flux (Gas), NCP and $CaCO_3$ dependencies in equations 5-7 represent changes to DIC and TA concentrations in the surface mixed layer, which in turn affect pCO_2. The influence of TA changes on pCO_2 are given based on the known stoichiometric relationships between DIC and TA changes for each process, where gas exchange does not affect TA, NCP increases TA by 17 moles for each 117 moles of DIC fixed to organic carbon [*Anderson and Sarmiento*, 1994], and $CaCO_3$ production decreases TA by 2 moles for each mole $CaCO_3$ produced due to removal of the doubly charged

CO_3^{2-} ion. Sensitivity of pCO_2 to DIC and TA changes in equations 5-7, based on the Revelle and Alkalinity factors, is given by equations 8 and 9 respectively:

$$\frac{\partial pCO_2}{\partial DIC} = \frac{\text{Revelle Factor} * pCO_2}{DIC} \quad (8)$$

$$\frac{\partial pCO_2}{\partial TA} = \frac{\text{Alkalinity Factor} * pCO_2}{TA} \quad (9)$$

Seasonal mean values for each region are calculated for each individual term in equations 3-9 from the compilation of all discrete sample measurements. As for DIC, the physical influence of advection and mixing is calculated as the residual based on estimates of all other terms in equation (2).

4.3.2.1 Time rate of change

To determine the DIC and pCO_2 time rate of change tendencies in equations (1) and (2) as well as the SST and salinity time rate of change tendencies in equations (3) and (4), all surface mixed layer measurements for each region are compiled into a single composite year, with the seasonal cycle determined by fitting simple harmonic functions using a least-squares approach. The derivatives of these harmonic fits for the day of the year corresponding to collection of each discrete sample are compiled and used to calculate the seasonal mean time rate of change tendency of mixed layer DIC, pCO_2, SST and S in each season for each of the three regions. Methodological uncertainty in the time rate of change of DIC and pCO_2 is calculated following a Monte Carlo approach based on 3000 iterations computing harmonic fits to the composite annual data while allowing each individual sampling location value to vary according to sample-specific measurement uncertainty.

4.3.2.2 Air-sea CO_2 flux

The rate of air-sea CO_2 gas flux is calculated from the difference in pCO_2 between the atmosphere and the surface ocean as:

$$\left.\frac{\partial \mathrm{DIC}}{\partial t}\right|_{\mathrm{Gas}} = \mathrm{k}_{\mathrm{CO}_2} * \mathrm{K}_0 * \left(\mathrm{pCO}_{2,\mathrm{atmos}} - \mathrm{pCO}_{2,\mathrm{ocean}}\right) * \rho \quad (10)$$

where $\mathrm{k}_{\mathrm{CO}_2}$ (m d^{-1}) is the air-sea gas transfer velocity for CO_2, K_0 (mol kg^{-1} μatm^{-1}) is the temperature- and salinity-dependent solubility of CO_2 [*Weiss*, 1974], and ρ is the seawater density (kg m^{-3}). When atmospheric pCO_2 exceeds (is less than) surface ocean pCO_2, gas exchange causes the value of $\left.\frac{\partial \mathrm{DIC}}{\partial t}\right|_{\mathrm{Gas}}$ to be positive (negative). Air-sea CO_2 flux rates are calculated for each individual discrete sample, and then compiled to calculate mean values in each season for each of the three regions.

The value of $\mathrm{pCO}_{2,\mathrm{atmos}}$ was determined for the time and location of each discrete sample measurement of $\mathrm{pCO}_{2,\mathrm{ocean}}$ using NOAA Earth Systems Research Laboratory CarbonTracker (CT2015; http://www.esrl.noaa.gov/gmd/ccgg/carbontracker) atmospheric CO_2 mole fraction data on a global 3° × 2° grid, averaged daily over the lowest two atmospheric pressure levels, and converted to a partial pressure of CO_2 using NCEP/NCAR reanalysis daily average atmospheric surface pressure (http://www.esrl.noaa.gov/psd/data/gridded/data.ncep.reanalysis.html), with an estimated uncertainty of ± 2 μatm. Daily wind speed data from the NOAA National Climactic Data Center's multiple-satellite Blended Sea Winds product (https://www.ncdc.noaa.gov/oa/rsad/air-sea/seawinds.html) were used to calculate $\mathrm{k}_{\mathrm{CO}_2}$ for the time and location of each discrete sample following the *Nightingale et al.* [2000] relationship between $\mathrm{k}_{\mathrm{CO}_2}$ and wind speed and the *Reuer et al.* [2007] weighting scheme. Uncertainty in the air-sea gas exchange rate is estimated by assuming that the majority of uncertainty results from the parameterized relationship between

gas exchange rate (k_{CO_2}) and wind speed, and that the spread between the air-sea gas exchange rates calculated from the *Liss and Merlivat* [1986] and *Wanninkhof* [1992] equations represents 95% of the variability (±2σ) in k_{CO_2} [*Palevsky et al.*, 2013], yielding a mean uncertainty in k_{CO_2} of ±14% over all discrete sample locations in the data set. Total methodological uncertainty in seasonal and annual mean air-sea CO_2 flux in each region is determined with a Monte Carlo analysis including measurement uncertainty in atmospheric pCO_2, sample-specific uncertainty in seawater pCO_2 and uncertainty from estimation of the air-sea gas transfer rate.

4.3.2.3 Net community production and $CaCO_3$ production

Biological processes influence DIC and pCO_2 through export of biologically-fixed organic carbon (NCP) and inorganic calcium carbonate ($CaCO_3$). NCP for each of the three sampling regions has previously been determined based on measurements of dissolved O_2/Ar gas ratios made on the same transects as carbonate chemistry measurements analyzed here (full details are in *Palevsky et al.* [2016]). O_2/Ar samples for the NCP analysis were measured at most stations with carbonate chemistry measurements included in the analysis in this paper (88%), as well as at a number of additional locations (n = 271) along the same transects where carbonate chemistry measurements are not available. We use NCP rates determined at all sampling locations with O_2/Ar because NCP rates determined only from the locations with carbonate chemistry samples differ minimally from those calculated from the full data set over the spring through fall productive season.

Rates of $CaCO_3$ production are based on published estimates of the particulate inorganic carbon (PIC): particulate organic carbon (POC) ratio and O_2/Ar-based regional estimates of NCP. We assume PIC:POC ratios of 0.1, 0.2 and 0.3 for the Kuroshio, Western and Eastern regions respectively. PIC:POC for the Kuroshio region is based on recent observational estimates

at the Kuroshio Extension Observatory [*Fassbender*, 2014], which also match estimates of the global mean PIC:POC ratio [*Jin et al.*, 2006] and are consistent with previous regional analysis indicating low calcification rates in the western North Pacific [*Wong et al.*, 2002a]. Observational estimates in the eastern subarctic North Pacific have found PIC:POC ratios above the global mean, with the mean value of 0.3 for the Eastern region taken from multiple observation-based estimates at Ocean Station Papa [*Fassbender et al.*, 2016]. We assume an intermediate value for the Western region (0.2), where region-specific observational estimates are lacking. Multiplying these PIC:POC ratios by O_2/Ar-based seasonal NCP rates in each region yields estimated rates of $CaCO_3$ production of 0.4, 0.7, and 0.9 mol m^{-2} yr^{-1} in the Kuroshio, Western, and Eastern regions respectively. This approach implicitly assumes that all NCP is exported as POC rather than as dissolved organic carbon which likely overestimates $CaCO_3$ export, but the uncertainty in this assumption is less than that in the PIC:POC values. We assume 100% uncertainty in estimated seasonal $CaCO_3$ production rates for all regions.

4.3.3 *Uncertainty analysis*

We quantify uncertainty in each term in equations (1) and (2) resulting from both methodological error and undersampling bias. Methodological uncertainty in seasonal and regional mean carbonate chemistry, the time rate of change terms, and air-sea CO_2 flux rates are described above. Sampling bias is calculated based on comparison between regional mean satellite-based SST and chlorophyll concentrations for each season determined only from the times and cruise track locations where discrete samples were collected and those determined using all grid points within each region sampled continuously from 2008-2012 (Moderate Resolution Imaging Spectroradiometer 1/6° × 1/6° monthly data provided by the Oregon State Ocean Productivity group, http://www.science.oregonstate.edu/ocean.productivity). This is the

approach used previously by *Palevsky et al.* [2016] to determine sampling bias in NCP estimates. Sampling biases for the set of sampling locations with carbonate chemistry data used in this analysis are similar to those found in the O_2/Ar discrete sampling dataset evaluated by *Palevsky et al.* [2016] (Figure 4.S3). Undersampling bias in our estimates of air-sea CO_2 flux and in the time rate of change of both DIC and pCO_2 is calculated as the mean percent difference between satellite-based SST and chlorophyll concentrations calculated over the entire region and season versus those calculated using only the times and locations of our discrete sample collection. Undersampling bias in temperature and salinity effects on pCO_2 (equation 3) are calculated solely from the mean percent difference between fully-sampled and discrete sample-based SST. The combined effects of uncertainty in carbonate chemistry estimates and in gas exchange, NCP, and $CaCO_3$ production rates in equations 5-7 are propagated following standard methods. The magnitude of DIC physical supply is determined as the residual term in both equations (1) and (2) and the error in this term is determined by propagating error from each individual term following standard methods.

4.4 RESULTS AND DISCUSSION

4.4.1 *Seasonal cycle of DIC and pCO_2*

DIC concentrations in the mixed layer follow a similar seasonal cycle in all three regions, with an annual maximum in spring and a minimum in fall (Figure 4.2; Table 4.1). This is consistent with biological removal of DIC during the spring through fall productive season and physical supply of DIC from winter mixing and vertical diffusion. The amplitude of the DIC seasonal cycle increases westward across the basin, consistent with westward increases in both summertime NCP and winter mixed layer depths.

Mixed layer pCO_2 is lower than atmospheric pCO_2 (394 ± 5 μatm) for the majority of the year in all three regions and follows a seasonal cycle offset from that of DIC, with maximum in summer and minimum in winter (Figure 4.2; Table 4.1). Variability of individual discrete sample measurements around the mean seasonal cycle is greater for pCO_2 than for DIC, and in contrast to DIC, the amplitude of the seasonal cycle in pCO_2 is lower in the Kuroshio region than the West and East. Previous global-scale analysis has demonstrated that pCO_2 seasonal cycles reflect the combined effects of two offsetting processes: temperature effects which increase pCO_2 during summertime and decrease pCO_2 during wintertime and non-temperature effects which decrease pCO_2 during summer due to biological drawdown and increase pCO_2 in winter due to vertical physical supply of high-pCO_2 waters, with temperature effects dominating in the subtropics and non-temperature effects dominating in the subarctic North Pacific [*Takahashi et al.*, 2002]. Our observed seasonal pCO_2 cycle reflects the competing effects of both processes at the interface between the subtropical and subarctic regimes which both mute the amplitude of the seasonal cycle and increase variability.

To evaluate the pCO_2 seasonal cycle independent of the temperature effect we calculate the temperature-normalized pCO_2 seasonal cycle (equation 1 from *Takahashi et al.* [2002]) at the mean annual SST for each region (Figure 4.2). The coincidence of seasonal cycles in temperature-normalized pCO_2 and DIC (Figure 4.2) implies that the lag between pCO_2 and DIC maxima results from the temperature effect on pCO_2. Furthermore, the westward increase in amplitudes of DIC and temperature-normalized pCO_2 indicate that the non-temperature effects on pCO_2 are caused by the same processes causing seasonal changes in DIC.

4.4.2 *Factors influencing the seasonal cycle of mixed layer DIC and pCO_2*

To quantitatively evaluate the factors influencing the observed seasonal cycles in mixed layer DIC and pCO_2, we consider the role of each component term in equations (1) and (2) for DIC and pCO_2 respectively (Figure 4.3). Air-sea CO_2 flux drives a small but steady increase in mixed layer DIC and pCO_2 via net uptake of atmospheric CO_2 throughout the year except in summer in the Western and Eastern regions, when the ocean outgases CO_2. NCP is the primary factor driving spring through fall decreases in both DIC and pCO_2. While both NCP and $CaCO_3$ production lead to a net removal of DIC, $CaCO_3$ production causes a net increase in pCO_2 by decreasing TA in a 2:1 ratio to DIC. However, even in the East with the largest specified PIC:NCP ratio across the basin of 0.3, $CaCO_3$ production only offsets ~20% of the pCO_2 drawdown due to NCP. The temperature effect increases pCO_2 during periods of warming in spring and summer and decreases pCO_2 during fall and winter cooling. The large temperature-driven increase in pCO_2 during summer largely offsets the NCP-driven pCO_2 drawdown, with a westward-increasing seasonal cycle in SST increasing the offset in tandem with the westward-increasing productive season NCP rates and producing a smaller seasonal cycle in observed pCO_2 as compared to DIC. The effect of seasonal changes in salinity on pCO_2 is negligible, and therefore not shown in Figure 4.3 or further discussed in the results.

Seasonal changes in mixed layer depth (Figure 4.S4) vary the effect of carbon fluxes on mixed layer DIC concentrations and pCO_2, with effects amplified during the stratified summer season when there is a smaller volume of water and dampened in the winter when there is a larger volume of water. Therefore, even though the rate of air-sea CO_2 flux is greatest in winter in the Kuroshio and Western regions, its influence on DIC and pCO_2 in winter is less than half that in fall because winter mixed layer depths are 2-4× deeper. Similarly, the influence of

biological removal of DIC via NCP is enhanced in the summer even though NCP rates per square meter are greater in spring and fall than in summer.

Seasonal patterns of physical supply, calculated as the residual term in both equations (1) and (2), are similar for both DIC and pCO_2 (Figure 4.3). This is consistent with DIC transport rather than TA transport as the primary influence of physical supply on pCO_2 such that the temperature effect rather than physical supply dominates the difference between the DIC and pCO_2 seasonal cycles (also consistent with the coincident seasonal cycles in DIC and temperature-normalized pCO_2; Figure 4.2). The physical supply term calculated as the residual in the DIC and pCO_2 budgets (equations 1 and 2) includes both horizontal transport due to geostrophic and Ekman-driven advection as well as vertical diffusive mixing, entrainment and upwelling. Previous work in the North Pacific transition zone region has demonstrated that vertical supply of high-DIC waters leads to an increase in mixed layer pCO_2 during the period of intense entrainment and vertical diffusion from late fall through early spring [*Ayers and Lozier*, 2012]. Similarly, our estimates of physical DIC supply are greatest in fall and winter. Advective transport has steady effects throughout the year in the transition zone region, with Ekman transport supplying high DIC waters from the north and geostrophic transport by the Kuroshio and Kuroshio Extension currents supplying low DIC waters that leads to a net removal of DIC from the region and a decrease in mixed layer pCO_2 [*Ayers and Lozier*, 2012]. In spring, we find that the influence of physical supply is near zero in the Eastern and Western regions and slightly negative (tending to remove mixed layer DIC and pCO_2) in the Kuroshio, potentially reflecting the influence of geostrophic removal of DIC that dominates over the influence of vertical supply once spring stratification begins. In summer, physical supply increases mixed layer DIC and pCO_2 in our study regions, likely due to reduced geostrophic removal of DIC by the Kuroshio

Extension, with the effects of advective DIC supply amplified by the shallow summer mixed layers, as discussed above.

4.4.3 *Annual influences on DIC*

Annual influences on DIC are calculated following equation (1) assuming that over a composite annual cycle $\frac{\partial \mathrm{DIC}}{\partial t} \approx 0$. Annual flux rates are determined for each RHS term in equation (1), with two separate DIC budgets calculated integrating, first, to the base of the seasonally-varying mixed layer depth and, second, to the winter ventilation depth.

Air-sea CO_2 flux leads to a net annual increase in ocean DIC inventory in all three regions, with rates of 2.7 ± 0.9, 2.3 ± 0.4 and 2.1 ± 0.3 mol C m^{-2} yr^{-1} in the Kuroshio, Western and Eastern regions, respectively. This pattern of westward-intensified ocean CO_2 uptake across the basin is consistent with the spatial trends identified by *Takahashi et al.* [2009] (Figure 4.1) but is stronger by ~0.6-0.9 mol C m^{-2} yr^{-1} (~30-60%) than the rates determined by *Takahashi et al.* [2009]. The decade-long interval between the *Takahashi et al.* [2009] reference year of 2000 and the 2008-2012 sampling period of our study is not long enough to be able to distinguish potential strengthening of the ocean carbon sink from natural variability [*McKinley et al.*, 2016]. Differences between our estimates and those of *Takahashi et al.* [2009] may also result from interpolation choices in developing the global climatology or from differences in the choice of air-sea gas transfer parameterizations, as well as actual differences between the measurement time periods.

Biological export of organic carbon (NCP) removes sufficient DIC to more than counterbalance the annual DIC increase due to air-sea CO_2 flux if the annual DIC inventory is computed to the base of the seasonally-varying mixed layer (green circles in Figure 4.4),. However, integrating the DIC budget to a constant winter ventilation depth for each region paints

a different picture. Although organic carbon export from the stratified mixed layer in spring through fall is greatest in the Kuroshio and decreases eastward across the basin, much of this organic material is remineralized below the base of the seasonally stratified mixed layer and reenters the mixed layer during deep winter mixing in the western basin, ventilating it to the atmosphere [*Palevsky et al.*, 2016]. Estimates of annual NCP are significantly reduced in the Kuroshio and Western regions when accounting for winter ventilation, whereas the reduction is small in the Eastern region due a strong permanent halocline that prevents winter mixing below ~120 m (green bars in Figure 4.4).

Integrating the annual DIC budget to the winter ventilation depth, it becomes clear that the relative roles of NCP and of physical supply of DIC vary considerably across the basin. NCP remains more than able to counterbalance the DIC increase due to air-sea CO_2 flux in the East. In the Kuroshio region, by contrast, ~90% of seasonal NCP is remineralized and ventilated back to the atmosphere such that the fraction of NCP that remains sequestered on an annual basis can only counterbalance a small fraction of the DIC increase due to air-sea CO_2 flux and, as a result, physical processes must counterbalance the CO_2 input from gas exchange over the annual cycle. According to analysis by [*Ayers and Lozier* [2012], the only physical process that leads to a net removal of DIC in this region is geostrophic advection, which transports low-DIC subtropical waters northward into the region via the Kuroshio Current and exports high-DIC eastward via the Kuroshio Extension. All other physical processes, including Ekman transport and vertical supply via entrainment, diffusive mixing and upwelling, yield a net supply of DIC. Our calculated physical supply term (residual in equation 1) represents the net result of all physical processes. Across the basin, the role of physical processes changes from being a net DIC sink in the west to

a net DIC source in the east (Figure 4.4), which follows the eastward decrease in the strength of geostrophic transport by the Kuroshio Extension.

The influence of $CaCO_3$ production on the DIC budget presented here assumes that none of the $CaCO_3$ exported from the seasonally-stratified mixed layer dissolves above the winter ventilation depth. Despite expected faster sinking of $CaCO_3$-ballasted particles [*Armstrong et al.*, 2002; *Klaas and Archer*, 2002], this is likely an overestimate of the contribution $CaCO_3$ production of to the annual DIC budget, since recent sediment trap measurements in the western subarctic gyre show a decrease in $CaCO_3$ flux between 60 and 200 m, likely driven by shallow aragonite and calcite saturation depths at 100 m and 200 m respectively [*Honda et al.*, 2015]. However, even without allowing for dissolution of sinking $CaCO_3$ particles, $CaCO_3$ production provides a fairly minor contribution to the annual DIC budget.

4.4.4 *Annual influences on surface ocean pCO_2 and air-sea CO_2 flux*

Annual influences on pCO_2 are calculated following equation (2) assuming that over a composite annual cycle $\frac{\partial \mathrm{pCO_2}}{\partial t} \approx 0$. This simplifying assumption is justified because rates of surface water pCO_2 increase in the North Pacific are < 3 μatm yr^{-1} [*Takahashi et al.*, 2009], which is negligible given the magnitude of other terms (Figure 4.5). Annual influences on mixed layer pCO_2 are determined for each RHS term in equation (2), with the roles of NCP and physical supply calculated both with and without accounting for winter ventilation (Figure 4.5), as in the annual DIC budget (Figure 4.4).

It is important to note that the impact of a given carbon flux on mixed layer pCO_2 depends on mixed layer depth because the pCO_2 change depends on the DIC concentration change (via equation 8) and the DIC concentration change depends inversely on mixed layer depth, as described in section 4.2. Thus a given NCP flux out of the shallow stratified mixed

layer in summer decreases the pCO_2 more than the return of this same flux (as DIC) into a deep mixed layer in winter increases the pCO_2. This mixed layer depth effect weights the annual pCO_2 cycle towards summertime NCP and away from wintertime DIC supply via vertical mixing and entrainment that ventilates remineralized organic carbon. We approximate the timing of winter ventilation based on seasonal entrainment rates in each season, which indicate that ~30% of ventilation occurs during initial mixed layer deepening in fall and 10-20% occurs during continued entrainment in early spring in the West and East, while the dominant remainder of ventilation occurs during winter. This ventilation lessens the annual influence of NCP towards reducing pCO_2 (green bars in Figure 4.5) as compared with the estimate not accounting for ventilation of remineralized seasonally-exported carbon (green filled circles in Figure 4.5). However, despite ventilation of 90% and 40% of seasonally-exported carbon in the Kuroshio and Western regions respectively, the reduction in the influence of NCP on annual drawdown of surface ocean pCO_2 is only 30% and 20% respectively. This strong effect of seasonal timing on the ability of NCP to influence surface ocean pCO_2 is due to the seasonal cycle of mixed layer depths, where winter mixed layers are 8× deeper than summer mixed layers in the Kuroshio and 5× deeper in the West and East (Figure 4.S4).

To further illustrate this point, as a thought experiment, we calculate the influence on pCO_2 of the same total annual NCP rate determined at the winter ventilation depth but redistributed seasonally such that NCP rates are reduced from spring through fall rather than seasonally exported and subsequently remineralized and ventilated as mixed layers deepen (black circles in Figure 4.5). This scenario significantly diminishes the ability of NCP to reduce surface ocean pCO_2 on an annual basis, although the total annual NCP flux is unchanged from that in the more realistic ventilation-based calculation of the influence of NCP (green bars in

Figure 4.5). Since both scenarios are based on the same annual NCP flux rate, both are consistent with the DIC budget accounting for the effects of winter ventilation (colored bars in Figure 4.4) despite their differing effects on pCO_2. This thought experiment, though unrealistic, demonstrates that knowledge of the timing of export and ventilation, as well as the rates, is important for quantifying the influence of NCP and ventilation on mixed layer pCO_2 and thus on the air-sea CO_2 flux.

Our analysis indicates that export of organic material (NCP) is the primary process drawing down pCO_2 in the three regions (Figure 4.5) although the magnitude of its importance depends on the timing of the physical processes ventilating remineralized organic matter back to the mixed layer as DIC, as discussed above. Our estimates indicate that physical processes cause a net annual increase in pCO_2 in all three regions (86 ± 222, 95 ± 145 and 74 ± 86 μatm yr^{-1} in the Kuroshio, Western, and Eastern regions respectively) albeit with large uncertainties, since the physical supply term is calculated as the residual in equation (2) with an error that depends on errors in all other terms, including significant uncertainty in seasonal MLD estimates. These results are consistent with those of *Ayers and Lozier* [2012] who estimated that physical processes cause a net pCO_2 increase of 59 ± 17 μatm yr^{-1} in the transition zone, with pCO_2 increases from Ekman transport and vertical mixing/entrainment more than counteracting the pCO_2 decrease from geostrophic advection.

The influence of $CaCO_3$ production on pCO_2 is substantially smaller than the influence of NCP and physical processes (Figure 4.5). However, it does drive a biological counter-pump that annually increases surface ocean pCO_2 at more than half the rate of air-sea CO_2 flux in the Eastern and Western regions. Improved estimates of the rate of $CaCO_3$ production are needed to

constrain widely varying literature values, and predict potential future changes in $CaCO_3$ production that could influence the strength of the North Pacific ocean carbon sink.

Assessing the drivers of air-sea CO_2 flux requires us to consider not only the annual changes in surface ocean pCO_2 (Figure 4.5), but also the effect of those pCO_2 changes in driving CO_2 exchange between the surface ocean and atmosphere. Wintertime increases in CO_2 solubility and wind speed-dependent air-sea gas transfer rates (K_0 and k_{CO_2}, respectively, in equation 10) enhance the leverage of winter over summer pCO_2 changes in driving air-sea CO_2 flux by 4×, 2.7×, and 2.9× in the Kuroshio, Western, and Eastern regions respectively. This serves to partially offset the mixed layer depth effect described earlier, which enhances the influence of carbon fluxes from the mixed layer in summer as compared to winter. Seasonal timing is thus important not only in determining the influence of carbon fluxes on surface ocean pCO_2 but also in determining the influence of pCO_2 changes in driving air-sea CO_2 flux.

Although the temperature effect is an important influence on the pCO_2 seasonal cycle (Figure 4.3) its influence on pCO_2 over an annual basis is indistinguishable from zero in all regions (Figure 4.5). This result is consistent with a previous analysis of climatological pCO_2 in the North Pacific transition zone [*Ayers and Lozier*, 2012]. Nevertheless, wintertime increases in K_0 and k_{CO_2} magnify the influence of winter temperature-driven decreases in pCO_2 on annual air-sea CO_2 flux rates. If K_0 and k_{CO_2} were held constant at the annual mean in each region, annual air-sea CO_2 flux would be 91%, 78% and 73% of the actual rates in the Kuroshio, Western and Eastern regions respectively. These potential reductions are similar to those previously estimated for the full transition zone region [*Ayers and Lozier*, 2012]. This indicates that although seasonal asymmetries in the leverage of surface ocean pCO_2 on air-sea CO_2 flux

(primarily due to higher wind speeds in winter) do drive a portion of the annual ocean carbon sink, this is a second-order effect.

4.5 CONCLUSIONS

In this study, we have combined measurements of the complete carbonate chemistry system across the North Pacific basin throughout the full annual cycle with previously-described estimates of NCP based on O_2/Ar measurements [*Palevsky et al.*, 2016] to investigate the relative roles of chemical, physical and biological processes in driving uptake of atmospheric CO_2. Air-sea CO_2 exchange is an atmospheric CO_2 sink (and source of DIC to the surface ocean) across the North Pacific basin. We find that the annual SST cycle has a strong effect on the seasonal pCO_2 cycle (Figures 4.2-4.3) but little effect on annual changes in surface ocean pCO_2 (Figure 4.5), and can account for less than 20% of the region's annual air-sea CO_2 flux, requiring that physical and biological processes drive annual ocean CO_2 uptake.

The annual DIC budget (Figure 4.4) shows an east-west trend across the basin with geostrophic transport as the dominant DIC sink in the Kuroshio region and NCP as the dominant DIC sink in the East. This spatial trend is only apparent by accounting for annual rates of NCP calculated to the winter ventilation depth, which reveal that ~90% of the seasonally-exported organic carbon in the Kuroshio region is subsequently remineralized and entrained into the mixed layer as DIC during deep winter mixing. Without accounting for winter ventilation, we would overestimate the influence of vertical DIC supply by counting this ventilation of remineralized carbon as a physical influence rather than a reduction in the rate of annual NCP. The effects of winter ventilation on surface ocean pCO_2 are still substantial but more muted (Figure 4.5). The influence of annual NCP on surface ocean pCO_2 depends not only on the

magnitude of the annual flux but also on its timing, since an identical flux has a larger influence on mixed layer DIC concentrations and thus pCO_2 when exported from a shallow summer mixed layer than a deep winter mixed layer.

Annual air-sea CO_2 flux increases westward across the basin, from 2.1 ± 0.3 mol C m^{-2} yr^{-1} in the East to 2.7 ± 0.9 mol C m^{-2} yr^{-1} in the Kuroshio region. These rates are 4-5× the global mean rate of ocean carbon uptake, underscoring the previously recognized role of the North Pacific as a significant sink of atmospheric CO_2 [*Takahashi et al.*, 2009]. We demonstrate that the biological pump (NCP) plays a key role in driving the North Pacific ocean carbon sink, and also that the influence of NCP on air-sea CO_2 flux depends not only on the magnitude of organic material export rates but also on the magnitude and timing of mixed layer deepening during fall and winter and the seasonal cycle in wind-speed driven gas exchange. Seasonal variations in NCP, mixed layer depth, and wind speed have a particularly strong impact on ocean CO_2 uptake in high latitude regions with a strong seasonal cycle such as the Kuroshio, where deep winter mixed layers return a significant fraction of exported organic carbon to the surface ocean, and ultimately atmosphere, as CO_2. Thus future studies aiming at unraveling the role of the biological pump in driving the ocean CO_2 sink need to not only focus on estimating the annual NCP rate but also account for the timing of seasonal export and impact of winter ventilation.

4.6 FIGURES AND TABLES

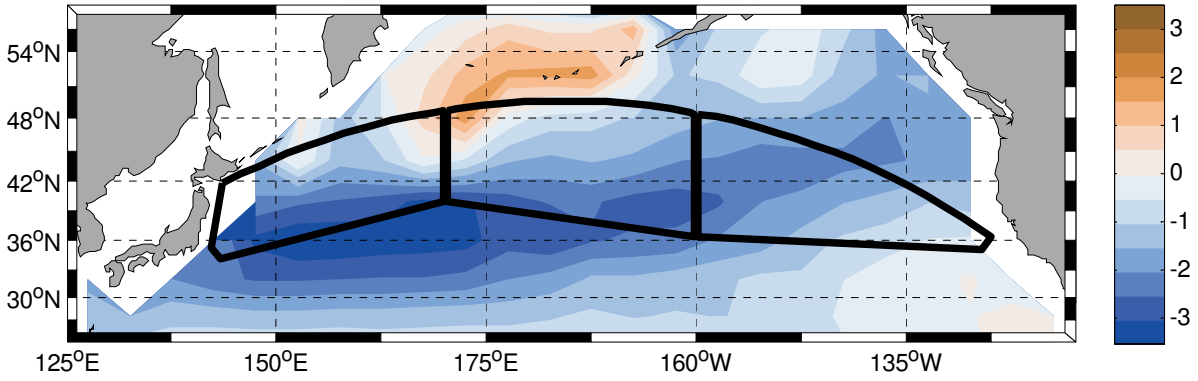

Figure 4.1. Locations of the three container ship sampling regions are outlined in black (from west to east, the Kuroshio, West and East) and shown over a map of climatological mean annual air-sea CO_2 flux (mol C m^{-2} yr^{-1}) normalized to the year 2000 (data from *Takahashi et al.* [2009]).

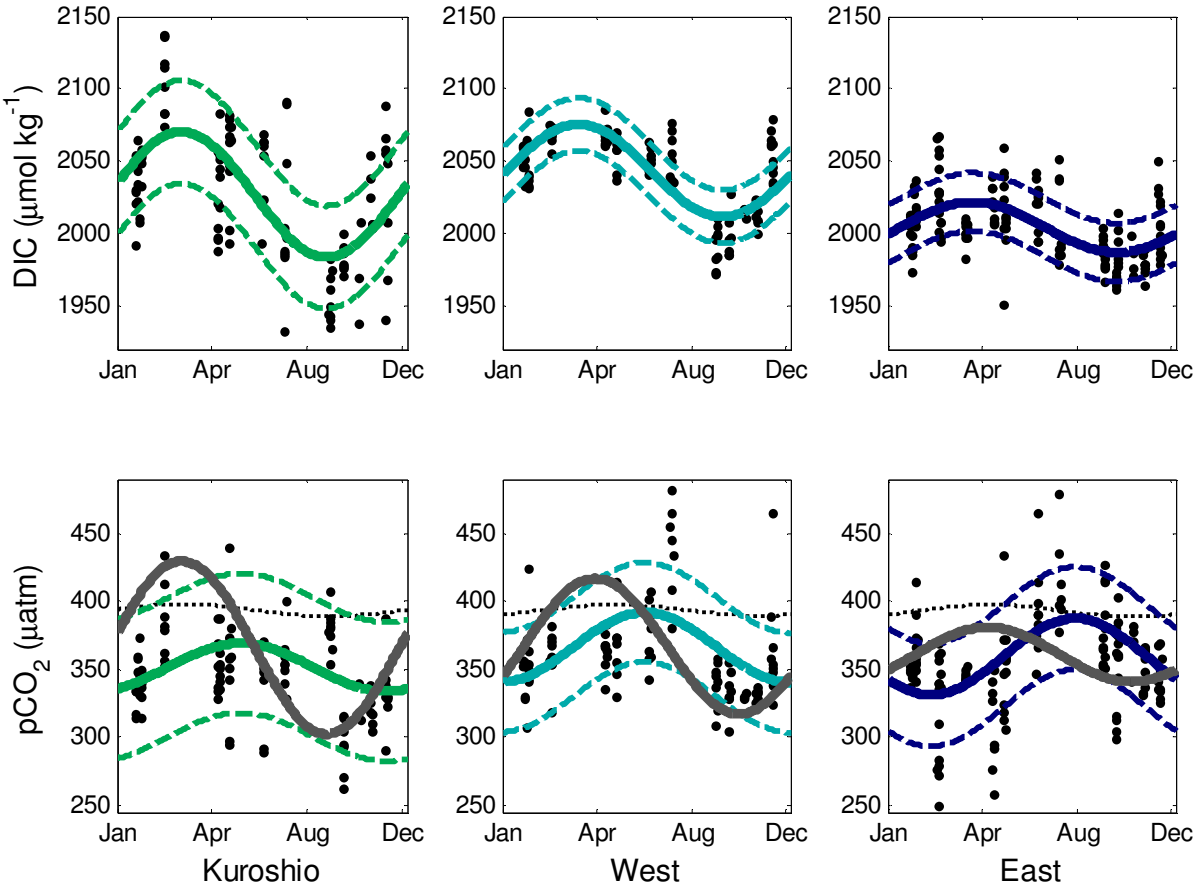

Figure 4.2. Composite annual cycle for DIC and seawater pCO_2 in each region. Black dots show all discrete sample measurements in a given region (two samples with pCO_2 < 250 µatm and seven samples with pCO_2 > 500 µatm are outside the y-axis bounds). The solid colored lines are harmonic fits to the data describing the annual cycle and the dashed colored lines show the harmonic fit ± root mean squared error. For pCO_2, the solid gray line shows the pCO_2 seasonal cycle normalized to mean annual SST for each region and atmospheric pCO_2 is shown as a dashed black line.

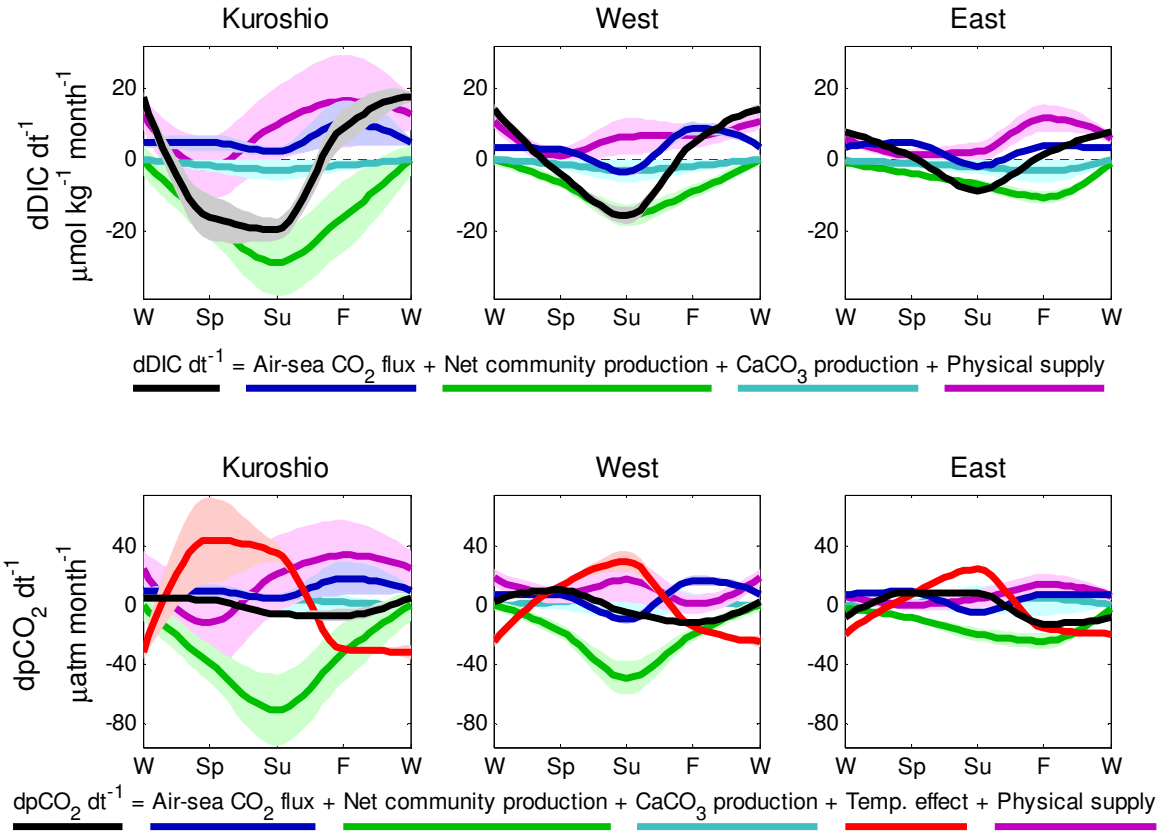

Figure 4.3. Seasonal influences on DIC concentrations (top) and seawater pCO_2 (bottom) in the surface mixed layer in each region, calculated following equations (1) and (2), respectively. Positive (negative) values represent increases (decreases) in mixed layer DIC and pCO_2. The salinity effect on seawater pCO_2 is negligible and is omitted for clarity.

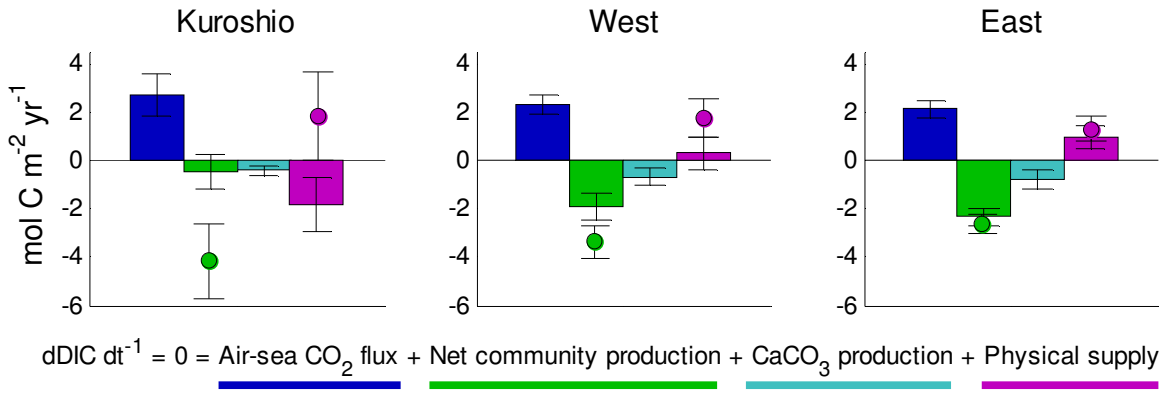

Figure 4.4. Annual DIC budget for each region, calculated following equation (1). Positive (negative) values represent increases (decreases) in surface ocean DIC. Note the differing influences of NCP and physical supply on the DIC budget integrated to the winter ventilation depth (bars) compared to the DIC budget integrated to the base of the seasonally-varying mixed layer depth (filled circles). See text for discussion.

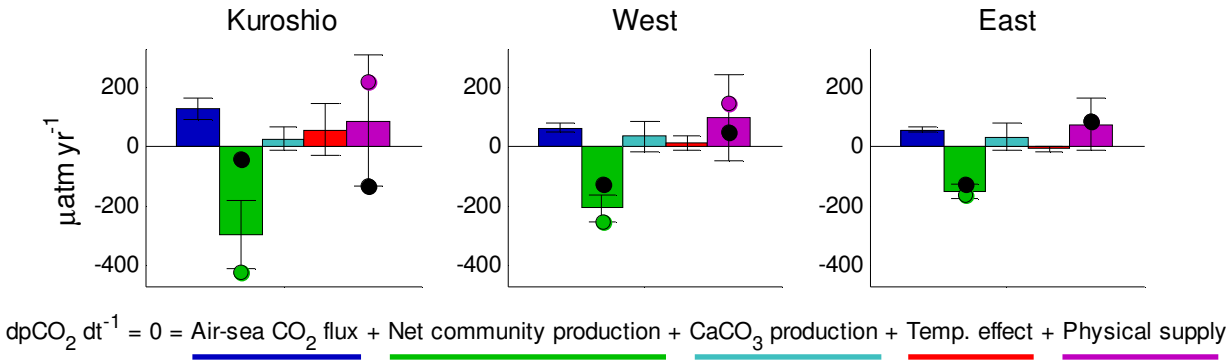

Figure 4.5. Annual influences on pCO_2 in the surface mixed layer in each region, calculated following equation (2). Positive (negative) values represent increases (decreases) in mixed layer pCO_2. The salinity effect is negligible and is omitted for clarity. The colored circles for NCP and physical supply integrate effects on the surface mixed layer shown in Figure 4. The colored bars account for winter ventilation, with a best estimate of when that ventilation occurs based on seasonal entrainment rates (see text for details). The black dots represent a thought experiment scenario where the total annual NCP rate is equivalent to the winter ventilation estimate shown in the colored bars, but results from reduced productive season NCP rather than winter ventilation.

Table 4.1. Summary of regional mean carbonate chemistry and air-sea CO_2 flux rates across the North Pacific

Kuroshio (142°E – 170°E)					
	No. of samples	DIC[a] (μmol kg^{-1})	TA[a] (μmol kg^{-1})	pCO_2[a] (μatm)	Air-sea CO_2 flux[b]
Spring (MAM)	24	2042 ± 1 (31)	2264 ± 1 (18)	360 ± 4 (43)	5.7 ± 2.5
Summer (JJA)	17	2026 ± 1 (45)	2239 ± 1 (18)	371 ± 3 (101)	0.9 ± 0.4
Fall (SON)	27	1982 ± 1 (31)	2237 ± 2 (17)	333 ± 2 (38)	8.7 ± 5.2
Winter (DJF)	36	2051 ± 1 (42)	2255 ± 1 (25)	348 ± 2 (28)	14.8 ± 2.6
Annual	104				2.7 ± 0.9
West (170°E – 160°W)					
	No. of samples	DIC[a] (μmol kg^{-1})	TA[a] (μmol kg^{-1})	pCO_2[a] (μatm)	Air-sea CO_2 flux[b]
Spring (MAM)	27	2065 ± 1 (10)	2230 ± 1 (16)	364 ± 3 (19)	6.8 ± 1.6
Summer (JJA)	17	2051 ± 1 (13)	2205 ± 1 (8)	420 ± 4 (57)	-2.4 ± 0.7
Fall (SON)	27	2001 ± 1 (14)	2222 ± 1 (17)	227 ± 2 (15)	10.2 ± 1.7
Winter (DJF)	27	2052 ± 1 (15)	2237 ± 1 (21)	356 ± 3 (30)	10.6 ± 2.1
Annual	98				2.3 ± 0.4
East (160°W – 125°W)					
	No. of samples	DIC[a] (μmol kg^{-1})	TA[a] (μmol kg^{-1})	pCO_2[a] (μatm)	Air-sea CO_2 flux[b]
Spring (MAM)	50	2017 ± 1 (23)	2225 ± 1 (21)	332 ± 2 (37)	11.0 ± 1.6
Summer (JJA)	20	2012 ± 1 (23)	2201 ± 1 (7)	414 ± 4 (54)	-1.0 ± 0.3
Fall (SON)	39	1982 ± 1 (12)	2208 ± 2 (8)	363 ± 3 (28)	4.6 ± 1.0
Winter (DJF)	36	2007 ± 1 (18)	2213 ± 1 (19)	353 ± 2 (17)	8.8 ± 1.5
Annual	145				2.1 ± 0.3

[a] Results are given as mean ± uncertainty, reflecting methodological error in individual measurements. 1σ variability about the mean is given in parentheses, reflecting regional variability.

[b] Seasonal rates for air-sea CO_2 flux are given in mmol C m^{-2} $d^{-1}$and annual rates are in mol C m^{-2} yr^{-1}. Results are given as mean ± uncertainty, reflecting both methodological error and sampling bias (see text for details).

4.7 SUPPLEMENTARY FIGURES

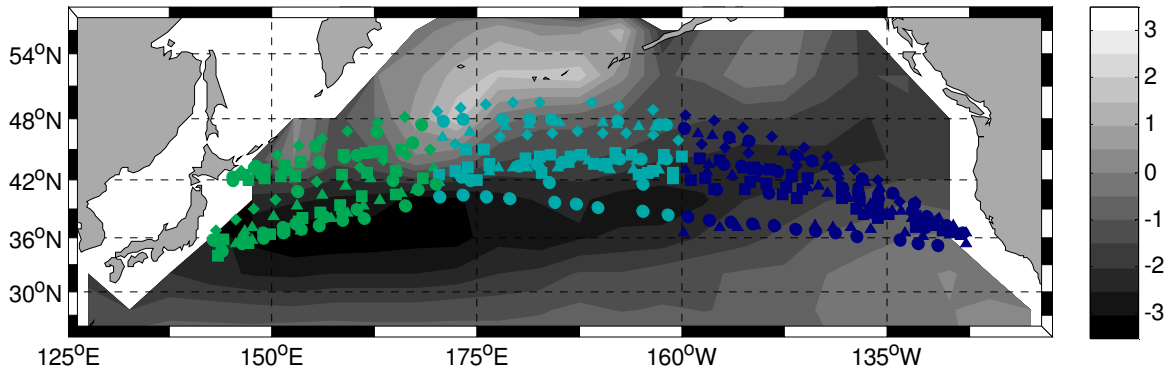

Figure 4.S1. Mixed layer discrete samples collected on fifteen basin-wide transects of the North Pacific between 2008 and 2012 are divided for analysis into three regions: the Kuroshio (green), the Western region (light blue), and the Eastern region (dark blue). The annual cycle is divided by season: spring (Mar. – May, triangles), summer (June – Aug., diamonds), fall (Sept. – Nov., squares), and winter (Dec. – Feb., circles). Sample locations are overlain on climatological mean annual air-seaCO_2 flux (mol C m^{-2} yr^{-1}) normalized to the year 2000 for the North Pacific (data from *Takahashi et al.* [2009]), as shown in Figure 1.

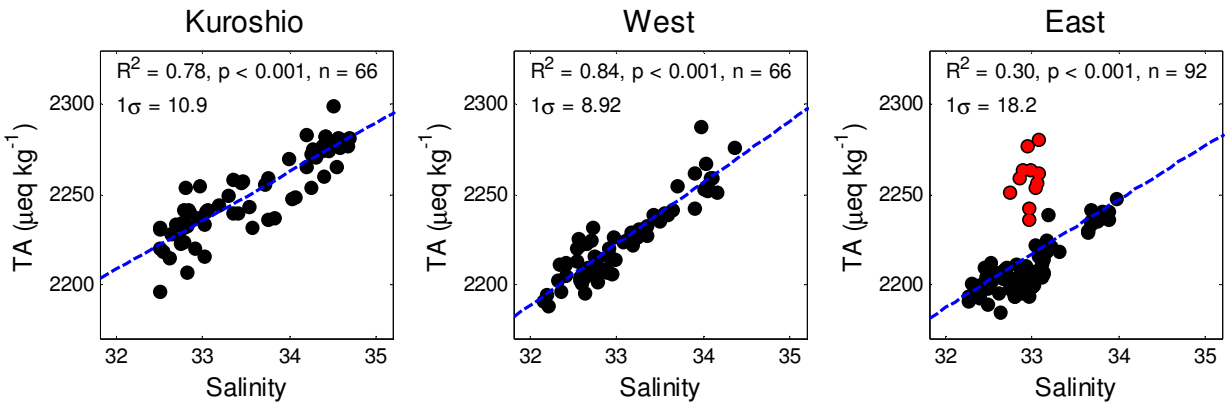

Figure 4.S2. Relationships between total alkalinity (TA) and salinity (S) for each region, based on all points where TA was directly measured (not including points where TA was calculated from DIC and pCO_2). Regional relationships were used to fill TA at points with DIC measurements that had neither pCO_2 or TA measurements available (51 out of 347 total sample locations included in this analysis). The red points are outliers from the TA-S relationship for the Eastern region, but are not members of any distinguishable water mass nor were sample measurements compromised, so they are included in the Eastern region TA-S regression. The influence of these points on the ultimate calculations of seasonal mean values is minimal.

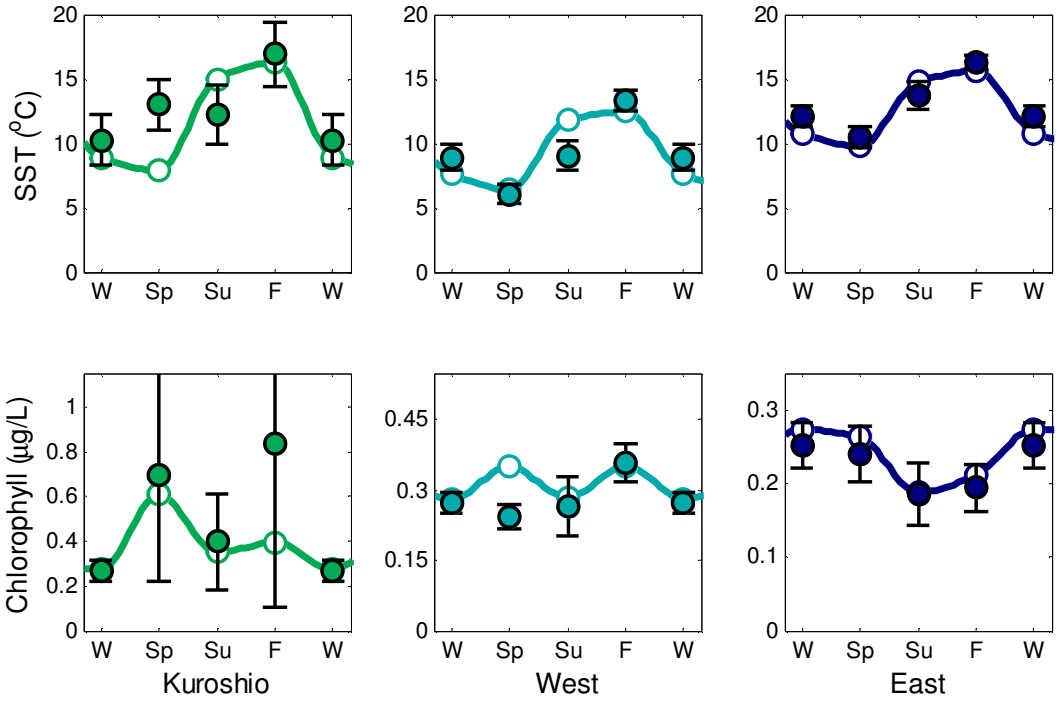

Figure 4.S3. Analysis of sampling bias after Figure 2 in *Palevsky et al.* [2016], recomputed using only sampling locations with carbonate chemistry measurements included in the analysis in this paper. Plots show the seasonal cycle of sea surface temperature (SST, top) and chlorophyll (bottom) in each region, from MODIS satellite data. Open circles connected by solid lines show mean values over all points in the region in all three months comprising each season in every year 2008-2012. Filled circles show mean values sampled only at the locations and times when discrete samples were collected during this study. Error bars represent twice the standard error of the mean (error bars not shown are smaller than the marker size). Discrepancies between the solid and open circles reflect undersampling bias. Note the varying y-axis for chlorophyll plots.

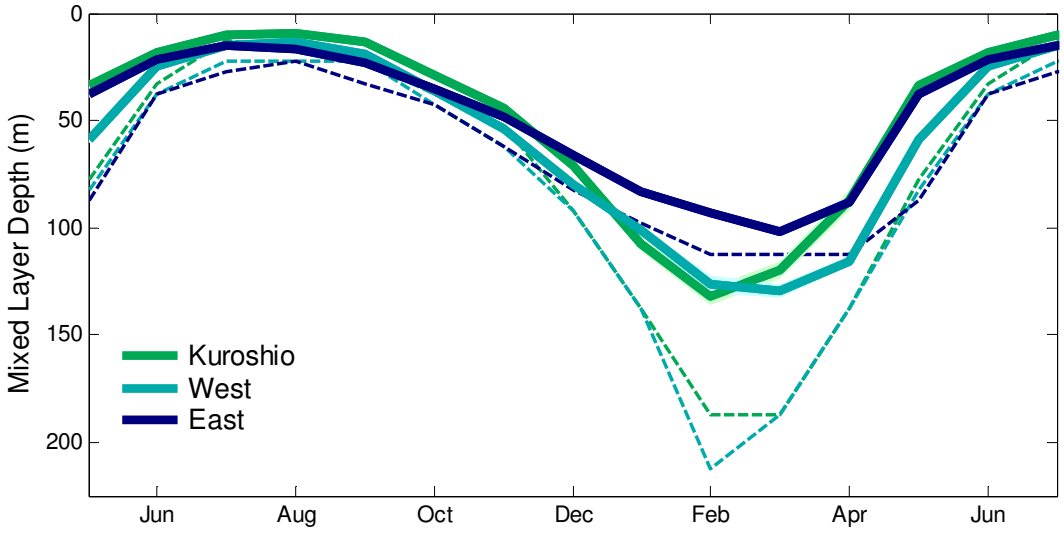

Figure 4.S4. Annual cycle of mixed layer depth (MLD) in each region, determined from World Ocean Atlas 2013 temperature and salinity data (MLD criterion of 0.125 kg m^{-3} density increase from the surface). Solid lines are mean ± standard error of all locations with discrete sample measurements in each region and dashed lines are the maximum monthly MLD in each region.

Chapter 5.

Conclusion

5.1 SUMMARY OF MAIN RESULTS

This dissertation assesses the rate and efficiency of the North Pacific biological pump, and its role in the regional ocean carbon sink. Our approach used surface ocean geochemical measurements sampled on sixteen repeat container ship transects between Hong Kong and Long Beach, CA from 2008-2012 to quantify gross primary production (GPP) and net community production (NCP), which together define the rate and efficiency of the biological pump, as well as rates of air-sea CO_2 flux. Together, these rate estimates enabled us to assess the relative influences of biological, chemical and physical drivers of the ocean carbon sink. This dissertation represents the first time all three of these key rates have been quantified simultaneously on a basin-wide scale over the full annual cycle based on geochemical measurements.

A major influence on the geochemical observations presented in Chapters 2 and 4 is the basin-wide gradient between the physically dynamic western basin influenced by the Kuroshio and Oyashio currents and deep (>200 m) winter mixed layers and the eastern basin, which experiences weaker advective transport and shallower winter mixing inhibited by a strong permanent halocline at ~120 m. The seasonal cycles of GPP, NCP, sea surface temperature, and dissolved inorganic carbon (DIC) concentrations are all strongest in the Kuroshio region west of 170°E and decrease eastward across the basin. Previous estimates of productivity at time-series stations agree with our regional estimates east of 160°W but not in the Kuroshio region, likely

reflecting higher spatial variability in the western basin that cannot be captured by measurements at a single time-series station.

In Chapter 2, we found that rates of GPP and of NCP from the stratified mixed layer in spring through fall are highest in the Kuroshio region and decrease eastward, likely due to greater nutrient supply from deeper winter mixing and aeolian dust supply in the western basin. However, ~40–90% of the organic carbon exported below the seasonally-stratified mixed layers west of 160°W is remineralized and ventilated back to the atmosphere as CO_2 during deep winter mixing, whereas only ~10% of seasonally exported carbon east of 160°W is ventilated in winter. Due to this ventilation, the annual carbon export (sequestration) rate and efficiency decrease westward across the basin from export of 2.3 ± 0.3 mol C m^{-2} yr^{-1} east of 160°W to 0.5 ± 0.7 mol C m^{-2} yr^{-1} west of 170°E, opposing the basin-wide trend in GPP and in seasonal NCP. This demonstrates the importance of estimating NCP integrated to the winter ventilation depth in order to determine the influence of biological carbon export in sequestering atmospheric carbon over annual to multi-annual time scales, particularly in regions with deep winter mixing.

Chapter 3 compared estimates of primary production, export production and export efficiency from satellite-based primary production and export efficiency algorithms and a dynamic global ocean model including embedded ecosystem and biogeochemistry components with in situ geochemical-based GPP and NCP estimates from the three basin-wide regions presented in Chapter 2 as well previous geochemical measurements at two time-series stations in the subarctic and subtropical gyres. No single satellite- or model-based approach matched the geochemically-determined seasonal and annual primary and export production rates throughout the North Pacific. Discrepancies in primary production were particularly pronounced in the higher-latitude regions in winter and spring, which have previously had sparse observational data

available for development, calibration or validation of models. We also note that the satellite-based approach to NCP cannot account for the effects of winter ventilation that we identified in Chapter 2 as key processes influencing annual NCP. These results underscore the need to evaluate satellite- and model-based estimates using multiple productivity parameters measured over broad ocean regions throughout the annual cycle, requiring the collection of additional geochemical datasets such as that presented in Chapter 2 to facilitate this comparison.

Chapter 4 considered the role of NCP rates calculated in Chapter 2 in the context of all chemical, physical and biological processes influencing the marine carbon cycle in the North Pacific. The rate of air-sea CO_2 flux is greatest in the Kuroshio region (2.7 ± 0.9 mol C m^{-2} yr^{-1}) and decreases eastward across the basin (2.1 ± 0.3 mol C m^{-2} yr^{-1} east of 160°W). In the eastern basin, DIC removal due to biological carbon export below the winter ventilation depth more than fully compensates for the DIC increase due to this uptake of atmospheric CO_2. In the region west of 170°E influenced by deep winter ventilation, however, annual NCP only offsets ~20% of DIC increase due to atmospheric CO_2 uptake, requiring significant DIC removal by physical processes, likely dominated by geostrophic advection. Temperature-driven solubility effects have no net influence on ocean pCO_2 and can account for <20% of annual CO_2 uptake. The seasonal timing of NCP as well as its annual magnitude strongly affects the influence of the biological pump on air-sea CO_2 flux, since export of fixed carbon has a stronger influence on DIC concentrations and thus on surface ocean pCO_2 in summer when mixed layers are shallow, but changes in pCO_2 have a stronger influence on air-sea CO_2 flux in winter when high wind speeds drive more vigorous gas exchange. This indicates that it is necessary to determine the seasonal timing as well as the annual magnitude of NCP to determine the influence of the biological pump on the ocean carbon sink.

5.2 IMPLICATIONS AND FUTURE WORK

The results of this dissertation's analysis in the North Pacific provide lessons for future geochemical measurements of the biological pump and the ocean carbon sink in other ocean regions, as well as development of mechanistic models and algorithms. This work has demonstrated the important influence of winter ventilation in determining the rate at which biological carbon export sequesters carbon on annual to multi-annual time scales [*Palevsky et al.*, 2016]. Many global-scale analyses pick a standard global depth [e.g. 100 m; *Henson et al.*, 2011; *Bopp et al.*, 2013; *Laufkötter et al.*, 2015] or use the depth of the euphotic zone [e.g. *Laws et al.*, 2000, 2011; *Dunne et al.*, 2007; *Siegel et al.*, 2014] to evaluate carbon flux from the biological pump, neglecting the importance of spatially-variable physical mixing. Estimates of the strength of the biological pump that are relevant to exchange of carbon between the atmosphere, surface ocean, and deep ocean reservoirs need to instead use the winter ventilation depth criterion. In addition, the influence of biological carbon export on ocean absorption of atmospheric CO_2 depends not only on the annual flux of organic carbon exported below the winter ventilation depth, but also on the timing of NCP flux from the mixed layer and ventilation of remineralized organic matter back to the mixed layer throughout the year.

The discrepancy between productivity estimates in the Kuroshio region and previous estimates from time-series stations [*Palevsky et al.*, 2016] as well as discrepancies between the geochemical-based estimates and estimates from satellite-based algorithms and a global biogeochemical model [*Palevsky et al.*, in prep] demonstrate that productivity rates in the ocean remain undersampled. This is particularly the case in the high latitude ocean where fall and winter sampling is more challenging and in physically dynamic regions such as the Kuroshio where measurements at a single time-series station cannot represent productivity rates

throughout a large area. The lack of observational estimates in wintertime high latitude conditions (i.e. outside the tropics and subtropics) presents a challenge for the development and validation of globally-applicable algorithms and models, and for expanding our mechanistic understanding of the role of wintertime processes in the ocean carbon cycle.

Sampling to increase the global footprint of observational coverage, temporal resolution over the full annual cycle, and process-based understanding of the mechanisms driving the biological pump requires a combination of observational approaches. Broad basin-scale coverage can be achieved from surface sampling on ships of opportunity [e.g. *Juranek and Quay*, 2010; *Ostle et al.*, 2014; *Munro et al.*, 2015; *Palevsky et al.*, 2016] as well as new arrays of profiling floats equipped with chemical sensors for dissolved oxygen, nitrate and carbonate system parameters [e.g. *Emerson and Bushinsky*, 2014; *Bushinsky and Emerson*, 2015; *Williams et al.*, 2016]. These are complementary approaches, as ship-based sampling allows for measurements not possible with autonomous sensors (i.e. TOI, O_2/Ar, DIC), but floats provide measurements throughout the water column not possible from ships of opportunity. Observations at individual time-series sampling locations with moorings to provide high temporal-resolution autonomous measurements [e.g. *Körtzinger et al.*, 2008; *Fassbender et al.*, 2016] enable more precise estimates of the timing as well as the annual rate of NCP. Extending these observational platforms to include measurements throughout the water column will further enhance our ability to quantify fluxes from both the mixed layer and winter ventilation depth throughout the year. Finally, ship-based process studies provide the opportunity to include additional measurements of ecosystem processes throughout the water column to further develop mechanistic understanding of the controls on seasonal export and remineralization rates [e.g. *Siegel et al.*,

2016], but need to be integrated with year-round observations to determine the ultimate fate of seasonally-exported material.

The analytical approach used to estimate GPP and NCP in Chapter 2 advances the utility of triple oxygen isotopes (TOI) and dissolved O_2/Ar ratios as a component of this overall observational effort. Interpreting the TOI and O_2/Ar measurements as non-incubation-based productivity tracers throughout the full annual cycle, including during seasons with vigorous physical advection and mixing, required the development of methods to account for physical as well as biological influences on the tracers. We introduced a novel approach to estimate annual NCP to the winter ventilation depth based on measured surface ocean O_2/Ar that can be applied even in regions of strong advection such as the Kuroshio (equation 8 in Chapter 2) and demonstrate that a simple approach to estimating annual GPP from annual air-sea TOI flux effectively determines GPP through the full euphotic zone. These advances in the utility of TOI and O_2/Ar as non-incubation based tracers of GPP and NCP are globally applicable, and present the opportunity for similar analyses in other ocean regions to extend our baseline understanding of the current rates and efficiency of the biological pump.

Even as observational analyses expand in scope, satellite-based primary and export production algorithms and global biogeochemical models remain vital tools for studying the biological pump at a global scale. Global biogeochemical models already are able to provide depth-resolved export rates and efficiency, as discussed in Chapter 3, but these variables are often archived only at a standard global depth in large scale model intercomparison projects. Adding common output variables needed to estimate depth-resolved export in future model intercomparison projects would greatly improve the ability to evaluate model simulations of the biological pump for both current and future conditions. Satellite-based estimates of export to the

winter ventilation depth are more challenging because remote sensing observations only measure surface ocean properties, but new efforts to improve mechanistic models of the fate of primary production provide a promising step forward [e.g. *Siegel et al.*, 2014, 2016]. New satellite-based algorithms should consider the influence of physical processes of winter mixing as well as ecosystem properties on annual export efficiency. In both cases, development of new algorithms and models will benefit from observational data to identify key mechanisms and provide calibration data to improve our global-scale estimates of export production and ability to evaluate its current and future role in the global carbon cycle.

BIBLIOGRAPHY

Anderson, L. A., and J. L. Sarmiento (1994), Redfield ratios of remineralization determined by nutrient data analysis, *Glob. Biogeochem. Cycles*, *8*(1), 65–80.

Andreev, A., M. Kusakabe, M. Honda, A. Murata, and C. Saito (2002), Vertical fluxes of nutrients and carbon through the halocline in the western subarctic Gyre calculated by mass balance, *Deep Sea Res., Part II*, *49*, 5577–5593, doi:10.1016/S0967-0645(02)00200-X.

Armstrong, R. A., C. Lee, J. I. Hedges, S. Honjo, and S. G. Wakeham (2002), A new, mechanistic model for organic carbon fluxes in the ocean based on the quantitative association of POC with ballast minerals, *Deep Sea Res., Part II*, *49*, 219–236.

Ayers, J. M., and M. S. Lozier (2010), Physical controls on the seasonal migration of the North Pacific transition zone chlorophyll front, *J. Geophys. Res.*, *115*, C05001, doi:10.1029/2009JC005596.

Ayers, J. M., and M. S. Lozier (2012), Unraveling dynamical controls on the North Pacific carbon sink, *J. Geophys. Res.*, *117*, C01017, doi:10.1029/2011JC007368.

Bates, R. N., Y. M. Astor, M. J. Church, K. Currie, J. E. Dore, M. Gonzalez-Davila, L. Lorenzoni, F. Muller-Karger, J. Olafsson, and J. M. Santana-Casiano (2014), A Time-Series View of Changing Surface Ocean Chemistry Due to Ocean Uptake of Anthropogenic CO_2 and Ocean Acidification, *Oceanography*, *27*(1), 126–141, doi:10.5670/oceanog.2014.16.

Behrenfeld, M. J. (2005), Carbon-based ocean productivity and phytoplankton physiology from space, *Global Biogeochem. Cycles*, *19*(1), 1–14, doi:10.1029/2004GB002299.

Behrenfeld, M. J., and P. G. Falkowski (1997), Photosynthetic rates derived from satellite-based chlorophyll concentration, *Limnol. Oceanogr.*, *42*(1), 1–20.

Behrenfeld, M. J. et al. (2009), Satellite-detected fluorescence reveals global physiology of ocean phytoplankton, *Biogeosciences*, *6*, 779–794, doi:10.5194/bgd-5-4235-2008.

Behrenfeld, M. J., R. T. O'Malley, E. S. Boss, T. K. Westberry, J. R. Graff, K. H. Halsey, A. J. Milligan, D. A. Siegel, and M. B. Brown (2015), Revaluating ocean warming impacts on global phytoplankton, *Nat. Clim. Chang.*, doi:10.1038/nclimate2838.

Bender, M. et al. (1987), A comparison of four methods for determining planktonic community production, *Limnol. Ocean.*, *32*(5), 1085–1098.

Bender, M., J. Orchardo, M.-L. Dickson, R. Barber, and S. Lindley (1999), In vitro O_2 fluxes compared with 14C production and other rate terms during the JGOFS Equatorial Pacific experiment, *Deep Sea Res., Part I*, *46*, 637–654, doi:10.1016/S0967-0637(98)00080-6.

Bograd, S. J., D. G. Foley, F. B. Schwing, C. Wilson, R. M. Laurs, J. J. Polovina, E. A. Howell, and R. E. Brainard (2004), On the seasonal and interannual migrations of the transition zone chlorophyll front, *Geophys. Res. Lett.*, *31*, L17204, doi:10.1029/2004GL020637.

Bopp, L. et al. (2013), Multiple stressors of ocean ecosystems in the 21st century: projections with CMIP5 models, *Biogeosciences*, *10*, 6225–6245, doi:10.5194/bg-10-6225-2013.

Boyd, P., and P. J. Harrison (1999), Phytoplankton dynamics in the NE subarctic Pacific, *Deep*

Sea Res., Part II, *46*, 2405–2432, doi:10.1016/S0967-0645(99)00069-7.

Brainerd, K. E., and M. C. Gregg (1993), Diurnal restratification and turbulence in the oceanic surface mixed layer: 1. Observations, *J. Geophys. Res.*, *98*(C12), 22645–22656, doi:10.1029/93JC02298.

Bushinsky, S. M., and S. Emerson (2015), Marine biological production from in situ oxygen measurements on a profiling float in the subarctic Pacific Ocean, *Glob. Biogeochem. Cycles*, *29*, doi:10.1002/2015GB005251.

Carr, M.-E. et al. (2006), A comparison of global estimates of marine primary production from ocean color, *Deep Sea Res., Part I*, *53*, 741–770, doi:10.1016/j.dsr2.2006.01.028.

Charette, M. A., S. B. Moran, and J. K. B. Bishop (1999), ^{234}Th as a tracer of particulate organic carbon export in the subarctic northeast Pacific Ocean, *Deep Sea Res., Part II*, *46*, 2833–2861, doi:10.1016/S0967-0645(99)00085-5.

Chierici, M., A. Fransson, and Y. Nojiri (2006), Biogeochemical processes as drivers of surface fCO_2 in contrasting provinces in the subarctic North Pacific Ocean, *Glob. Biogeochem. Cycles*, *20*, GB1009, doi:10.1029/2004GB002356.

Church, M. J., M. W. Lomas, and F. Muller-Karger (2013), Sea change: Charting the course for biogeochemical ocean time-series research in a new millennium, *Deep Sea Res., Part II*, *93*, 2–15, doi:10.1016/j.dsr2.2013.01.035.

Ciais, P. et al. (2013), Carbon and Other Biogeochemical Cycles, in *Climate Change 2013 - The Physical Science Basis*, edited by Stocker, T.F., D. Qin, G.-K. Plattner, M. Tignor, S.K. Allen, J. Boschung, A. Nauels, Y. Xia, V. Bex and P.M. Midgley, pp. 465–570, Cambridge University Press, Cambridge, United Kingdom and New York, NY, USA.

Craig, H., and T. Hayward (1987), Oxygen supersaturation in the ocean: Biological versus physical contributions, *Science.*, *235*, 199–202.

Cronin, M. F., N. A. Bond, J. Thomas Farrar, H. Ichikawa, S. R. Jayne, Y. Kawai, M. Konda, B. Qiu, L. Rainville, and H. Tomita (2013), Formation and erosion of the seasonal thermocline in the Kuroshio Extension Recirculation Gyre, *Deep Sea Res., Part II*, *85*, 62–74, doi:10.1016/j.dsr2.2012.07.018.

Demnan, K. L., and A. E. Gargett (1983), Time and space scales of vertical mixing and advection of phytoplankton in the upper ocean, *Limnol. Oceanogr.*, *28*(5), 801–815, doi:10.4319/lo.1983.28.5.0801.

DeVries, T., F. Primeau, and C. Deutsch (2012), The sequestration efficiency of the biological pump, *Geophys. Res. Lett.*, *39*, L13601, doi:10.1029/2012GL051963.

Dickson, A. G., and F. J. Millero (1987), A comparison of the equilibrium constants for the dissociation of carbonic acid in seawater media, *Deep Sea Res.*, *34*(10), 1733–1743, doi:10.1016/0198-0149(87)90021-5.

Dickson, A. G., C. L. Sabine, and J. R. Christian (2007), Guide to best practices for ocean CO_2 measurements., *PICES Spec. Publ.*, *3*, 191 pp., North Pacific Marine Sciences Organization. Sidney, B.C., Canada.

Doney, S. C., V. J. Fabry, R. A. Feely, and J. A. Kleypas (2009a), Ocean Acidification: The

Other CO_2 Problem, *Ann. Rev. Mar. Sci.*, *1*(1), 169–192, doi:10.1146/annurev.marine.010908.163834.

Doney, S. C., I. Lima, J. K. Moore, K. Lindsay, M. J. Behrenfeld, T. K. Westberry, N. Mahowald, D. M. Glover, and T. Takahashi (2009b), Skill metrics for confronting global upper ocean ecosystem-biogeochemistry models against field and remote sensing data, *J. Mar. Syst.*, *76*(1-2), 95–112, doi:10.1016/j.jmarsys.2008.05.015.

Duce, R. A., and N. W. Tindale (1991), Chemistry and biology of iron and other trace metals in the ocean, *Limnol. Oceanogr.*, *36*(8), 1715–1726, doi:10.4319/lo.1991.36.8.1715.

Dugdale, R. C., and J. J. Goering (1967), Uptake of new and regenerated forms of nitrogen in primary productivity, *Limnol. Oceanogr.*, *12*(2), 196–206, doi:10.4319/lo.1967.12.2.0196.

Dunne, J. P., R. A. Armstrong, A. Gnanadesikan, and J. L. Sarmiento (2005), Empirical and mechanistic models for the particle export ratio, *Glob. Biogeochem. Cycles*, *19*, doi:10.1029/2004GB002390.

Dunne, J. P., J. L. Sarmiento, and A. Gnanadesikan (2007), A synthesis of global particle export from the surface ocean and cycling through the ocean interior and on the seafloor, *Glob. Biogeochem. Cycles*, *21*(4), doi:10.1029/2006GB002907.

Elskens, M., N. Brion, K. Buesseler, B. A. S. Van Mooy, P. Boyd, F. Dehairs, N. Savoye, and W. Baeyens (2008), Primary, new and export production in the NW Pacific subarctic gyre during the vertigo K2 experiments, *Deep Sea Res., Part II*, *55*, 1594–1604, doi:10.1016/j.dsr2.2008.04.013.

Emerson, S. (1987), Seasonal oxygen cycles and biological new production in surface waters of the subarctic Pacific Ocean, *J. Geophys. Res.*, *92*(C6), 6535–6544.

Emerson, S. (2014), Annual Net Community Production and the Biological Carbon Flux in the Ocean, *Global Biogeochem. Cycles*, *28*, doi:10.1002/2013GB004680.

Emerson, S., and S. Bushinsky (2014), Oxygen Concentrations and Biological Fluxes in the Open Ocean, *Oceanography*, *27*(1), 168–171, doi:10.5670/oceanog.2014.20.

Emerson, S., and C. Stump (2010), Net biological oxygen production in the ocean—II: Remote in situ measurements of O_2 and N_2 in subarctic pacific surface waters, *Deep Sea Res., Part I*, *57*, 1255–1265, doi:10.1016/j.dsr.2010.06.001.

Emerson, S., P. Quay, C. Stump, D. Wilbur, and M. Knox (1991), O_2, Ar, N_2 and ^{222}Rn in surface waters of the subarctic ocean: net biological O2 production, *Glob. Biogeochem. Cycles*, *5*(1), 49–69.

Emerson, S., C. Stump, D. Wilbur, and P. Quay (1999), Accurate measurement of Oxygen, Nitrogen and Argon gases in water and the solubility of Nitrogen, *Mar. Chem.*, *64*, 337–347, doi:10.1016/S0304-4203(98)00090-5.

Emerson, S. R., and J. I. Hedges (2008), *Chemical Oceanography and the Marine Carbon Cycle*, Cambridge University Press, New York, USA.

Fassbender, A. (2014), New approaches to study the marine carbon cycle, PhD thesis, University of Washington, Seattle, Washington, USA.

Fassbender, A. J., C. L. Sabine, and M. F. Cronin (2016), Net community production and

calcification from 7 years of NOAA Station Papa Mooring measurements, *Glob. Biogeochem. Cycles*, *30*, doi:10.1002/2015GB005205.

Feely, R. A., R. Wanninkhof, H. B. Milburn, C. E. Cosca, M. Stapp, and P. P. Murphy (1998), A new automated underway system for making high precision pCO_2 measurements onboard research ships, *Anal. Chim. Acta*, *377*, 185–191.

Field, C. B., M. J. Behrenfeld, J. T. Randerson, and P. Falkowski (1998), Primary Production of the Biosphere: Integrating Terrestrial and Oceanic Components, *Science*, *281*(5374), 237–240, doi:10.1126/science.281.5374.237.

Francois, R. (2002), Factors controlling the flux of organic carbon to the bathypelagic zone of the ocean, *Global Biogeochem. Cycles*, *16*(4), 1087, doi:10.1029/2001GB001722.

Friedrichs, M. A. M. et al. (2009), Assessing the uncertainties of model estimates of primary productivity in the tropical Pacific Ocean, *J. Mar. Syst.*, *76*(1-2), 113–133, doi:10.1016/j.jmarsys.2008.05.010.

Fujiki, T., K. Matsumoto, S. Watanabe, T. Hosaka, and T. Saino (2011), Phytoplankton productivity in the western subarctic gyre of the North Pacific in early summer 2006, *J. Oceanogr.*, *67*, 295–303, doi:10.1007/s10872-011-0028-1.

Garcia, H. E., and L. I. Gordon (1992), Oxygen solubility in seawater: Better fitting solubility equations, *Limnol. Ocean.*, *37*(6), 1307–1312.

Giesbrecht, K. E., R. C. Hamme, and S. R. Emerson (2012), Biological productivity along Line P in the subarctic northeast Pacific: In situ versus incubation-based methods, *Global Biogeochem. Cycles*, *26*, GB3028, doi:10.1029/2012GB004349.

Halsey, K. H., and B. M. Jones (2015), Phytoplankton Strategies for Photosynthetic Energy Allocation., *Ann. Rev. Mar. Sci.*, *7*, 265–297, doi:10.1146/annurev-marine-010814-015813.

Hamme, R., and S. Emerson (2004), The solubility of neon, nitrogen and argon in distilled water and seawater, *Deep Sea Res., Part I*, *51*(11), 1517–1528, doi:10.1016/j.dsr.2004.06.009.

Hamme, R. C. et al. (2012), Dissolved O_2/Ar and other methods reveal rapid changes in productivity during a Lagrangian experiment in the Southern Ocean, *J. Geophys. Res.*, *117*, C00F12, doi:10.1029/2011JC007046.

Hansell, D. A., and C. A. Carlson (1998), Net community production of dissolved organic carbon, *Glob. Biogeochem. Cycles*, *12*(3), 443–453, doi:doi:10.1029/98GB01928.

Harrison, P., P. Boyd, D. Varela, S. Takeda, A. Shiomoto, and T. Odate (1999), Comparison of factors controlling phytoplankton productivity in the NE and NW subarctic Pacific gyres, *Prog. Ocean.*, *43*(2-4), 205–234.

Harrison, P., F. Whitney, A. Tsuda, H. Saito, and K. Tadokoro (2004a), Nutrient and plankton dynamics in the NE and NW gyres of the subarctic Pacific Ocean, *J. Ocean.*, *60*, 93–117.

Harrison, P. J., F. A. Whitney, A. Tsuda, H. Saito, and K. Tadokoro (2004b), Nutrient and Plankton Dynamics in the NE and NW Gyres of the Subarctic Pacific Ocean, *J. Ocean.*, *60*, 93–117, doi:10.1023/B:JOCE.0000038321.57391.2a.

Hauck, J. et al. (2015), On the Southern Ocean CO_2 uptake and the role of the biological carbon pump in the 21st century, *Glob. Biogeochem. Cycles*, *29*, 1451–1470,

doi:10.1002/2015GB005140.

Henson, S. A., R. Sanders, E. Madsen, P. J. Morris, F. Le Moigne, and G. D. Quartly (2011), A reduced estimate of the strength of the ocean's biological carbon pump, *Geophys. Res. Lett.*, *38*(4), 10–14, doi:10.1029/2011GL046735.

Henson, S. A., C. Beaulieu, and R. Lampitt (2016), Observing climate change trends in ocean biogeochemistry: when and where., *Glob. Chang. Biol.*, doi:10.1111/gcb.13152.

Heuven, S. van, D. Pierrot, E. L. J.W.B. Rae, and D. W. R. Wallace (2011), MATLAB Program Developed for CO2 System Calculations, , doi:10.3334/CDIAC/otg.CO2SYS_MATLAB_v1.1.

Honda, M. C. (2003), Biological pump in northwestern North Pacific, *J. Oceanogr.*, *59*, 671–684, doi:10.1023/B:JOCE.0000009596.57705.0c.

Honda, M. C. et al. (2015), Comparison of sinking particles in the upper 200 m between subarctic station K2 and subtropical station S1 based on drifting sediment trap experiments, *J. Oceanogr.*, doi:10.1007/s10872-015-0280-x.

Howard, E., S. Emerson, S. Bushinsky, and C. Stump (2010), The role of net community production in air-sea carbon fluxes at the North Pacific subarctic-subtropical boundary region, *Limnol. Oceanogr.*, *55*(6), 2585–2596, doi:10.4319/lo.2010.55.6.2585.

Imai, K., Y. Nojiri, N. Tsurushima, and T. Saino (2002), Time series of seasonal variation of primary productivity at station KNOT (44°N, 155°E) in the sub-arctic western North Pacific, *Deep Sea Res., Part II*, *49*, 5395–5408.

Isada, T., A. Hattori-Saito, H. Saito, T. Ikeda, and K. Suzuki (2010), Primary productivity and its bio-optical modeling in the Oyashio region, NW Pacific during the spring bloom 2007, *Deep Sea Res., Part II*, *57*, 1653–1664, doi:10.1016/j.dsr2.2010.03.009.

Jayne, S. R. et al. (2009), The Kuroshio Extension and its recirculation gyres, *Deep Sea Res., Part I*, *56*, 2088–2099, doi:10.1016/j.dsr.2009.08.006.

Jin, X., N. Gruber, J. P. Dunne, J. L. Sarmiento, and R. A. Armstrong (2006), Diagnosing the contribution of phytoplankton functional groups to the production and export of particulate organic carbon, $CaCO_3$, and opal from global nutrient and alkalinity distributions, *Global Biogeochem. Cycles*, *20*, GB2015, doi:10.1029/2005GB002532.

Jonsson, B. F., S. C. Doney, J. Dunne, and M. Bender (2013), Evaluation of the Southern Ocean O_2/Ar-based NCP estimates in a model framework, *J. Geophys. Res. Biogeosciences*, *118*, 385–399, doi:10.1002/jgrg.20032.

Juranek, L., and P. Quay (2010), Basin-wide photosynthetic production rates in the subtropical and tropical Pacific Ocean determined from dissolved oxygen isotope ratio measurements, *Global Biogeochem. Cycles*, *24*, GB2006, doi:10.1029/2009GB003492.

Juranek, L. W., and P. D. Quay (2013), Using triple isotopes of dissolved oxygen to evaluate global marine productivity, *Annu. Rev. Mar. Sci.*, *5*, 503–24, doi:10.1146/annurev-marine-121211-172430.

Juranek, L. W., R. C. Hamme, J. Kaiser, R. Wanninkhof, and P. D. Quay (2010), Evidence of O_2 consumption in underway seawater lines: Implications for air-sea O_2 and CO_2 fluxes,

Geophys. Res. Lett., *37*, L01601, doi:10.1029/2009GL040423.

Juranek, L. W., P. D. Quay, R. A. Feely, D. Lockwood, D. M. Karl, and M. J. Church (2012), Biological production in the NE Pacific and its influence on air-sea CO_2 flux: Evidence from dissolved oxygen isotopes and O 2 /Ar, *J. Geophys. Res.*, *117*, C05022, doi:10.1029/2011JC007450.

Kaiser, J. (2011), Technical note: Consistent calculation of aquatic gross production from oxygen triple isotope measurements, *Biogeosciences*, *8*, 1793–1811, doi:10.5194/bg-8-1793-2011.

Karl, D. M., J. R. Christian, J. E. Dore, D. V. Hebel, R. M. Letelier, L. M. Tupas, and C. D. Winn (1996), Seasonal and interannual variability in primary production and particle flux at Station ALOHA, *Deep Sea Res., Part II*, *43*(2-3), 539–568, doi:10.1016/0967-0645(96)00002-1.

Kawakami, H., and M. C. Honda (2007), Time-series observation of POC fluxes estimated from ^{234}Th in the northwestern North Pacific, *Deep Sea Res., Part I*, *54*, 1070–1090, doi:10.1016/j.dsr.2007.04.005.

Kawakami, H., Y. L. Yang, M. C. Honda, and M. Kusakabe (2004), Particulate organic carbon fluxes estimated from Th-234 deficiency in winters and springs in the northwestern North Pacific, *Geochem. J.*, *38*, 581–592.

Kawakami, H., M. C. Honda, M. Wakita, and S. Watanabe (2007), Time-series observation of dissolved inorganic carbon and nutrients in the northwestern North Pacific, *J. Oceanogr.*, *63*, 967–982, doi:10.1007/s10872-007-0081-y.

Kawakami, H., M. C. Honda, K. Matsumoto, T. Fujiki, and S. Watanabe (2010a), East – West Distribution of POC Fluxes Estimated from ^{234}Th in the Northern North Pacific in Autumn, *J. Ocean.*, *66*, 71–83.

Kawakami, H., M. C. Honda, K. Matsumoto, T. Fujiki, and S. Watanabe (2010b), East-West Distribution of Nutrients and Dissolved Inorganic Carbon in the Northern North Pacific in Autumn, *Open Ocean. J.*, *4*, 99–106.

Klaas, C., and D. E. Archer (2002), Association of sinking organic matter with various types of mineral ballast in the deep sea: Implications for the rain ratio, *Global Biogeochem. Cycles*, *16*(4), 1116, doi:10.1029/2001GB001765.

Körtzinger, A., U. Send, R. S. Lampitt, S. Hartman, D. W. R. Wallace, J. Karstensen, M. G. Villagarcia, O. Llinás, and M. D. DeGrandpre (2008), The seasonal pCO_2 cycle at 49°N/16.5°W in the northeastern Atlantic Ocean and what it tells us about biological productivity, *J. Geophys. Res.*, *113*, C04020, doi:10.1029/2007JC004347.

Lämmerzahl, P. (2002), Oxygen isotope composition of stratospheric carbon dioxide, *Geophys. Res. Lett.*, *29*(12), 1582, doi:10.1029/2001GL014343.

Landschützer, P., N. Gruber, D. C. E. Bakker, and U. Schuster (2014), Recent variability of the global ocean carbon sink, *Glob. Biogeochem. Cycles*, *28*, 927–949, doi:10.1002/2014GB004853.

Laufkötter, C., M. Vogt, and N. Gruber (2013), Long-term trends in ocean plankton production and particle export between 1960-2006, *Biogeosciences*, *10*(11), 7373–7393,

doi:10.5194/bg-10-7373-2013.

Laufkötter, C., M. Vogt, N. Gruber, L. Bopp, J. Dunne, J. Hauck, J. John, I. Lima, R. Seferian, and C. Volker (2015), Projected decreases in future marine export production: the role of the carbon flux through the upper ocean ecosystem, *Biogeosci. Discuss.*, *12*(4), 3731–3824, doi:doi:10.5194/bgd-12-3731-2015.

Laws, E., P. Falkowski, W. J. Smith, H. Ducklow, and J. McCarthy (2000), Temperature effects on export production in the open ocean, *Glob. Biogeochem. Cycles*, *14*(4), 1231–1246.

Laws, E. A. (1991), Photosynthetic quotients, new production and net community production in the open ocean, *Deep Sea Res.*, *38*(1), 143–167.

Laws, E. A., E. D'Sa, and P. Naik (2011), Simple equations to estimate ratios of new or export production to total production from satellite-derived estimates of sea surface temperature and primary production, *Limnol. Ocean. Methods*, *9*, 593–601, doi:10.4319/lom.2011.9.593.

Liss, P. S., and L. Merlivat (1986), Air-sea gas exchange rates: Introduction and synthesis, in *The Role of Air-Sea Exchange in Geochemical Cycling*, edited by P. Buat-Menard, pp. 113–127, D. Reidel, Hingham, Massachusetts, USA.

Lockwood, D., P. D. Quay, M. T. Kavanaugh, L. W. Juranek, and R. A. Feely (2012), High-resolution estimates of net community production and air-sea CO_2 flux in the northeast Pacific, *Global Biogeochem. Cycles*, *26*, GB4010, doi:10.1029/2012GB004380.

Lockwood, D. E. (2013), Impact of the marine biological pump on atmospheric CO_2 uptake in the North Pacific: a study based on basin-wide underway measurements of oxygen/argon gas ratios and pCO2, PhD thesis, University of Washington, Seattle, Washington, USA.

Luz, B., and E. Barkan (2000), Assessment of Oceanic Productivity with the Triple-Isotope Composition of Dissolved Oxygen, *Science*, *288*, 2028–2031, doi:10.1126/science.288.5473.2028.

Luz, B., and E. Barkan (2005), The isotopic ratios $^{17}O/^{16}O$ and $^{18}O/^{16}O$ in molecular oxygen and their significance in biogeochemistry, *Geochim. Cosmochim. Acta*, *69*(5), 1099–1110, doi:10.1016/j.gca.2004.09.001.

Luz, B., and E. Barkan (2009), Net and gross oxygen production from O_2/Ar, $^{17}O/^{16}O$ and $^{18}O/^{16}O$ ratios, *Aquat. Microb. Ecol.*, *56*, 133–145, doi:10.3354/ame01296.

Marra, J. (2002), Approaches to the measurement of plankton production, in *Productivity and Carbon Assimilation in Marine and Freshwater Ecosystems*, edited by P. J. Williams, D. R. Thomas, and C. S. Reynolds, pp. 78–108, Blackwell, London, United Kingdom.

Matsumoto, K., O. Abe, T. Fujiki, C. Sukigara, and Y. Mino (2016), Primary productivity at the time-series stations in the northwestern Pacific Ocean: is the subtropical station unproductive?, *J. Oceanogr.*, doi:10.1007/s10872-016-0354-4.

McKinley, G. A. et al. (2006), North Pacific carbon cycle response to climate variability on seasonal to decadal timescales, *J. Geophys. Res.*, *111*, C07S06, doi:10.1029/2005JC003173.

McKinley, G. A., D. J. Pilcher, A. R. Fay, K. Lindsay, M. C. Long, and N. S. Lovenduski (2016), Timescales for detection of trends in the ocean carbon sink, *Nature*, *530*, 469–472, doi:10.1038/nature16958.

Mehrbach, C., C. H. Cuberson, J. E. Hawley, and R. M. Pytkowicz (1973), Measurement of the apparent dissociation constants of carbonic acid in seawater at atmospheric pressure, *Limnol. Oceanogr.*, *18*, 897–907, doi:10.4319/lo.1973.18.6.0897.

Midorikawa, T., T. Umeda, N. Hiraishi, K. Ogawa, K. Nemoto, N. Kubo, and M. Ishii (2002), Estimation of seasonal net community production and air-sea CO_2 flux based on the carbon budget above the temperature minimum layer in the western subarctic North Pacific, *Deep Sea Res., Part I*, *49*, 339–362, doi:10.1016/S0967-0637(01)00054-1.

Midorikawa, T., K. Ogawa, K. Nemoto, H. Kamiya, T. Umeda, N. Hiraishi, A. Wada, and M. Ishii (2003), Interannual variations of net community production and air-sea CO_2 flux from winter to spring in the western subarctic North Pacific, *Tellus*, *55B*, 466–477, doi:10.1034/j.1600-0889.2003.00009.x.

Monterey, G., and S. Levitus (1997), Seasonal Variability of the Mixed Layer Depth for the World Ocean, *NOAA Atlas NESDIS*, *14*(5), 96pp.

Moore, J. K., S. C. Doney, J. A. Kleypas, D. M. Glover, and I. Y. Fung (2002), An intermediate complexity marine ecosystem model for the global domain, *Deep Sea Res., Part II*, *49*, 403–462, doi:10.1016/S0967-0645(01)00108-4.

Moore, J. K., S. C. Doney, and K. Lindsay (2004), Upper ocean ecosystem dynamics and iron cycling in a global three-dimensional model, *Global Biogeochem. Cycles*, *18*(4), 1–21, doi:10.1029/2004GB002220.

Moore, J. K., K. Lindsay, S. C. Doney, M. C. Long, and K. Misumi (2013), Marine ecosystem dynamics and biogeochemical cycling in the community earth system model [CESM1(BGC)]: Comparison of the 1990s with the 2090s under the RCP4.5 and RCP8.5 scenarios, *J. Clim.*, *26*(23), 9291–9312, doi:10.1175/JCLI-D-12-00566.1.

Munro, D. R., N. S. Lovenduski, B. B. Stephens, T. Newberger, K. R. Arrigo, T. Takahashi, P. D. Quay, J. Sprintall, N. Freeman, and C. Sweeney (2015), Estimates of net community production in the Southern Ocean determined from time series observations (2002–2011) of nutrients, dissolved inorganic carbon, and surface ocean pCO_2 in Drake Passage, *Deep Sea Res., Part II*, *114*, 49–63, doi:10.1016/j.dsr2.2014.12.014.

Nicholson, D., R. H. R. Stanley, and S. C. Doney (2014), The triple oxygen isotope tracer of primary productivity in a dynamic ocean model, *Global Biogeochem. Cycles*, *28*, 538–552, doi:10.1002/2013GB004704.

Nicholson, D. P., R. H. R. Stanley, E. Barkan, D. M. Karl, B. Luz, P. D. Quay, and S. C. Doney (2012), Evaluating triple oxygen isotope estimates of gross primary production at the Hawaii Ocean Time-series and Bermuda Atlantic Time-series Study sites, *J. Geophys. Res.*, *117*, C05012, doi:10.1029/2010JC006856.

Nicholson, D. P., S. T. Wilson, S. C. Doney, and D. M. Karl (2015), Quantifying subtropical North Pacific gyre mixed layer primary productivity from Seaglider observations of diel oxygen cycles, *Geophys. Res. Lett.*, doi:10.1002/2015GL063065.

Nightingale, P. D., G. Malin, C. S. Law, A. J. Watson, P. S. Liss, M. I. Liddicoat, J. Boutin, and R. C. Upstill-Goddard (2000), In situ evaluation of air-sea gas exchange parameterizations using novel conservative and volatile tracers, *Glob. Biogeochem. Cycles*, *14*(1), 373–387.

Ohno, Y., N. Iwasaka, F. Kobashi, and Y. Sato (2009), Mixed Layer Depth Climatology of the North Pacific, *J. Ocean.*, *65*, 1–16.

Ostle, C., M. Johnson, P. Landschützer, U. Schuster, S. Hartman, and C. Robinson (2014), Net Community Production in the North Atlantic Ocean derived from Volunteer Observing Ship data, *Global Biogeochem. Cycles*, *29*, doi:10.1002/2014GB004868.

Palevsky, H. I., F. Ribalet, J. E. Swalwell, C. E. Cosca, E. D. Cokelet, R. A. Feely, E. V. Armbrust, and P. D. Quay (2013), The influence of net community production and phytoplankton community structure on CO_2 uptake in the Gulf of Alaska, *Global Biogeochem. Cycles*, *27*, doi:10.1002/gbc.20058.

Palevsky, H. I., P. D. Quay, D. E. Lockwood, and D. P. Nicholson (2016), The annual cycle of gross primary production, net community production, and export efficiency across the North Pacific Ocean, *Glob. Biogeochem. Cycles*, *30*, doi:10.1002/2015GB005318.

Palevsky, H. I., P. D. Quay, and D. P. Nicholson (submitted manuscript), Discrepant estimates of primary and export production from satellite algorithms, a biogeochemical model and geochemical tracer measurements in the North Pacific Ocean.

Passow, U., and C. Carlson (2012), The biological pump in a high CO_2 world, *Mar. Ecol. Prog. Ser.*, *470*(2), 249–271, doi:10.3354/meps09985.

Pierrot, D., C. Neill, K. Sullivan, R. Castle, R. Wanninkhof, H. Luger, T. Johannessen, A. Olsen, R. A. Feely, and C. E. Cosca (2009), Recommendations for autonomous underway pCO_2 measuring systems and data-reduction routines, *Deep Sea Res., Part II*, *56*(8-10), 512–522, doi:10.1016/j.dsr2.2008.12.005.

Polovina, J. J. J., E. Howell, D. R. D. R. Kobayashi, and M. P. M. P. Seki (2001), The transition zone chlorophyll front, a dynamic global feature defining migration and forage habitat for marine resources, *Prog. Oceanogr.*, *49*, 469–483, doi:10.1016/S0079-6611(01)00036-2.

Prokopenko, M. G., O. M. Pauluis, J. Granger, and L. Y. Yeung (2011), Exact evaluation of gross photosynthetic production from the oxygen triple-isotope composition of O_2: Implications for the net-to-gross primary production ratios, *Geophys. Res. Lett.*, *38*, L14603, doi:10.1029/2011GL047652.

Quay, P., and J. Stutsman (2003), Surface layer carbon budget for the subtropical N. Pacific: $\delta^{13}C$ constraints at station ALOHA, *Deep Sea Res., Part I*, *50*, 1045–1061, doi:10.1016/S0967-0637(03)00116-X.

Quay, P., J. Stutsman, and T. Steinhoff (2012), Primary production and carbon export rates across the subpolar N. Atlantic Ocean basin based on triple oxygen isotope and dissolved O_2 and Ar gas measurements, *Glob. Biogeochem. Cycles*, *26*, GB2003, doi:10.1029/2010GB004003.

Quay, P. D., C. Peacock, K. Björkman, and D. M. Karl (2010), Measuring primary production rates in the ocean: Enigmatic results between incubation and non-incubation methods at Station ALOHA, *Global Biogeochem. Cycles*, *24*, GB3014, doi:10.1029/2009GB003665.

Le Quéré, C. et al. (2015), Global Carbon Budget 2015, *Earth Syst. Sci. Data*, *7*, 349–396, doi:10.5194/essd-7-349-2015.

Redfield, A. C., B. H. Ketchum, and F. A. Richards (1963), The influence of organisms on the

composition of seawater, in *The sea, v.2*, edited by M. N. Hill, pp. 26–77, Interscience, New York, USA.

Reuer, M. K., B. A. Barnett, M. L. Bender, P. G. Falkowski, and M. B. Hendricks (2007), New estimates of Southern Ocean biological production rates from O_2/Ar ratios and the triple isotope composition of O_2, *Deep Sea Res., Part I*, *54*, 951–974, doi:10.1016/j.dsr.2007.02.007.

Roden, G. I. (1991), Subarctic-subtropical transition zone of the North Pacific: Large-scale aspects and mesoscale structure, *NOAA Tech. Rep. NMFS*, *105*, 1–38.

Roy, T., L. Bopp, M. Gehlen, B. Schneider, P. Cadule, T. L. Frölicher, J. Segschneider, J. Tjiputra, C. Heinze, and F. Joos (2011), Regional impacts of climate change and atmospheric CO_2 on future ocean carbon uptake: A multimodel linear feedback analysis, *J. Clim.*, *24*(9), 2300–2318, doi:10.1175/2010JCLI3787.1.

Saba, V. S. et al. (2011), An evaluation of ocean color model estimates of marine primary productivity in coastal and pelagic regions across the globe, *Biogeosciences*, *8*, 489–503, doi:10.5194/bg-8-489-2011.

Sabine, C. L., and T. Tanhua (2010), Estimation of Anthropogenic CO_2 Inventories in the Ocean, *Annu. Rev. Mar. Sci.*, *2*(1), 175–198, doi:10.1146/annurev-marine-120308-080947.

Sarmiento, J. L., and N. Gruber (2006), *Ocean Biogeochemical Dynamics*, Princeton Univ. Press, Princeton, N.J.

Sasai, Y., K. J. Richards, A. Ishida, and H. Sasaki (2010), Effects of cyclonic mesoscale eddies on the marine ecosystem in the Kuroshio Extension region using an eddy-resolving coupled physical-biological model, *Ocean Dyn.*, *60*, 693–704, doi:10.1007/s10236-010-0264-8.

Sasai, Y., C. Yoshikawa, S. L. Smith, T. Hashioka, K. Matsumoto, M. Wakita, K. Sasaoka, and M. C. Honda (2016), Coupled 1-D physical–biological model study of phytoplankton production at two contrasting time-series stations in the western North Pacific, *J. Oceanogr.*, doi:10.1007/s10872-015-0341-1.

Shiomoto, A. (2000), Efficiency of water-column light utilization in the subarctic northwestern Pacific, *Limnol. Oceanogr.*, *45*(4), 982–987, doi:10.4319/lo.2000.45.4.0982.

Siegel, D. A., K. O. Buesseler, S. C. Doney, S. F. Sailley, M. J. Behrenfeld, and P. W. Boyd (2014), Global assessment of ocean carbon export by combining satellite observations and food-web models, *Global Biogeochem. Cycles*, *28*, 181–196, doi:10.1002/2013GB004743.

Siegel, D. A. et al. (2016), Prediction of the Export and Fate of Global Ocean Net Primary Production: The EXPORTS Science Plan, *Front. Mar. Sci.*, *3*(22), doi:10.3389/fmars.2016.00022.

Smayda, T. J. (1970), The suspension and sinking of phytoplankton in the sea, *Ocean. Mar. Biol. Ann. Rev.*, *8*, 353–414.

Sonnerup, R. E., S. Mecking, and J. L. Bullister (2013), Transit time distributions and oxygen utilization rates in the Northeast Pacific Ocean from chlorofluorocarbons and sulfur hexafluoride, *Deep Sea Res., Part I*, *72*, 61–71, doi:10.1016/j.dsr.2012.10.013.

Stanley, R. H. R., J. B. Kirkpatrick, N. Cassar, B. A. Barnett, and M. L. Bender (2010), Net

community production and gross primary production rates in the western equatorial Pacific, *Glob. Biogeochem. Cycles*, *24*, GB4001, doi:10.1029/2009GB003651.

Steeman Nielsen, E. (1952), The use of radio-active carbon (C14) for measuring organic production in the sea, *J Cons Cons Int Explor Mer*, *18*, 117–140.

Stukel, M. R., M. Kahru, C. R. Benitez-Nelson, M. Decima, R. Goericke, M. R. Landry, and M. D. Ohman (2015), Using Lagrangian-based process studies to test satellite algorithms of vertical carbon flux in the eastern North Pacific Ocean, *J. Geophys. Res.*, *120*(3), 2370–2384, doi:10.1002/2014JC010516.Received.

Takahashi, T., J. Olafsson, J. G. Goddard, D. W. Chipman, and S. C. Sutherland (1993), Seasonal variation of CO_2 and nutrients in the high-latitude surface oceans: A comparative study, *Glob. Biogeochem. Cycles*, *7*(4), 843–878.

Takahashi, T. et al. (2002), Global sea-air CO2 flux based on climatological surface ocean pCO2, and seasonal biological and temperature effects, *Deep Sea Res., Part II*, *49*, 1601–1622.

Takahashi, T. et al. (2009), Climatological mean and decadal change in surface ocean pCO_2, and net sea-air CO_2 flux over the global oceans, *Deep Sea Res., Part II*, *56*, 554–577, doi:10.1016/j.dsr2.2008.12.009.

Taylor, K. E., R. J. Stouffer, and G. A. Meehl (2012), An overview of CMIP5 and the experiment design, *Bull. Am. Meteorol. Soc.*, *93*(4), 485–498, doi:10.1175/BAMS-D-11-00094.1.

Tsurushima, N., Y. Nojiri, K. Imai, and S. Watanabe (2002), Seasonal variations of carbon dioxide system and nutrients in the surface mixed layer at station KNOT (44°N, 155°E) in the subarctic western North Pacific, *Deep Sea Res., Part II*, *49*, 5377–5394, doi:10.1016/S0967-0645(02)00197-2.

Varela, D. E., and P. J. Harrison (1999), Seasonal variability in nitrogenous nutrition of phytoplankton assemblages in the northeastern subarctic Pacific Ocean, *Deep Sea Res., Part II*, *46*, 2505–2538, doi:10.1016/S0967-0645(99)00074-0.

Volk, T., and M. I. Hoffert (1985), Ocean Carbon Pumps: Analysis of relative strengths and efficiencies in ocean-driven atmospheric CO_2 changes, in *The Carbon Cycle and Atmospheric CO_2 Natural Variations Archean to Present*, vol. 32, edited by E. T. Sundquist and W. S. Broecker, pp. 99–110, American Geophysical Union, Wahington, D.C., USA.

VITA

Hilary Ilana Palevsky

EDUCATION:

Ph.D. Oceanography, University of Washington, June 2016
Thesis: "The North Pacific biological pump: Rates, efficiency and influence on ocean carbon uptake"
Graduate Certificate in Climate Science, June 2014

M.S. Oceanography, University of Washington, March 2012

B.A. Geology, *Summa cum laude*, Amherst College, May 2007

RESEARCH AND TEACHING POSITIONS:

Graduate Research Assistant, U. of Washington School of Oceanography, June 2010 – present
Advisers: Dr. Paul D. Quay and Dr. E. Virginia Armbrust

Visiting Member of the Faculty, The Evergreen State College, July – Sept. 2014
General Chemistry II with Laboratory

Teaching Assistant, U. of Washington School of Oceanography
Senior Thesis Capstone Sequence (OCEAN 443-445), Sept. 2012 – June 2013
Principles of Oceanography (OCEAN 200), Mar. – June 2012

Marine Science Shipboard Educator
Schooner Quinnipiack, Mar. – Oct. 2009
Schooner SoundWaters, Aug. – Nov. 2008

Thomas J. Watson Fellow, June 2007 – July 2008

Keck Geology Consortium Student Fellow, June 2006 – April 2007
Adviser: Dr. Anna M. Martini

ACADEMIC HONORS:

FELLOWSHIPS/SCHOLARSHIPS

Woods Hole Oceanographic Institution Postdoctoral Scholarship, 2016

National Science Foundation Graduate Research Fellowship (NSF GRFP), 2010 – 2015

National Defense Science and Engineering Graduate Fellowship (NDSEG), 2010 – 2013

Achievement Rewards for College Scientists Seattle Chapter Fellowship, 2010 – 2014

U. of Washington Program on Climate Change Fellowship (awarded but not used), Apr. 2010

Thomas J. Watson Fellowship, June 2007 – July 2008

AWARDS :

Mary Landsteiner Scholar Award, U. of Washington School of Oceanography, April 2016

U. of Washington College of the Environment Travel Award, Feb. 2016

Best Student Poster Award, SOLAS Summer School, Sept. 2013

Outstanding Student Presentation Award, TOS/ASLO/AGU Ocean Sciences Meeting, Feb. 2012

Phi Beta Kappa, April 2007

Walter F. Pond Prize, Amherst College Geology Department, April 2007

Belt-Brophy Prize, Amherst College Geology Department, April 2006

PUBLICATIONS:

Palevsky, H. I., P. D. Quay, D. E. Lockwood, and D. P. Nicholson (2016), The annual cycle of gross primary production, net community production and export efficiency across the North Pacific Ocean, Global Biogeochemical Cycles, 30, doi: 10.1002/2015GB005318.

Palevsky, H. I., F. Ribalet, J. E. Swalwell, C. E. Cosca, E. D. Cokelet, R. A. Feely, E. V. Armbrust, P. D. Quay (2013) The influence of net community production and phytoplankton community structure on CO_2 uptake in the Gulf of Alaska. Global Biogeochemical Cycles, 27, 664-676, doi: 10.1002/gbc.20058.

Gezelius, S. S., T. J. Hegland**, H. I. Palevsky**, J. Raakjær, (2008) "The Politics of Implementation in Resource Conservation: Comparing the EU/Denmark and Norway," in S.S. Gezelius, J. Raakjær (eds.), *Making Fisheries Management Work,* 207-229, Springer Science+Business Media B.V.

MANUSCRIPTS IN PREPARATION:

Palevsky, H. I. and P. D. Quay, Influence of the biological pump on CO_2 uptake over the annual cycle across the North Pacific Ocean, *in prep.*

Palevsky, H. I., P. D. Quay, and D. P. Nicholson, Primary production and carbon export rates across the North Pacific: Discrepant estimates from satellite algorithms, a biogeochemical model and tracer measurements from ships of opportunity, *submitted manuscript*.

CONFERENCE PRESENTATIONS:

Palevsky, H.I. and P. D. Quay (2016), Influence of the biological pump on carbon uptake over the annual cycle across the North Pacific Ocean. TOS/ASLO/AGU Ocean Sciences Meeting, New Orleans, LA, 21-26 February 2016. Oral presentation.

Palevsky, H.I., (2015) Ocean acidification data analysis in the chemistry classroom. American Association of Colleges and Universities STEM Conference, Seattle, WA, November 12-14 2015. Poster.

Palevsky, H. I., P. D. Quay, D. E. Lockwood, D. P. Nicholson (2015), Winter ventilation depth controls annual net community production and export efficiency across the North Pacific Ocean, Chemical Oceanography Gordon Research Seminar and Conference, Holderness, NH, July 25-31 2015. Poster.

Palevsky, H. I., P. D. Quay, D. E. Lockwood, D. P. Nicholson (2015), The annual cycle of gross primary production, net community production and export efficiency across the North Pacific Ocean, Ocean Carbon and Biogeochemistry Workshop, Woods Hole, MA, July 20-23 2015. Poster.

Palevsky, H.I., L. Neshyba, (2015) Ocean acidification data analysis in the chemistry classroom. University of Washington Teaching and Learning Symposium, Seattle, WA, April 14 2015. Poster.

Palevsky, H. I., D.E. Lockwood, E. J. Armstrong, P. D. Quay (2014) Rates and efficiency of the North Pacific biological pump. Graduate Climate Conference, Pack Forest, WA, October 31 – November 2 2014. Poster.

Palevsky, H. I., D.E. Lockwood, E. J. Armstrong, P. D. Quay (2014) Gross primary production and net community production rates across the North Pacific from triple oxygen isotopes and oxygen/argon dissolved gas ratios. TOS/ASLO/AGU Ocean Sciences Meeting, Honolulu, HI, 23-28 February 2014. Oral presentation.

Palevsky, H.I., Armstrong, E.J., and Quay, P.D. (2012) Quantifying the biological pump: comparing in-situ and satellite-based observations. Graduate Climate Conference, Pack Forest, WA, 26-28 October 2012. Poster.

Palevsky, H.I., Ribalet, F., Cosca, C.E., Swalwell, J.E., Cokelet, E.D., Quay, P.D., Feely, R.A., and Armbrust, E.V. (2012) Explaining a narrow region of high CO_2 uptake in the Gulf of Alaska: The role of biological production and phytoplankton community structure. TOS/ASLO/AGU Ocean Sciences Meeting, Salt Lake City, UT, 20-24 February 2012. Abstract #10039. Poster.

Palevsky, H.I., Ribalet, F., Cosca, C.E., Swalwell, J.E., Cokelet, E.D., Quay, P.D., Feely, R.A., and Armbrust, E.V. (2011) Using biological productivity and phytoplankton community structure to understand oceanic CO_2 uptake: A case study from the Gulf of Alaska. Graduate Climate Conference, Woods Hole, MA, 28-30 October, 2011. Oral presentation.

Palevsky, H., Ribalet, F., Cosca, C.E., Quay, P., Armbrust, E.V., and Feely, R.A. (2010) Biological productivity, phytoplankton community structure and air-sea CO_2 flux in the surface waters of the Gulf of Alaska. American Geophysical Union Fall Meeting, San Francisco, CA, 13-17 December 2010. Abstract #OS51A-1271. Poster.

Palevsky, H.I., A.M. Martini, and Ku, T.C.W. (2007) The pore water chemistry, microbial processes, and trace metal mobility of bioluminescent bays. Geological Society of America Northeastern Meeting, Durham, NH, 12-14 March 2007. Abstract #117605. Poster.

WORKSHOP PARTICIPATION:

On the Cutting Edge: Preparing for an Academic Career in the Geosciences
June 2015, Madison, WI

COMPASS Science Communication Training Workshop
Oct. 2013, Seattle, WA

Surface Ocean-Lower Atmosphere Study (SOLAS) Summer School
Aug. – Sept. 2013, Xiamen, China

UW Program on Climate Change Summer Institutes, Friday Harbor Labs, WA
Interactions between Terrestrial Ecosystems, Land Surface Processes and Climate, 2015
Climate Variability and Uncertainty, 2014
Response of Marine Ecosystems to Climate Forcing: Causes and Consequences, 2013
The Water Cycle in a Changing Climate, 2011
Climate Feedbacks, 2010

PROFESSIONAL SERVICE:

Gordon Research Seminar in Chemical Oceanography
Elected Co-Chair for 2017

Univ. of Washington School of Oceanography Undergraduate Academic Affairs Committee
Graduate Student Representative, Sept. 2015 – June 2016

Univ. of Washington Program on Climate Change Graduate Student Seminar
Co-Organizer, Mar. 2014 – June 2016

Graduate Climate Conference (GCC)
Carbon Cycle Session Chair, GCC8 (2014)
Fundraising Co-Chair, Organizing Committee, Abstract Committee, GCC6 (2012)

Univ. of Washington College of the Environment Curriculum Committee
Graduate Student Representative, June 2013 – June 2015

Univ. of Washington Program on Climate Change
Graduate Student Representative to the Executive Board, Sept. 2013 – Aug. 2014

Univ. of Washington School of Oceanography
Graduate Student Representative to the Faculty, Oct. 2011 – July 2012

OUTREACH:

Letters to a Pre-Scientist Pen Pal, Sept. 2012 – June 2016

Guest speaker on climate and ocean change, Seattle area schools, Jan. 2013. – Feb. 2016

Amherst Pathways Mentor to an undergraduate Chemistry major, Jan. – June 2015

Central Sound Regional Science and Engineering Fair Mentor, Jan. – Mar. 2015

Ocean Inquiry Project, Volunteer Instructor, May 2011 – Aug. 2014

5th Grade Science Fair Mentor, John Stanford International School, Jan. – April 2014

C2S2 Climate Change Student Summit, Science Mentor, April 2012

Educurious Expert Mentor, Ecological Impacts of Climate Change (9th grade), Oct. – Dec. 2011

FIELD WORK:

Kuroshio Extension student cruise in the Northwest Pacific Ocean (PIs S. Emerson and S. Riser)
R/V Melville, February-March 2013, 4 weeks

Vessel of opportunity cruises from Hong Kong to Long Beach, CA, USA
M/V OOCL Tokyo, May 2011 and January-February 2012, each 2 weeks
M/V OOCL Tianjin, July-August 2012, 2 weeks

PRISM Puget Sound time series cruise
R/V Thomas G. Thompson, November 2010, 2 days

International Bottom Trawl Survey (IBTS) of the North Sea, Scottish Fisheries Research Services
FRV Scotia, February 2008, 1 week

Northern Shrimp Survey, Marine Research Institute of Iceland
R/V Bjarni Sæmundsson, July 2007, 2 weeks

The Hydrodynamics and Biogeochemistry of Bioluminescent Bays, Keck Geology Consortium
Vieques, Puerto Rico, June 2006, 2 weeks

Williams-Mystic Maritime Studies Program Offshore Field Seminar, Gulf of Maine
SSV Corwith Cramer, August – September 2005, 10 days

PROFESSIONAL AFFILIATIONS:

The Oceanography Society (2015 – present)

National Association of Geoscience Teachers (2015 – present)

Earth Science Women's Network (2014 – present)

American Geophysical Union (2010 – present)

Sigma Xi (2007 – present)